Institute for Space Studies

THE JULY CLIMATOLOGY AND SEASONAL CHANGES

SIMULATED BY THE GISS GENERAL CIRCULATION MODEL

P.H. Stone

S. Chow

W.J. Quirk

GODDARD SPACE FLIGHT CENTER

NATIONAL AERONAUTICS AND SPACE ADMINISTRATION

The July Climatology and Seasonal Changes

Simulated by the GISS General Circulation Model

P. H. Stone,* S. Chow[†] and W. J. Quirk

Institute for Space Studies
Goddard Space Flight Center,
NASA, New York, N. Y. 10025

*Current affiliation: Department of Meteorology,
                       Massachusetts Institute of Technology

[†]GTE Information Systems

ABSTRACT

The GISS global general circulation model has been used to simu-
late July conditions, in a manner analogous to the previously described
January simulation. Sea surface temperatures, ice cover, snow line
and soil moisture were assigned values based on climatological data
for July, and the integration was started from real data for 18 June
1973. Because of the realistic initial condition, the model rapidly ap-
proached a quasi-steady state. Mean statistics were computed for the
simulated calendar month of July, and compared with climatological
data, mainly for the Northern Hemisphere troposphere. Qualitatively,
the model-generated energy cycle, distributions of winds, temperature,
humidity and pressure, dynamical transports, diabatic heating, evapo-
ration, precipitation and cloud cover are all realistic. Quantita-
tively, the July simulation, like the January simulation, tends to
underestimate the strength of the mean meridional circulations, the
eddy activity, and some of the associated transports. The July simu-
lation of zonal mean temperature and zonal wind fields is superior to
the January simulation in the Northern Hemisphere because of the ab-
sence of the polar night jet, and the decreased importance of large-
scale dynamical heating and cooling in summer.

In order to assess the model's ability to simulate seasonal
change, the July and January simulations were compared with each other
and with climatological data on seasonal changes. The model simulates
accurately the northward displacement of the mid-latitude jets, the
low-latitude Hadley cells, the tropical rain belt, the trade winds,
and the ITCZ from January to July, the seasonal reversal of the In-
dian monsoon, and the weakening of the zonal and meridional circu-

lations and the decline of eddy activity in the summer. The simulated seasonal changes in the Southern Hemisphere are much less pronounced than in the Northern Hemisphere as expected.

From a climatological point of view, there are three particular aspects of the model's simulations that need to be improved: (1) Arctic regions in January are as much as 10°K too cold, because of the model's underestimate of the dynamical transports of heat into high altitudes; (2) the simulation of the climatological fields in the vicinity of the Himalayas and Southeast Asia is noticeably poorer than in other areas -- for example, the rainfall rates in Southeast Asia are half the observed amount; and (3) the global albedo in July is too high when compared to satellite-derived values (0.35 vs. 0.26), at least partially because the model-simulated deep, penetrating cumulus clouds occur too frequently in July.

1. Introduction

The global general circulation model (GCM) of the Goddard Institute for Space Studies (GISS) was developed originally for use in observing system simulation experiments, asynoptic data assimilation studies, and experimental forecasting (Jastrow and Halem, 1973). Previous tests of the model's skill have been designed with these uses in mind (Somerville et al., 1974; Druyan, 1974; Tennenbaum, 1976; Druyan et al., 1976). These tests have shown that the model's skill at simulating tropospheric statistics and forecasting weather in the northern hemisphere in winter is comparable to that of other GCM's with similar resolution.

More recently, the GISS model has been used in climate sensitivity studies (Charney et al., 1974; Somerville et al., 1976). Validation of any GCM for use in such studies requires somewhat different tests of its skill than those referred to above. Ideally one would like to demonstrate that the model can simulate accurately an observed change in climate. The one change for which good observations are available is the seasonal change from winter to summer, which is in fact just a climate change on a short time scale. Since the seasonal changes are substantial, they represent a simple, stringent test for validating any climate model developed without reference to observed seasonal changes.

Tests of the ability of other GCM's to simulate the atmosphere have also concentrated on simulations of winter conditions (Holloway and Manabe, 1971; Kasahara et al., 1973; Newson, 1974; Gates, 1975).

Current GCM's generally prescribe boundary conditions such as sea-surface temperature, but this does not prevent one from testing their ability to simulate seasonal changes in atmospheric processes that accompany prescribed seasonal changes in boundary conditions. The skill of a GCM in simulating some aspects of seasonal change has been studied by Manabe et al. (1974) and Manabe and Holloway (1975). These studies were concerned with seasonal changes in the tropics and in the hydrological cycle, respectively. However, no study of the skill of a GCM in simulating, for example, seasonal changes in the hemispheric heat balance or energetics, or in the polar heat balance, has been published. Polar conditions are particularly crucial in climate problems (SMIC Report, 1971), and many simplified climate models have been based solely on the heat balance (Sellers, 1969; Budyko, 1969; Gal-Chen and Schneider, 1975).

Consequently, in this paper we present a study of the skill of the GISS GCM in simulating seasonal changes. In section 2 we give a brief description of the model. More details can be found in the paper by Somerville et al. (1974). In section 3 we describe the results of an experiment simulating the July climatology which parallels the January simulation presented by Somerville et al. (1974). In section 4 we directly compare the January and July simulations with each other and with observations. Finally, we summarize our results in section 5.

2. Model description

The GISS model is a global, primitive equation model, with longitude and latitude as horizontal coordinates, and a vertical "sigma" coordinate defined by

$$\sigma = \frac{P - P_t}{P_s - P_t} \ .$$

P is the pressure, P_s the surface pressure, and P_t the pressure at the top of the model atmosphere, taken to be 10 mb. Integrations are performed with nine equally-spaced levels in the vertical, a horizontal grid of four degrees of latitude by five degrees of longitude, and a time step of five minutes. The numerical method of integration is that given by Arakawa (1972) for a distribution of variables over the horizontal grid corresponding to his Scheme B. The space-differencing is quasi-conservative for enstrophy and kinetic energy, and the time-differencing is a combination of the regular Matsuno and the time-alternating space-uncentered Matsuno procedures.

The model contains no explicit sub-grid scale horizontal diffusion. Sub-grid scale vertical diffusion is included by means of diffusion laws with simple parameterizations for the kinematic eddy viscosity, thermal diffusivity, and water-vapor diffusivity based on Deardorff's (1967) work and on experiments with the GISS model (Stone et al., 1974). The only difference between the model used in the calculations and comparisons reported here, and that used in the calculations reported earlier by Somerville et al. (1974), is in the calculation of the eddy diffusion coefficients in the lowest model layer. In particular, these coefficients depend on the static stability of the

lowest model layer (see Eq. 12 of Somerville et al., 1974), and the method of calculating this static stability has been changed. The difference formula for this quantity in the earlier calculations used the ground temperature, while in the present calculations the ground temperature was replaced by the atmospheric surface temperature. The January simulation described by Somerville et al. (1974) was repeated with this modified formula, in order to get a clean comparison with the July simulation described in section 3 below.

The diabatic heating includes contributions from radiation, condensation and convection as well as from diffusion. The absorption of solar radiation is parameterized with formulae based on detailed multiple scattering calculations (Lacis and Hansen, 1974). The amount of absorption depends on the model generated clouds and humidity, and varies with the solar zenith angle and the solar flux. The solar zenith angle and flux are calculated from the earth's orbital elements, and change diurnally and seasonally. Long-wave radiative heating rates are calculated from simplified non-gray calculations using twice the number of model layers, and are dependent on the model-generated clouds and temperature and humidity fields.

Condensation in the model is generated by two different mechanisms, large-scale supersaturation and small-scale moist convection. Supersaturation occurs whenever the relative humidity exceeds 100%, and moist convection whenever the moist static energy at lower atmospheric levels exceeds the saturated moist static energy at higher levels. The diabatic heating due to large scale supersaturation is calculated by assuming that condensation reduces the relative

humidity of the supersturated levels to 100%, and that the condensed water either re-evaporates in the next lower layers, or precipitates to the ground if all lower layers are saturated. The heating due to moist convection is parameterized by Arakawa's scheme for moist convection in a 3-layer model (Arakawa et al., 1969), generalized to a 9-layer model. In this scheme the atmosphere is heated by the subsidence generated by the upward mass flux in the convective clouds, and humidity in excess of saturation in any layer condenses and precipitates, directly to the ground in the case of deep or middle level convection, or to the next lowest unsaturated layer in the case of low level convection. Dry convection is also included by means of a conventional adiabatic adjustment scheme.

Clouds are generated whenever large scale supersaturation or small scale moist convection occurs. Table 2.1 lists the eight cloud types and sub-types which may be generated, depending on the initiating process and the atmospheric layers affected. For each cloud type the table lists the layers in which they occur (the model's layers are numbered from one to nine from top to bottom); the most closely analogous atmospheric cloud type; the cloud's short wave optical thickness; and its visual albedo. The optical thickness, τ, is based on observations of the analogous cloud types, and the albedos, a, are calculated from an approximate formula derived from scattering theory by Lacis and Hansen (1974),

$$a = \frac{0.13\tau}{1 + 0.13\tau} \ .$$

For purposes of calculating long-wave heating rates, all clouds are treated as black bodies. Supersaturation clouds in level 9 and deep and middle level convective clouds are accompanied by precipitation.

Ground temperatures are predicted from the net heating and cooling at the surface by radiation, sensible heat, and latent heat fluxes. Sea-surface temperatures are prescribed, and Fig. 2.1 shows the values used in the July simulation. These sea-surface temperatures were taken from Schutz and Gates' (1972) July analysis, which is based on data from Washington and Thiel (1970) and from the Hydrographic Office Atlases (1944, 1957, 1958). The surface fluxes of sensible and latent heat and the surface stress are parameterized by drag laws. The surface albedo is taken to be 0.07 over water, 0.14 over land, and 0.7 over ice and snow. The distribution of ice used in the July simulation is shown in Fig. 2.2. This distribution was also taken from Schutz and Gates (1972). The snow line over land varies daily according to Eq. (11) given by Somerville et al. (1974). The ground wetness, GW, (percent of saturation) used in the calculation of latent heat fluxes at the surface is fixed, and is calculated for each grid point over land from observed mean surface relative humidities, SRH, by using the formula

$$GW = \frac{SRH - 15}{85} \quad .$$

The surface relative humidities used in this calculation were those given by Gates (1972), which were based on data from Crutcher and Meserve (1970) and Taljaard et al. (1969). The resulting values of Ground Wetness for July are illustrated in Fig. 2.3. Grid points with ice, snow or ocean are assumed to have a ground wetness of 100%. The ground has a realistic topography, illustrated in Fig. 4 of Somerville et al. (1974). The boundary conditions used in the January simulations are given by Somerville et al. (1974).

3. July simulation

The July simulation was carried out in a way exactly analogous to the January simulation. The integration was started from an initial state taken from real data, in this case data for 18 June 1973, supplied by the National Meteorological Center (NMC) in Washington, D. C. (The January integration started from real data for 20 December, 1972). The data were taken from NMC's experimental global data set (Flattery, 1971). This data did not include humidities for the model's upper three layers, so climatological values were used for these humidities. The sea-surface temperature, ice cover, and soil moisture throughout the integration were fixed at the July mean climatological values given in section 2. Solar declination, solar insolation and snow line varied with calendar data as described in section 2.

a) Time evolution

The integration was carried out for 44 days of simulated time, through July 31. Figs. 3.1 and 3.2 show the computed time evolution in the Northern and Southern Hemispheres, respectively, of the integrated tropospheric (layers 2-9) zonal kinetic energy (K_M), eddy kinetic energy (K_E), zonal available potential energy (P_M) and eddy available potential energy (P_E). Because of the realistic initial state, a quasi-equilibrium state was achieved within a few days. The longer-term changes in the hemispheric energies during the integration are seasonal changes, and are realistic. For example, Peixoto and Oort (1974) found that in the Northern Hemisphere the monthly mean value of P_M changed from 18.8×10^5 J m^{-2} in June to 13.0×10^5

$J\ m^{-2}$ in July; a similar change is apparent in Fig. 3.1.

In addition, smaller amplitude fluctuations occur, especially in eddy energies in the Southern Hemisphere. These fluctuations have the same properties as the vacillations found in the Southern Hemisphere EOLE balloon data by Webster and Keller (1975). For example, the fluctuations have about a 20-day period, and the changes in the eddy and zonal kinetic energies are negatively correlated, in accord with Webster and Keller's findings. This vacillation is also apparent in the January simulation of the Southern Hemisphere (Somerville et al., 1974, Fig. 10). There is just a hint of a similar vacillation in the Northern Hemisphere energies, but if it is real, it is much less pronounced than in the simulated Southern Hemisphere. An experiment in which the sub-grid scale eddy viscosity was completely suppressed shows this same sort of vacillation more prominently in the Northern Hemisphere (Stone et al., 1974). This suggests that the greater prominence of the vacillation in the Southern Hemisphere is due to a smaller effective viscosity in the Southern Hemisphere, perhaps because of the lesser prominence of mountains in the Southern Hemisphere. The simulated energy cycle is discussed in section 4a below.

b) Zonal mean state

Figs. 3.3 - 3.5 show the simulated zonal mean wind fields, along with the observed zonal mean wind fields in the Northern Hemisphere based on data from Oort and Rasmusson (1971). The simulated mean zonal motions (Fig. 3.3.) are in excellent agreement with the observations. In fact the July simulation of zonal winds is superior to

the January simulation in the Northern Hemisphere, mainly because the model's resolution in the stratosphere is inadequate for resolving the Northern Hemisphere's polar night jet (Somerville et al., 1974). The mean meridional and vertical motions (Figs. 3.4 and 3.5, respectively), are simulated well qualitatively -- i.e., the strong Southern Hemisphere Hadley cell and the weak Northern Hemisphere Hadley and Ferrel cells are all reproduced in the simulations in about the right locations. However, the meridional circulations in the simulation are understimated compared to the observations. This underestimate is most apparent in the magnitudes of the vertical velocities (Fig. 3.5) and of the meridional stream function (see Fig. 4.6 below). Similar underestimates occurred in the January simulation (Somerville et al., 1974). The underestimate of the strength of the Hadley cells may be due to the omission from the model of any vertical mixing of momentum by moist convection (Stone et al., 1974; Schneider and Lindzen, 1976). The strength of the Ferrel cells is closely related to the strength of the eddy fluxes (Kuo, 1956). Consequently the weakness of the simulated Ferrel cells may be attributed to the underestimate of the eddy flux of momentum in the simulations (see Fig. 3.9 below).

Figs. 3.6, 3.7, and 3.8 show the zonal mean temperature, potential temperature, and specific humidity fields, respectively, from the July simulation, together with the observed fields, based on Oort and Rasmusson's (1971) data. The simulated temperature and potential temperature fields are generally in good agreement with the observations in the troposphere. For example, the tropospheric

static stabilities are within 1/2°K/km of the observed static stabilities. The most notable discrepancies in the temperature are in the stratosphere where the model's vertical resolution is poor. Here the simulated equatorial temperatures are about 10°K too warm. The simulated specific humidity field is on the whole realistic. Near the surface in tropical regions, the simulated humidity falls off more rapidly with height than in the observations, because the simulated equatorward branch of the Hadley cell and its associated moisture transport are too strongly peaked near the ground (see Figs. 3.4 above and 3.14 below).

c) Meridional transports

Figs. 3.9 - 3.14 show the simulated and observed zonal mean fields of the meridional transports of westerly momentum, sensible heat, and water vapor by eddies and by the mean meridional circulations. The observed fields are based on Oort and Rasmusson's data (1971). In calculating the transports we have followed Oort and Rasmusson's (1971) definitions of the transports. Qualitatively, the simulated meridional transports are realistic. For example, the transports in low latitudes are dominated by the Southern Hemisphere Hadley cell (Figs. 3.10, 3.12, and 3.14) while the transports in mid and high latitudes are dominated by the eddies (Figs. 3.9, 3.11 and 3.13); the eddy momentum transport tends to concentrate the mid-latitude jets (Fig. 3.9); the poleward transport of sensible heat by the eddies shows the characteristic double maximum in mid-latitudes, one near the surface and one near the tropopause (Fig. 3.11); and the poleward transport of water vapor by the eddies is concentrated near the

surface in mid-latitudes (Fig. 3.13). The simulated locations of the maxima in the different components of the meridional transports are also in very good agreement with the observed locations.

However, the strength of the transports is generally underestimated in the July simulation, just as they were in the January simulation (Somerville et al., 1974). The previously described underestimate of the strength of the Hadley and Ferrel cells causes the transports of momentum and sensible heat by the mean meridional circulations to be about one-half as large as the observed transports in the poleward branch of the Southern Hemisphere Hadley cell, and much smaller than the observed transports in mid-latitudes (Figs. 3.10 and 3.12). The maximum in the eddy transport of momentum near the tropopause in mid-latitude is about one-third as strong in the simulation as in the observations (Fig. 3.9). This deficiency is to be expected in view of the model's underestimate of the strength of eddies in general (see section 4a below). Such underestimates appear to be common in general circulation models (Manabe et al., 1970; Kasahara et al., 1973; Somerville et al., 1974). On the other hand, the simulated maximum in the eddy transport of sensible heat is much more realistic (Fig. 3.11). The maximum water vapor transport by the equatorward branch of the Southern Hemisphere Hadley cell is overestimated in the simulation (Fig. 3.14), but this transport is also too sharply peaked near the ground, so the total transport in the simulation is close to the observed transport.

d) Eddy activity

Fig. 3.15 shows the zonal mean distribution of the computed and observed variances of the temperature field in July. This variance is one convenient measure of eddy activity. The computed variances are in good agreement with the observed variances. Both lack the sharp maximum found in January in mid-latitudes near the surface (Somerville et al., 1974).

Fig. 3.16 shows the eddy kinetic energy spectrum for the Northern Hemisphere troposphere (levels 2-9) in the July simulation. Saltzman's (1970) conventions were used in calculating the spectrum. The eddy kinetic energy peaks at low wave-numbers, but does not fall off sharply with wave-number until wave-numbers beyond 9 are reached. In January the sharp fall-off in the simulated spectrum occurred after wave-number 5 (Somerville et al., 1974). In the wave-number range 8-15 the computed spectrum had an approximate -2.4 power dependence on wave-number in July, and an approximate -2.5 power dependence in January. These results may be contrasted with the -3 power dependence of geostrophic or two-dimensional turbulence. At all wave-numbers, the kinetic energy in July is less than in January, with the difference being largest at wave-numbers 2-5.

e) Diabatic heating

Figs. 3.17 and 3.18 show the zonal mean radiative heating rates due to solar and terrestrial radiation, respectively, calculated from the July simulation. The distributions are in good qualitative agreement with independent calculations (e.g., Dopplick, 1972). Quantitative checks of the simulated atmospheric heating rates are not yet

possible, since they are very sensitive to the vertical distribution of cloud cover used in the calculations (Haurwitz and Kuhn, 1974), and the actual vertical distribution is not well known. The seasonal changes in the simulated radiative heating rates agree with one's expectations: reflecting the January heating rates about the equator would give a good approximation to the July heating rates.

Figs. 3.19 and 3.20 show the zonal mean heating rates in the July simulation due to parameterized sub-grid scale moist convection and large scale supersaturation, respectively. The former process dominates in the tropics, and the latter in mid and high latitudes. Again the July heating rates represent approximately a reflection of the January heating rates about the equator. Other diabatic processes in the model, i.e., sub-grid scale diffusion and dry convection, have negligible atmospheric heating rates compared to those illustrated in Figs. 3.17 - 3.20.

4. Seasonal Changes

In this section we present results from the July simulation described in the preceding section, together with results from the January simulations and from observations, in order to ascertain the model's ability to simulate seasonal changes. The January and July simulations described here differ only in the choice of initial conditions and boundary conditions. The January simulation results differ slightly from those presented by Somerville et al. (1974) because they use the modified formula for the eddy diffusion coefficients in the lowest layer referred to in section 2, and because all of the present calcu-

lations are based on a sampling interval of four hours instead of twelve hours. In addition, the latitude-height distributions of eddy transports of momentum, sensible heat and water vapor published in Somerville et al. (1974) were inaccurate, because of a programming error in the diagnostic code. The difference between the published transports and the corrected transports is 10% to 20%.

a)   Energy cycle

One convenient measure of the overall performance of a general circulation model is the accuracy with which it simulates the atmosphere's energy cycle. The simulated energy cycles in the Northern Hemisphere troposphere (levels 2 to 9) for January and July are shown in Fig. 4.1. The corresponding observed energy cycles estimated by Oort and Peixoto (1974) are shown in Fig. 4.2. The new symbols in the figures are defined as follows:

$$G(X) \quad \text{-- generation of X}$$
$$D(X) \quad \text{-- conversion of X}$$
$$C(X,Y) \quad \text{-- conversion of X to Y}$$

The model's energetics were computed for the mixed space-time domain using the same formulae as Oort and Peixoto (1974) with the exception of $C(P_M, K_M)$. Oort and Peixoto calculated this conversion

from

$$C(P_M, K_M) = -\int [\bar{v}]g \frac{\partial[\bar{z}]}{a\partial\phi} \, dm \, ,$$

whereas the model-generated value was calculated from the more common definition (Oort, 1964; Saltzmann, 1970)

$$C(P_M, K_M) = -\int [\bar{\omega}]'' [\bar{\alpha}]'' \, dm.$$

(Oort and Peixoto's (1974) notation is used in these expressions.) For the global domain these two formulations are identical, but for the hemispheric domain they differ considerably because the flux of potential energy across the equator is significant (see Fig. 4.13 below). The previously published calculations for the simulated energy cycle in January (Somerville et al., 1974) used Oort's (1964) approximate formulae, which neglect variations of the static stability. Oort and Peixoto's (1974) formulae do not neglect these variations and give substantially different results for P_M and P_E. Consequently, the energy box diagrams presented here use the exact formulae, and the diagram for January in Fig. 4.1 differs from that presented by Somerville et al. (1974).

The simulated Northern Hemisphere energy cycle and its seasonal change agree quite well with the observations. The most notable discrepancy in the simulations is the understimate of K_E. This is a common feature of general circulation models, apparently caused by inadequate horizontal resolution (Manabe et al., 1970; Wellck et al., 1971). However, even for K_E the simulated seasonal change is accurate -- i.e., the July value is 55% of the January value in both the simulations and the observations. The January values of P_M and K_M in

the simulations are about 20% higher than in the observations, because the meridional temperature gradient in the simulated January is too large (see Fig. 4.11 below). Because of this larger gradient, the meridional deviation from the area mean temperature on isobaric surfaces is increased, thus increasing P_M, and the mean zonal thermal wind is increased, thus increasing K_M. It is not clear whether the discrepancy between the simulated and observed values of $G(P_M)$ are significant. The "observed" values were in fact calculated as residuals, and different methods of estimating $G(P_M)$ give substantially different values (Oort and Peixoto, 1974).

The simulated energy cycle for the Southern Hemisphere troposphere (levels 2 - 9) is shown in Fig. 4.3 for January and July. The energy cycle is qualitatively similar to that for the Northern Hemisphere. However, the seasonal changes in the Southern Hemisphere are significantly less than in the Northern Hemisphere, because of the moderating influence of the greater ocean area in the Southern Hemisphere.

b) Momentum balance

Fig. 4.4 shows the latitudinal distribution of vertically averaged mean zonal wind for the model atmosphere for January and July, together with the observed values based on data from Oort and Rasmusson (1971). In all the subsequent figures in this section with the same format as Fig. 4.4, the solid curves refer to the simulated January atmosphere, the dashed curves to the simulated July atmosphere, the triangles to the observed January atmosphere, and the circles to the observed July atmosphere. The vertical averages are

all computed for the troposphere -- i.e., for the model the data are averaged over layers 2 to 9, corresponding approximately to pressures from 120 mb to the surface, and for the observations (Oort and Rasmusson, 1971) the data are averaged over pressures from 125 mb to 1012.5 mb.

Fig. 4.4 shows that the seasonal variation in the Northern Hemisphere jet is simulated accurately by the model. In particular, the jet is displaced 10° northward in July, and is only half as strong as in January. As reported previously (Somerville, 1974), the model-calculated Northern Hemisphere jet in January is too broad, because the model-calculated meridional temperature gradient in northern high latitudes is too large (see Fig. 4.11 below). The width of the Northern Hemisphere jet in July is simulated much more accurately. The seasonal changes in the jet in the Southern Hemisphere are much less pronounced than in the Northern Hemisphere.

Figs. 4.5 and 4.6 show the meridional stream function from the simulations and the observations for January and July, respectively. The model's underestimate of the strength of the meridional circulations is again apparent, but the underestimate in January and July is consistent so that the seasonal changes are simulated accurately. In both the simulations and the observations, the Northern Hemisphere Hadley cell all but disappears in July, and the Northern Hemisphere Ferrel cell is only about one-third as strong in July as in January. The seasonal behavior in the Southern Hemisphere in the simulations contrasts strongly with the behavior in the Northern Hemisphere. In particular, the strength of the Ferrel cell in the Southern Hemisphere

shows virtually no change from January to July. The model's under-
estimate of the circulation in the Hadley cells is less in the South-
ern Hemisphere than in the Northern Hemisphere.

Fig. 4.7 shows the latitudinal distribution of the northward
transport in the troposphere of relative angular momentum by the
large scale eddies (transient plus stationary) and by the mean meri-
dional circulations for both January and July, as simulated by the
model, together with the observed transports based on data from Oort
and Rasmusson (1971). The results are what one would expect from the
already quoted results for eddy kinetic energy and the mean meridional
stream function. The eddy transports and mean transports are under-
estimated in the simulations, but their seasonal changes are simulated
reasonably well. In the summer the mean transports virtually disap-
pear and the eddy transports are reduced, by a substantial amount in
the Northern Hemisphere and by a lesser amount in the Southern Hemi-
sphere.

c) Hydrological cycle

Fig. 4.8 shows the tropospheric mean specific humidity as a func-
tion of latitude for January and July, both from the simulations and
from the observations (Oort and Rasmusson, 1971). The model's under-
estimate of the strength of the winter Hadley cell leads to an under-
estimate of the moisture transport by the equatorward branch of the
Northern Hemisphere Hadley cell in January (see Fig. 4.14 below), and
this results in an underestimate of the humidity near the equator in
the January simulation, as is apparent in Fig. 4.8. However, Fig.
4.8 shows that on the whole the simulated seasonal changes in the

humidity agree quite well with the observations. This good agreement is not surprising when one considers that the specific humidity is strongly controlled by the temperature through the Clausius-Clapeyron relation, and that the sea-surface temperatures in the simulations are prescribed to have the observed January and July values. The simulated seasonal changes in the humidity in the Southern Hemisphere are again much smaller than in the Northern Hemisphere because of the greater moderating effect of the southern oceans.

Figs. 4.9 and 4.10 show the zonal mean precipitation and evaporation rates, respectively, for January and July, from the simulations and the observations. The observed values in both figures are taken from Möller (1951) and Budyko (1963), respectively, as analysed by Schutz and Gates (1971, 1972a,b). The observed precipitation rates are actually seasonal rates, i.e., means for December-January-February and June-July-August, rather than for January and July. The simulated seasonal changes in the precipitation rates are in good agreement with the observations. In particular, the changes are small, except in the subtropics, where the rainfall is substantially increased in summer.

The simulated evaporation rates shown in Fig. 4.10 are systematically lower than the observed (actually inferred) rates in low latitudes. Most of the evaporation comes from the ocean surface, which is prescribed to have the correct climatological temperature for each month. However, the simulated atmospheric specific humidities near the surface are high (see Fig. 3.8) and this probably accounts for the underestimate of the evaporation rates. Similar underestimates of the evaporation from the oceans have appeared in other simulations with similar resolution (Holloway and Manabe, 1971).

d)   Heat Balance

Fig. 4.11 shows the mean tropospheric temperature for January and July as a function of latitude, from both the simulations and the observations (Oort and Rasmusson, 1971). In low and mid latitudes, the seasonal temperature change has been simulated accurately. However there is a notable discrepancy in th north polar regions. These regions are as much as 10°K too cold in the January simulation, although they are simulated much more accurately in July. It is the resulting overestimate of the meridional temperature gradient in the simulated January which causes the broadness of the jet and the overestimate of K_M and P_M in the Northern Hemisphere in January. In addition, the simulated Northern Hemisphere temperatures in July are systematically 1°K or 2°K too cold.

Other GCM's with similar horizontal resolution show comparable discrepancies in north polar regions in January (Holloway and Manabe, 1971; Kasahara et al., 1973; Newson, 1974). In these latitudes the amount of solar heating is negligible in January, and there are very few ocean grid points (which act as heat reservoirs in the model). Consequently, the temperatures are determined essentially by a balance between the import of heat by atmospheric motions from low latitudes and the export of heat by long-wave radiation to space. The lower temperatures in the simulations thus imply that the dynamical heating and long-wave cooling are both reduced compared to the atmospheric situation. In fact the model-simulated long-wave radiation to space in the arctic regions in January is about 20% smaller than the amount measured from satellites (Vander Haar and Suomi, 1971).

This reduction is what one would expect for lower temperatures.

On the other hand, the lower temperatures imply larger meridional temperature gradients, as illustrated in Fig. 4.11. One would expect these increased gradients to be accompanied by an increased dynamical flux into arctic regions in January. Actually, the dynamical flux in the January simulation is reduced, as shown in Fig. 4.12. This figure shows the meridional tropospheric flux across a latitude circle of total energy (potential energy plus latent heat plus sensible heat plus kinetic energy) by all atmospheric motions as a function of latitude, calculated both from the simulations and from the observations (Oort and Rasmusson, 1971). At 58°N in January, the simulated transport is about 30% less than the observed transport, and this reduction implies a decrease in the mean dynamical heating rate in higher latitudes of about 1/3°K per day. This reduction in the dynamical flux is the apparent cause of the low arctic temperatures in January. Discrepancies in the total meridional flux at lower latitudes have a much smaller impact on mean temperatures because they are spread over much larger areas. Similar deficiencies in the dynamical heating rate in north polar regions are apparent in January simulations by other GCM's with comparable resolution (Holloway and Manabe, 1971; Kasahara et al., 1973). By contrast, Fig. 4.12 shows that the simulation of the meridional energy flux in July is much more realistic.

Figs. 4.13, 4.14 and 4.15 show the individual components of the meridional energy flux which make significant contributions to the total flux, i.e., the flux of potential energy by the mean meridional

circulations (Fig. 4.13), and the fluxes of latent heat (Fig. 4.14) and sensible heat (Fig. 4.15) by the large scale eddies and by the mean meridional circulation. Once again these figures show the mean tropospheric fluxes vs. latitude for both January and July, calculated from both the simulations and the observations (Oort and Rasmusson, 1971). The seasonal changes in these fluxes are in good qualitative agreement with the observations. For example, the seasonal reversal in sign of the cross-equatorward transports by the mean meridional circulation and the sharp decrease in the transports by the Hadley cells in summer (Figs. 4.13, 4.14b, 4.15b), and the sharp decrease in the eddy transport of sensible heat in the Northern Hemisphere in summer (Fig. 4.15a) are reproduced by the simulations. However, the deficiencies noted previously -- namely the underestimates of the strength of the Hadley cells and of the activity of the large scale eddies -- again cause most of the individual components of the meridional flux to be underestimated. The seasonal changes in the Southern Hemisphere are again much less than in the Northern Hemisphere. The seasonal changes in the eddy latent heat flux (Fig. 4.14a) are much less than the seasonal changes in the eddy sensible heat flux (Fig. 4.15a), because seasonal changes in eddy activity tend to be compensated by seasonal changes in specific humidity (cf. Figs. 4.1 and 4.8).

Figs. 4.13, 4.14 and 4.15 show that the deficiency in the dynamical heating of north polar regions in January is primarily due to the underestimate of the eddy flux of sensible heat. This flux can be separated into the contributions by standing eddies and by transient eddies, and it then becomes apparent that the main deficiency

is in the standing eddy flux of sensible heat in mid-latitudes. Fig. 4.16 shows this flux calculated for the troposphere as a function of latitude from the simulations and also from observations (Oort and Rasmusson, 1971). Since the stationary eddies virtually disappear in summer, errors in simulating the associated flux only affect the simulation of north polar temperatures in January. One possible source of error in the simulated standing eddy flux is the smoothed field of topography prescribed in the model (Somerville et al., 1974).

The discrepancy in the July temperatures in the Northern Hemisphere is systematic (see Figure 4.11) and cannot be explained by deficiencies in the dynamical heating rates, which in July are not systemmatically high or low (see Figure. 4.12). Rather the discrepancy must be attributed to deficiencies in the simulation of the radiative heating. In particular, the lower temperatures in the July simulation imply that the simulated absorption of short-wave radiation and emission of long-wave radiation are too low.

The deficit in the short-wave absorption is revealed in the calculated value of the global albedo. In the July simulation this is 0.346, whereas the mean value measured by satellites for the months of June, July and August is 0.26 (Vonder Haar and Suomi, 1971). This discrepancy is more than ample to account for the 1°K to 2°K discrepancies shown in Fig. 4.11. The discrepancy would be even greater if it were not for the stabilizing effect of prescribing sea surface temperatures. No comparable discrepancy in the albedo appeared in the January simulation. The simulated mean global albedo for January

was 0.325, which may be compared to the observed value for the months
of December, January and February of 0.31 (Vonder Haar and Suomi,
1971). It is noteworthy that the simulated seasonal change in the
global mean albedo has the wrong sign.

The main contributor to the global mean albedo is cloud albedo.
Table 4.1 shows the percentage cloud cover for each hemisphere and
each season in the simulations, broken down by cloud type. In general
the convective clouds increase in summer, while the supersaturation
clouds decrease. Thus, changes in the two cloud types tend to com-
pensate each other. The total cloud cover shows opposite tendencies
in the different hemispheres, increasing in summer in the Northern
Hemisphere, but increasing in winter in the Southern Hemisphere. The
simulated total cloud cover in the Northern Hemisphere is in excel-
lent agreement with the observed values of 0.48 in January and 0.52
in July (Sasamori et al., 1972). Also the distribution of convec-
tive cloud types is realistic, in particular the dominance of low
level and deep penetrating convection (Ogura and Cho, 1973). How-
ever, the seasonal tendency in the total cloud cover in the Southern
Hemisphere is opposite to that reported by Sasamori et al. (1972).

Figs. 4.17 and 4.18 show the latitudinal variations of mean
cloud cover due to convective clouds and supersaturation clouds, re-
spectively. In these figures the cloud covers generated by the simu-
lations are compared with observed values based on the analysis by
Rodgers (1967) for the Northern Hemisphere and by Sasamori et al.
(1972) for the Southern Hemisphere. In calculating the observed
cloud covers from their cloud covers for individual cloud types, we

assumed that cloud types occurring at different levels had a random overlap. These figures show that the simulated seasonal changes in the Northern Hemisphere are realistic as far as the super-saturation clouds are concerned, but are much too large as far as the convective clouds are concerned. This increase in the convective cloud cover in the Northern Hemisphere summer is mainly attributable to the increase in penetrating convective clouds (see Table 4.1). Since these clouds have albedos of 0.81 (see Table 2.1) the discrepancy in the deep convective clouds could account for much of the discrepancy in the albedo in the July simulation. The poor simulation of the deep, penetrating convective cloud cover can be attributed to inadequacies in the parameterization scheme for moist convection (Stone et al., 1975). It is interesting to note that this discrepancy was not accompanied by a similar discrepancy in the precipitation in the Northern Hemisphere summer (see Fig. 4.9).

In the Southern Hemisphere the convective cloud cover in the simulations shows strong local variations, but in a mean sense is in reasonable agreement with the observations. The simulated super-saturation cloud cover in the Southern Hemisphere is systematically larger than the cloud covers reported by Sasamori et al. (1972), but satellite observations (Clapp, 1964) also give substantially larger estimates of cloud cover in the Southern Hemisphere. The marked increase in the supersaturation cloud cover in the subtropics of the Southern Hemisphere in July accounts for the increase in the total cloud cover in the Southern Hemisphere in July (see Table 4.1) and for the apparent discrepancy with the observed seasonal change in the Southern Hemisphere (Sasamori et al., 1972).

e)   Climatology

Figs. 4.19 and 4.20 show the simulated sea-level pressures for January and July, respectively. The semi-permanent pressure systems and their seasonal changes are generally reproduced accurately. For example, the Icelandic low and Siberian high are present in January but not in July; the low in the Gulf of Alaska in January is replaced by a high in July; and the Himalayan low and Australian high are present in July but not in January. The primary defect in the simulations is the sea-level pressures over mountainous regions. For example, the low over the Andes in January and the high over the Antarctic in July are unrealistic, and the low pressures over the Himalayas in July are too extreme. The "sea level" pressures shown for mountainous regions are, of course, extrapolated pressures rather than true pressures. Similar discrepancies in sea level pressures over mountainous regions occur in other GCM's (Manabe and Holloway, 1975).

Figs. 4.21 and 4.22 show the simulated 500 mb geopotential height surfaces for January and July, respectively. Again the seasonal changes in the major features are realistic. For example, the mid-latitude gradients are much weaker in summer, and the ridge over the Eastern Atlantic is much weaker in July than in January.

Figs. 4.23 and 4.24 show maps of the model-generated surface winds for January and July, respectively. The surface winds shown here were calculated by linearly extrapolating the velocities in layers 8 and 9 to the earth's surface. The main features and their seasonal changes are simulated realistically. For example, the trade winds and the intertropical convergence zone (ITCZ), their northward shift in July, and the seasonal reversal of the monsoonal circulation over India are all readily apparent. In January, however, the low-level winds in the

Bay of Bengal and southeast Asia are much too weak and in the wrong direction (Riehl, 1954). This defect is probably caused by the fact that the simulated Siberian high in January is weaker and farther east than in reality (see Fig. 4.19). Also, there is a tendency for the simulated ITCZ in the Indian Ocean in January and in the central Pacific in both seasons to be too near the equator, and to be too far north over Africa in July (Riehl, 1954; Godshall, 1971). The displacement over Africa in July is caused by the ground albedo in the model always being taken to be 0.14. Other studies have shown that a more realistic albedo over the Sahara of 0.35 leads to a correct positioning of the ITCZ over Africa in July (Charney et al., 1975).

Figs. 4.25 and 4.26 show maps of the model-simulated precipitation rates in January and July, respectively. The tropical rainbelt and the subtropical dry belts and their seasonal changes have all been simulated realistically. For example, the rainfall maxima over South America and Africa have shifted northward from January to July by about 25° and 30° latitude, respectively, and the Indian monsoon develops in July. The rainbelt across Africa in July, like the ITCZ, is actually about 6° latitude too far north (Ramage, 1971). This is again the result of the unrealistic ground albedo in the Sahara (Charney et al., 1975). The ITCZ shows up particularly clearly in the rainfall pattern over the eastern Pacific in July. The most notable defect in the simulated precipitation rates is their magnitude in July over Southeast Asia where they are about one-half the observed rate (Ramage, 1971).

Maps of the simulated deep, penetrating convective cloud cover are shown in Figs. 4.27 and 4.28 for January and July, respectively. As discussed above, the greater penetrating convective cloud cover in July in the Northern Hemisphere is at least partially responsible for the abnormally high simulated global albedo in July. The deep, penetrating convection occurs most frequently over continents and near the equator. The associated clouds over water near the equator show a small northward shift from January to July. The ITCZ is particularly prominent in the cloud cover over the eastern Pacific and the Atlantic in July. The penetrating convection over land shows a strong increase in summer.

Maps of the simulated low-level convective cloud cover are shown in Figs. 4.29 and 4.30 for January and July, respectively. The low-level convection is concentrated in mid and high latitudes, and tends to increase over land in summer but decrease over water in summer. Consequently, low level convection is a maximum in the Northern Hemisphere (which is mostly land) in the summer, and is a maximum in the Southern Hemisphere (which is mostly water) in the winter (see Table 4.1).

Figs. 4.31 and 4.32 are maps of the simulated supersaturation cloud cover in January and July, respectively. There is a tendency for supersaturation clouds to be a maximum over the continents, but the seasonal changes are primarily dependent on latitude, and are perhaps seen more clearly in Fig. 4.18. The most notable seasonal

change is the one previously alluded to, namely, the change in the Southern Hemisphere subtropics, where there is a substantial increase in the supersaturation clouds in July.

5.   Summary

Atmospheric conditions during the calendar months of July have been simulated with a 44-day integration of the GISS model. The model-generated statistics during the month of July (days 14-44 of the integration) were stable, because of the realistic choice of initial conditions. The monthly mean statistics for the July simulation were compared with climatological data, mainly for the Northern Hemisphere troposphere. The comparison shows that the model-generated energy cycle, distribution of winds, temperature, humidity and pressure, dynamical transports, diabatic heating, evaporation, precipitation and cloud cover are all realistic for the Northern Hemisphere troposphere in July.

There are quantitative differences between the model-generated statistics and the climatological data, and these are generally similar to those found in the earlier January simulation (Somerville et al., 1974). In both seasons the simulations tend to underestimate the eddy activity, the strength of the mean meridional circulations, and some of the associated transports. However, the July simulation of the Northern Hemisphere on the whole is superior to the January simulation. In particular, the zonal mean temperature and zonal wind fields are in better agreement with the observed fields. This

improvement in the Northern Hemisphere simulation in July appears to be due to the absence of the polar night jet (which cannot be resolved with the model's stratospheric resolution), and to the decreased importance of large-scale dynamical heating and cooling in summer.

The model-simulated seasonal changes, determined by comparing the separate January and July simulations, were also evaluated by comparing them with climatological data. The model's simulation of seasonal changes is generally quite realistic, since the systematic quantitative errors referred to above do not affect the simulation of relative changes, to first order. For example, the northward displacement of the mid-latitude jets, the low-latitude Hadley cells, the tropical rain belt, the trade winds and the ITCZ in July, and the relative decrease in strength of the zonal and meridional circulations and in eddy activity in summer are all in good agreement with the observations. The simulated seasonal changes in the Southern Hemisphere are much smaller than in the Northern Hemisphere.

However, the simulation experiments do reveal three defects that could seriously bias its performance in particular climate experiments:

1) The north polar regions are as much as 10°K too cold in January. Errors of this magnitude would place the model at a disadvantage in simulating the amount and extent of polar ice and snow. The albedo of the polar ice and snow supplies a positive feedback to changes in solar radiation and is potentially an important mechanism for modifying climate (Sellers, 1969; Budyko, 1969; Gal-Chen and Schneider, 1975). Improvements in simulating arctic temperatures

will require improvements in simulating the dynamical transports. The
eddy flux of sensible heat by standing eddies appears to be at fault
in the January simulation, but the variability of different realiza-
tions of any individual transport averaged over a one-month period can
be substantial (Oort and Rasmusson, 1971). Consequently, we cannot be
sure that this particular flux needs improvement more than others. How-
ever, the deficiency in this flux in the January experiment does sug-
gest the need for improving the model's simulation of topography. The
deficiency in the arctic temperatures in January is a common defect in
GCM's (Holloway and Manabe, 1971; Kasahara et al., 1973; Newson, 1974).

2) The simulated climate in the vicinity of the Himalayas and
Southeast Asia is noticeably poorer than in other areas. For example,
the model's simulation of the Siberian High and the low-level winds
over the Bay of Bengal, Southeast Asia, and the Western Pacific in
January, and the model's simulation of the Himalayan Low and the pre-
cipitation rates over   Southeast Asia
in July are all sub-standard. The particular importance of topo-
graphy for the climate of this area -- i.e., the Himalayas -- again
suggests that the simulation of topographic effects needs to be im-
proved. Unusual difficulty in simulating the climate in this area
is again not unique to the GISS model (Manabe and Holloway, 1975).

3) The global albedo in the July simulation is abnormally high.
This defect leads to temperatures which are at most only 2°K too cold,
but this temperature error is kept small by the fact that sea surface
temperatures were prescribed to have their observed values. In many
climate calculations one needs to couple an ocean model to the atmo-
sphere model, and the temperature errors caused by such an albedo

error could then be substantially larger. The high albedo in the GISS model is caused at least in part by an excessive frequency of deep convective clouds in July. Correcting this defect will require improvements in the parameterization scheme for moist convection.

Acknowledgments

Figure and Table Captions

Table 2.1   Properties of cloud types generated in the model.

Fig. 2.1   Sea surface temperature field for July. Legend: 0, 0-9C; 1, 9-11C; 2, 11-13C; 3, 13-15C; 4, 15-17C; 5, 17-19C, 6, 19-23C; 7, 23-25C; 8, 25-27C; 9, above 27C.

Fig. 2.2   Global distribution of land (C), ice (I), and sea (blank) for July.

Fig. 2.3   Ground Wetness (per cent of saturation) for July. Legend: 0, 0-5%; 1, 5-15%; 2, 15-25%; 3, 25-35%; 4, 35-45%; 5, 45-55%; 6, 55-65%; 7, 65-75%; 8, 75-85%; 9, 85-100%; S, snow on land on July 1st; I, ice.

Fig. 3.1   Time evolution in the Northern Hemisphere model troposphere (layers 2-9) of the integrated zonal available potential energy (P_M), eddy available potential energy (P_E), eddy kinetic energy (K_E), and zonal kinetic energy (K_M). Units: $10^5 J\ m^{-2}$.

Fig. 3.2   Same as Fig. 3.1, but for the Southern Hemisphere, and the units of P_M have been changed to $10^6 J\ m^{-2}$.

Fig. 3.3   Computed and observed July zonal mean fields of zonal wind. Observed field is based on data from Oort and Rasmusson (1971). Units: $m\ sec^{-1}$. Negative (easterly) winds are shaded.

Fig. 3.4   Computed and observed July zonal mean fields of meridional wind. Observed field is based on data from Oort and Rasmusson (1971). Units: $m\ sec^{-1}$. Negative (southward) regions are shaded.

Fig. 3.5   Computed and observed July zonal mean field of vertical wind (omega). Observed field is based on data from Oort and Rasmusson (1971). Units: $10^{-4} mb\ sec^{-1}$. Negative (upward) regions are shaded.

Fig. 3.6   Computed and observed July zonal mean fields of temperature. Observed field is based on data from Oort and Rasmusson (1971). Units: °C. Negative regions are shaded.

Fig. 3.7   Computed and observed July zonal mean fields of potential temperature. Observed field is based on data from Oort and Rasmusson (1971). Units: K.

Fig. 3.8   Computed and observed July zonal mean fields of specific humidity. Observed field is based on data from Oort and Rasmusson (1971). Units: $g\ Kg^{-1}$.

Fig. 3.9   Computed and observed July zonal mean fields of northward transport of westerly momentum by eddies. Observed field is based on data from Oort and Rasmusson (1971). Units: $m^2 sec^{-2}$. Negative regions are shaded.

Fig. 3.10   Same as Fig. 3.9, but for northward transport of westerly momentum by the mean meridional circulations.

Fig. 3.11   Same as Fig. 3.9, but for northward transport of sensible heat by eddies. Units: $K \; m \; sec^{-1}$.

Fig. 3.12   Same as Fig. 3.9, but for northward transport of sensible heat by the mean meridional circulations. Units: $K \; m \; sec^{-1}$.

Fig. 3.13   Same as Fig. 3.9, but for northward transport of water vapor by eddies. Units: $g \; Kg^{-1} \; m \; sec^{-1}$.

Fig. 3.14   Same as Fig. 3.9, but for the northward transport of water vapor by the mean meridional circulations. Units: $g \; Kg^{-1} \; m \; sec^{-1}$.

Fig. 3.15   Computed and observed July zonal mean fields of variance of temperature due to eddies. Observed field is based on data from Oort and Rasmusson (1971). Units K^2.

Fig. 3.16   Computed July mean eddy kinetic energy (K_E) vs. wave-number. The slanted lines show a -3.0 slope.

Fig. 3.17   Computed July zonal mean field of heating rates due to solar radiation. Units: $K \; day^{-1}$.

Fig. 3.18   Computed July zonal mean field of cooling rates due to terretrial radiation. Units: $K \; day^{-1}$. Negative regions (regions of heating) are shaded.

Fig. 3.19   Computed July zonal mean field of heating rates due to large scale condensation and evaporation. Units: $K \; day^{-1}$. Negative regions (regions of net evaporation) are shaded.

Fig. 3.20   Computed July zonal mean field of heating rates due to parameterized sub-grid scale moist convection. Units: $K \; day^{-1}$. Negative regions are shaded.

Fig. 4.1   Simulated energy cycle for the Northern Hemisphere troposphere. a) January, b) July. Units: energy, 10^5 joules m^{-2}; conversions, watts m^{-2}.

Fig. 4.2   Observed energy cycle for the Northern Hemisphere troposphere from Oort and Peixoto (1974). a) January, b) July. Same units as Fig. 4.1.

Fig. 4.3   Same as Fig. 4.1, but for the Southern Hemisphere.

REFERENCES

Arakawa, A., 1972: Design of the UCLA atmospheric general circulation model. Tech. Rept. No. 7, Dept. of Meteorology, University of California at Los Angeles.

Arakawa, A., A. Katayama and Y. Mintz, 1969: Numerical simulation of the general circulation of the atmosphere. Proc. WMO/IUGG Symp. Numerical Weather Prediction, Tokyo, Japan Meteor. Agency, IV, 7, 8-12.

Budyko, M.I., 1963: Atlas of the Heat Balance of the Earth, Moscow, Gidrometeorizdat, 69 pp.

Budyko, M.I., 1969: The effect of solar radiation variations on the climate of the earth. Tellus, 21, 611-619.

Charney, J., P. H. Stone and W. J. Quirk, 1975: Drought in the Sahara: a biogeophysical feedback mechanism. Science, 187, 435-436.

Clapp, P. F., 1964: Global cloud cover for seasons using TIROS nephanalyses. Mon. Wea. Rev., 92, 495-507.

Crutcher, H. L., and J. M. Meserve, 1970: Selected Level Heights, Temperatures and Dew Points for the Northern Hemisphere. NAVAIR 50-1C-52, Naval Weather Service Command.

Deardorff, J. W., 1967: Empirical dependence of the eddy coefficient for heat upon stability above the lowest 50 m. J. Appl. Meteor., 6, 631-643.

Dopplick, T. G., 1972: Radiative heating of the global atmosphere. J. Atmos. Sci., 29, 1278-1294.

Druyan, L. M., 1974: Short-range forecasts with the GISS model of the global atmosphere. Mon. Wea. Rev., 102, 269-279.

Druyan, L. M., R. C. J. Somerville, and W. J. Quirk, 1976: Extended-range forecasts with the GISS model of the global atmosphere. Mon. Wea. Rev., in press.

Flattery, T. W., 1971: Spectral models for global analysis and forecasting. Air Weather Service Technical Report 242, pp. 42-54.

Gal-Chen, T., and S. H. Schneider, 1975: Energy balance climate modeling: comparison of radiative and dynamic feedback mechanisms. Tellus, in press.

Gates, W. L., 1972: The January global climate simulated by the two-level Mintz-Arakawa model: a comparison with observation. Rept. R-1005-ARPA, Rand Corporation.

Gates, W. L., 1975: The January global climate simulated by a two-level general circulation model: a comparison with observation. J. Atmos. Sci., 32, 449-477.

Godshall, F. A., 1968: Intertropical convergence zone and mean cloud amount in the tropical Pacific Ocean. Mon. Wea. Rev., 96, 172-175.

Gruber, A., 1971: Fluctuations in the position of the ITCZ in the Atlantic and Pacific Oceans. J. Atmos. Sci., 29, 193-197.

Haltiner, G. J., 1971: Numerical Weather Prediction. New York, Wiley, 317 pp.

Haurwitz, F., and W. R. Kuhn, 1974: The distribution of tropospheric planetary radiation in the Southern Hemisphere. J. Appl. Meteor., 13, 417-429.

Holloway, J. L., Jr., and S. Manabe, 1971: Simulation of climate by a global general circulation model: I. Hydrologic cycle and heat balance. Mon. Wea. Rev., 99, 335-370.

Jastrow, R., and M. Halem, 1973: Simulation studies and the design of the first GARP global experiment. Bull. Amer. Meteor. Soc., 54, 13-21.

Kasahara, A., T. Sasamori, and W. Washington, 1973: Simulation experiments with a 12-layer stratospheric global circulation model: I. Dynamical effect of the earth's orography and thermal influence of continentality, J. Atmos. Sci., 30, 1229-1251.

Kuo, H.-L., 1956: Forced and free meridional circulations in the atmosphere. J. Meteor., 13, 561-568.

Lacis, A. A., and J. E. Hansen, 1974: A parameterization for the absorption of solar radiation in the earth's atmosphere. J. Atmos. Sci., 31, 118-133.

Manabe, S., D. G. Hahn, and J. L. Holloway, Jr., 1974: The seasonal variation of the tropical circulation as simulated by a global model of the atmosphere. J. Atmos. Sci., 31, 43-83.

Manabe, S., and J. L. Holloway, Jr., 1975: The seasonal variation of the hydrologic cycle as simulated by a global model of the atmosphere. J. Geophys. Res., 80, 1617-1649.

Manabe, S., J. Smagorinsky, J. L. Holloway, Jr., and H. M. Stone, 1970: Simulated climatology of a general circulation model with hydrologic cycle: III. Effects of increased horizontal computational resolution. Mon. Wea. Rev., 98, 175-212.

Möller, F., 1951: Vierteljahrskarten des Niederschlags für die ganze Erde. Petermanns Geographische Mitteilungen, Gotha, Justus Perthes, 1-7.

Newson, R.L., 1974: An experiment with a tropospheric and stratospheric three-dimensional circulation model. Proc. 3rd Conference of the CIAP. Cambridge, U.S. Dept. of Transportation, pp. 461-473.

Ogura, Y. and H.-R. Cho, 1973: Diagnostic determination of cumulus cloud populations from observed large-scale variables. J. Atmos. Sci., 30, 1276-1286.

Oort, A. H., 1964: On estimates of the atmospheric energy cycle. Mon. Wea. Rev., 92, 483-493.

Oort, A. H., and J. P. Peixoto, 1974: The annual cycle of the energetics of the atmosphere on a planetary scale. J. Geophys. Res., 79, 2705-2719.

Oort, A. H., and E. M. Rasmusson, 1971: Atmospheric Circulation Statistics. NOAA Prof. Paper 5.

Peixoto, J. P., and A. H. Oort, 1974: The annual distribution of atmospheric energy on a planetary scale. J. Geophys. Res., 79, 2149-2159.

Ramage, C. S., 1971: Monsoon Meteorology, New York, Academic
     Press, 296 pp.

Riehl, M., 1954: Tropical Meteorology, New York, McGraw-Hill,
     515 pp.

Rodgers, C. D. 1967: The radiative heat budget of the troposphere
     and lower stratosphere. Rept. A2, Dept. of Meteorology,
     Massachusetts Institute of Technology, 99 pp.

Saltzman, B., 1970: Large-scale atmospheric energetics in the
     wavenumber domain. Rev. Geophys. Space Phys., 8, 289-302.

Sasamori, T., J. London and D. V. Hoyt, 1972: Radiation budget
     of the Southern Hemisphere. Meteor. Monogr., 13, No. 35,
     9-23.

Schneider, E. K., and R. S. Lindzen, 1976: A discussion of the
     parameterization of momentum exchange by cumulus convection.
     J. Geophys. Res., in press.

Schutz, C., and W. L. Gates, 1971: Global climatic data for
     surface, 800 mb. 400 mb: January Rept. R-915-ARPA, Rand
     Corporation.

Schutz, C., and W. L. Gates, 1972a: Supplemental global climatic
     data. January Rept. R-915/1-ARPA, Rand Corporation.

Schutz, C., and W. L. Gates, 1972b: Global climatic data for surface, 800 mb., 400 mb.: July Rept. R-1029-ARPA, Rand Corporation.

Sellers, W. D., 1969: A global climatic model based on the energy balance of the earth-atmosphere system. J. Appl. Meteor., 8, 392-400.

SMIC Report, 1971: Inadvertent Climate Modification. Cambridge, M.I.T. Press, 308 pp.

Somerville, R. C. J., W. J. Quirk, J. E. Hansen, A. A. Lacis, and P. H. Stone, 1976: A search for short-term meteorological effects of solar variability in an atmospheric circulation model. J. Geophys. Res., in press.

Somerville, R. C. J., P. H. Stone, M. Halem, J. E. Hansen, J. S. Hogan, L. M. Druyan, G. Russell, A. A. Lacis, W. J. Quirk, and J. Tenenbaum, 1974: The GISS model of the global atmosphere. J. Atmos. Sci., 31, 84-117.

Stone, P. H., S. Chow, H.M. Helfand, W. J. Quirk and R. C. J. Somerville, 1975: Seasonal changes in the atmospheric heat balance simulated by the GISS general circulation model. Proc. WMO/IAMAP, Symposium on Long-Term Climatic Fluctuations, Geneva, WMO Publ. No. 421, 383-389.

Stone, P. H., W. J. Quirk and R. C. J. Somerville, 1974: The effect of small-scale vertical mixing of horizontal momentum in a general circulation model. Mon. Wea. Rev., 102, 765-771.

Taljaard, J., H. Van Loon, H. Crutcher, and R. Jenne, 1969:
   Climate of the upper air: Southern Hemisphere, Vol. 1.
   NAVAIR 50-1C-55, Naval Weather Service Command.

Tenenbaum, J., 1976: Spectral and spatial energetics of the GISS
   model atmosphere. Mon. Wea. Rev., in press.

U. S. Navy Hydrographic Office, 1944: World Atlas of Sea Surface
   Temperatures. H. O. Pub. No. 225.

U. S. Navy Hydrographic Office, 1957: Oceanographic Atlas of the
   Polar Seas: Part I, Antarctic. H. O. Pub. No. 705.

U. S. Navy Hydrographic Office, 1958: Oceanographic Atlas of the
   Polar Seas: Part II, Arctic. H. O. Pub. No. 705.

Vonder Haar, T. H., and V. E. Suomi, 1971: Measurements of the
   earth's radiation budget from satellites during a five-year
   period. Part I: Extended time and space means. J. Atmos.
   Sci., 28, 305-314.

Washington, W. M., and L. G. Thiel, 1970: Digitized monthly mean
   ocean temperatures over the globe. Tech. Note 54, National
   Center for Atmospheric Research, 30 pp.

Webster, P. J., and J. L. Keller, 1975: Atmospheric variations:
   vacillations and index cycles. J. Atmos. Sci., 32, 1283-1300.

Wellck, R. E., A. Kasahara, W. M. Washington, and G. Santo, 1971:
   Effect of horizontal resolution in a finite-difference model
   of the general circulation. Mon. Wea. Rev., 99, 673-683.

TABLE 2.1

PROPERTIES OF CLOUDS IN THE GISS MODEL

Cloud Type	Layers	Analogy	Optical Thickness	Albedo
supersaturation	2	Ci	1	.12
supersaturation	3	Ci	2	.21
supersaturation	4	As	4	.34
supersaturation	5 or 6	As	6	.44
supersaturation	7 or 8 or 9	St	8	.51
penetrating convection	4-7 or 5-8 or 6-9	Cb	32	.81
middle level convection	5 or 6	Ac	8	.51
low level convection	7 or 8	Cu	16	.68

Fig. 2.1

Fig.2.2
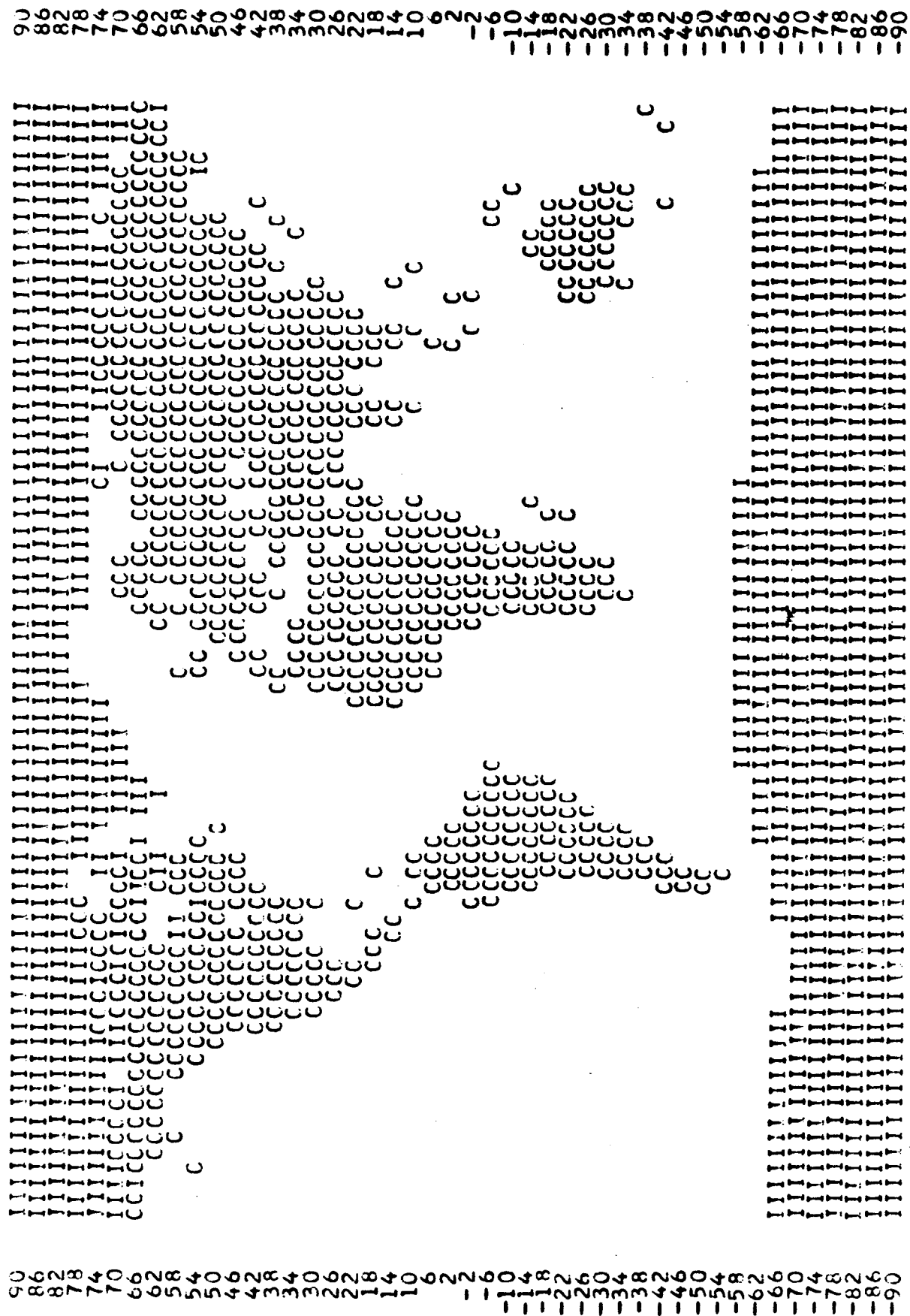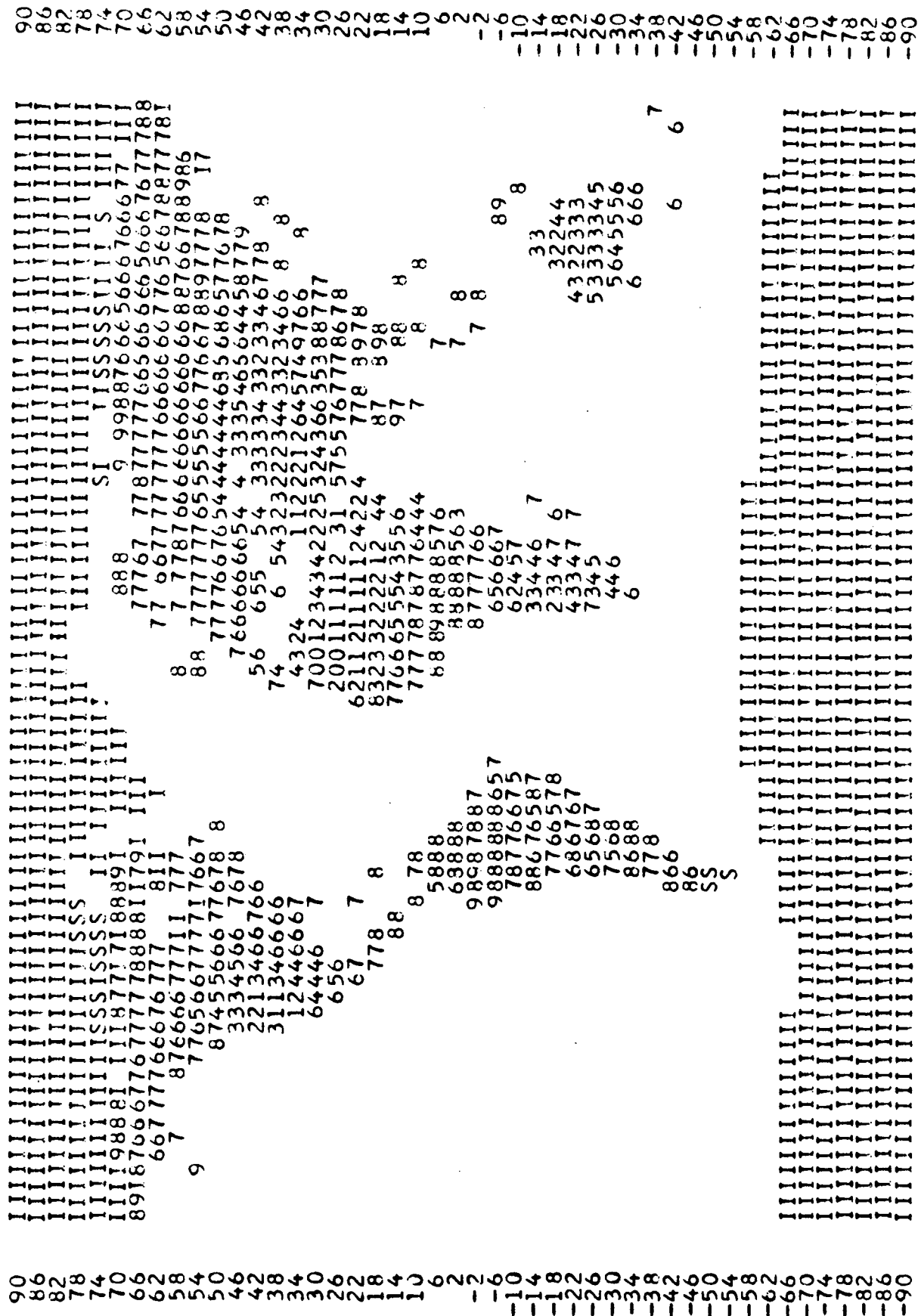
Fig.2.3
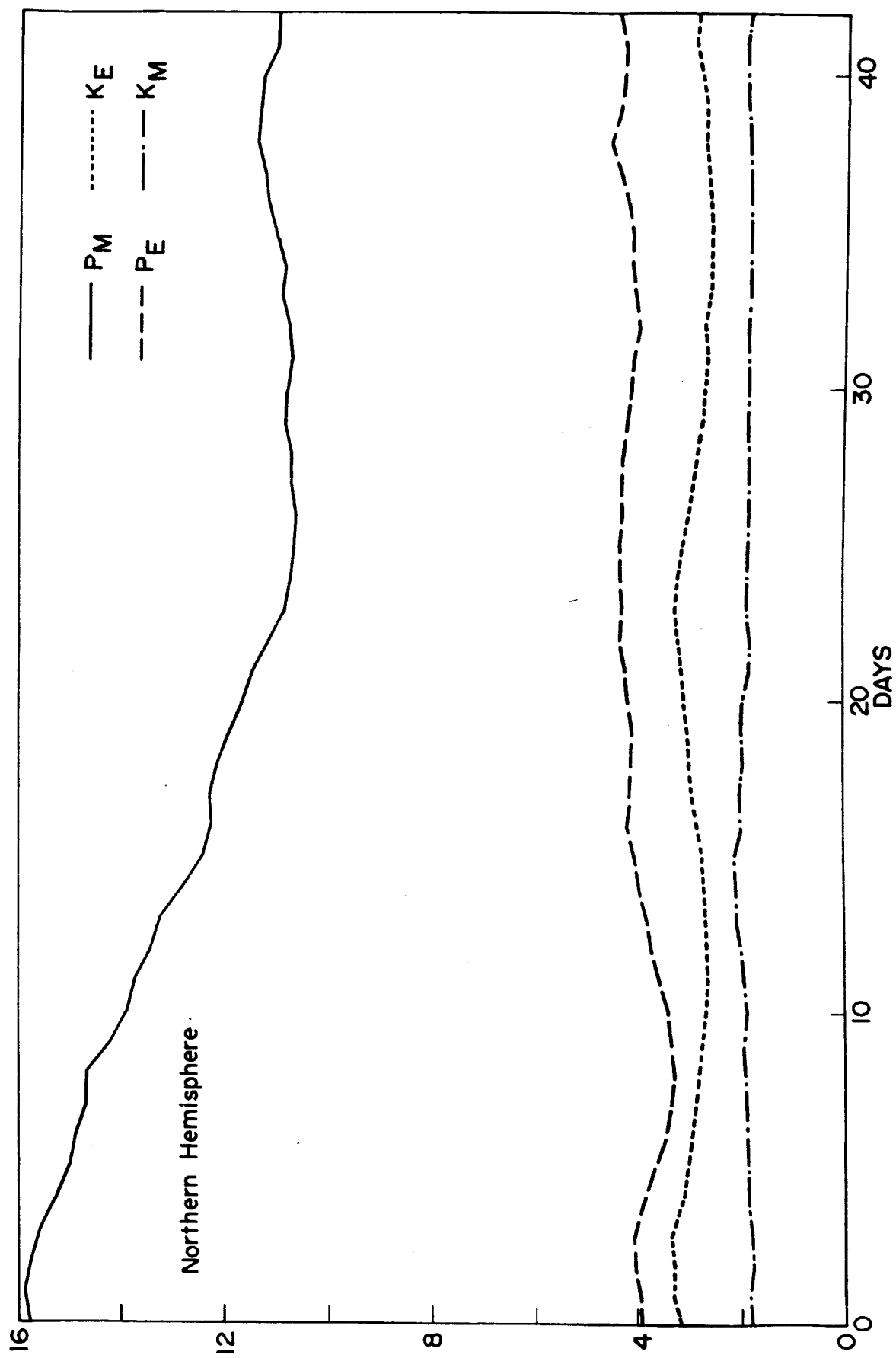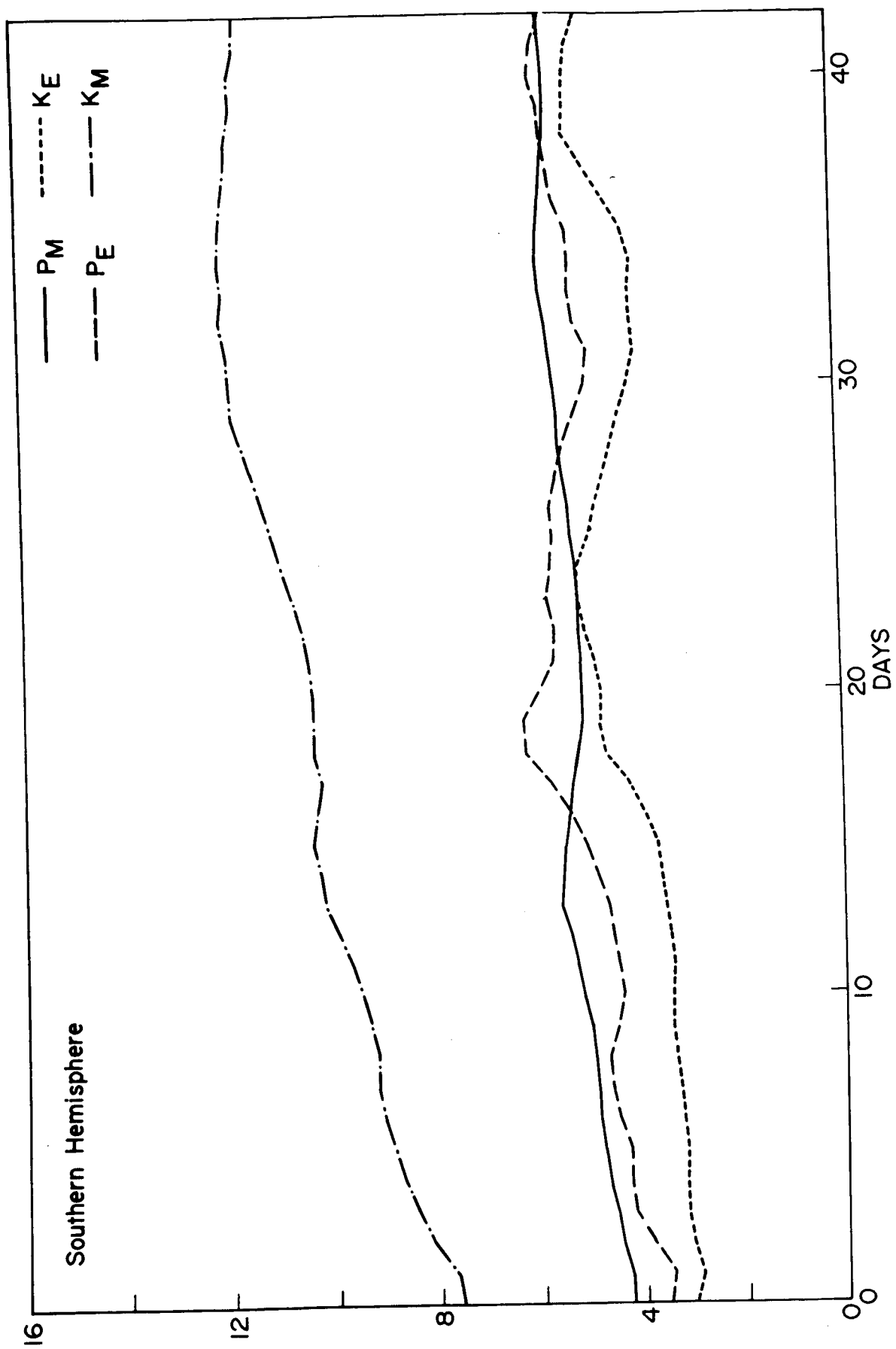
Fig. 3.1

Fig. 3.2

Fig.3.3

Fig.3.4

Fig. 3.5

COMPUTED

OBSERVED
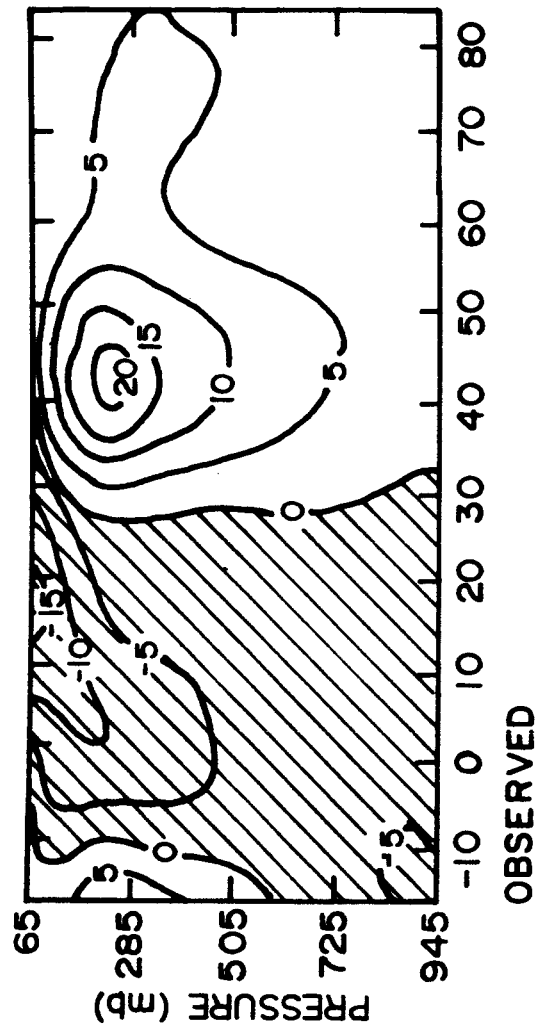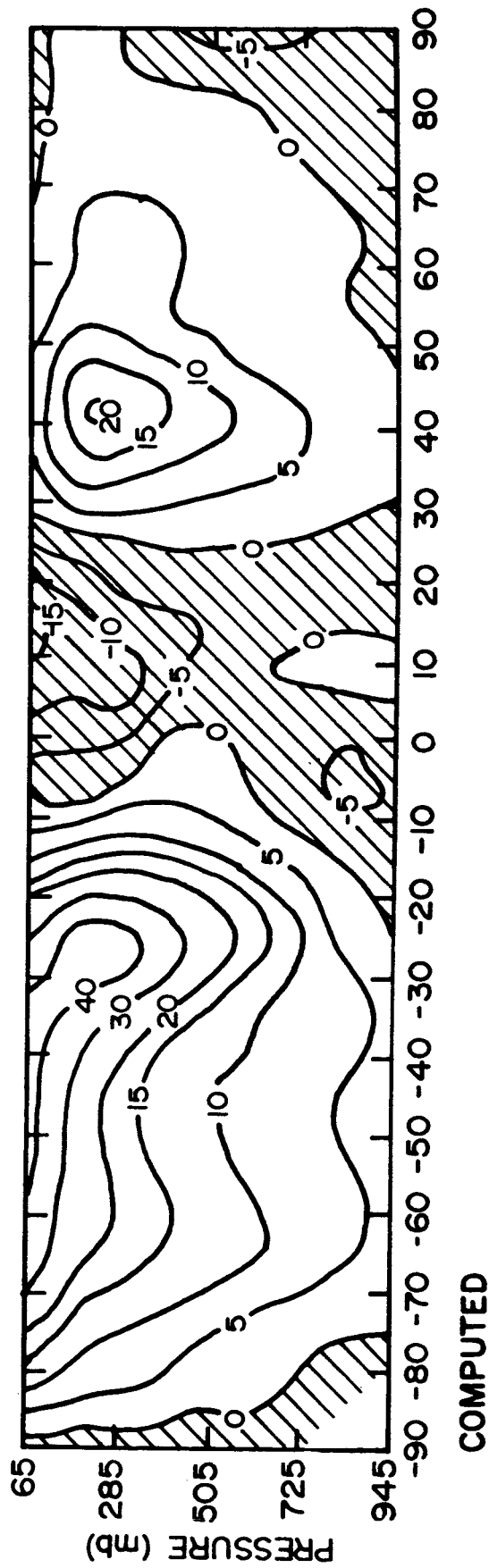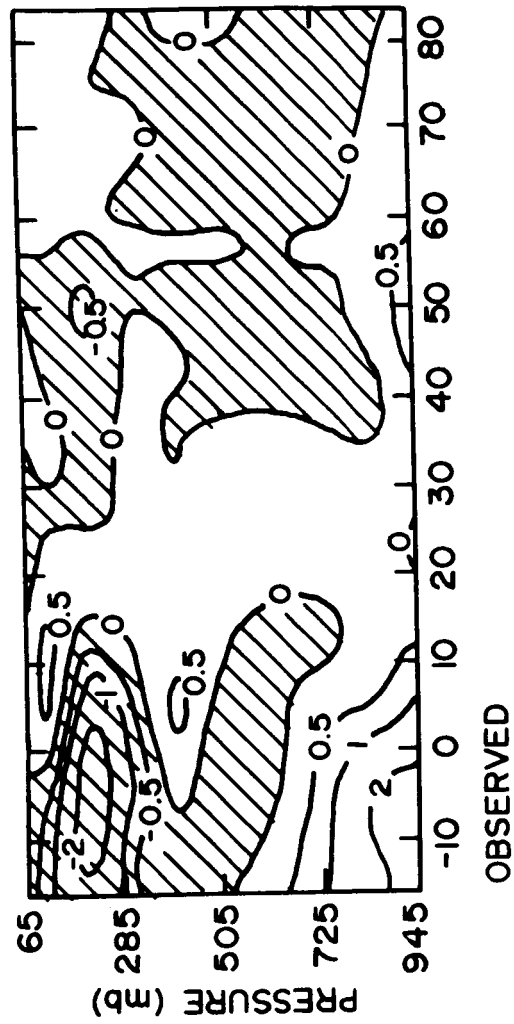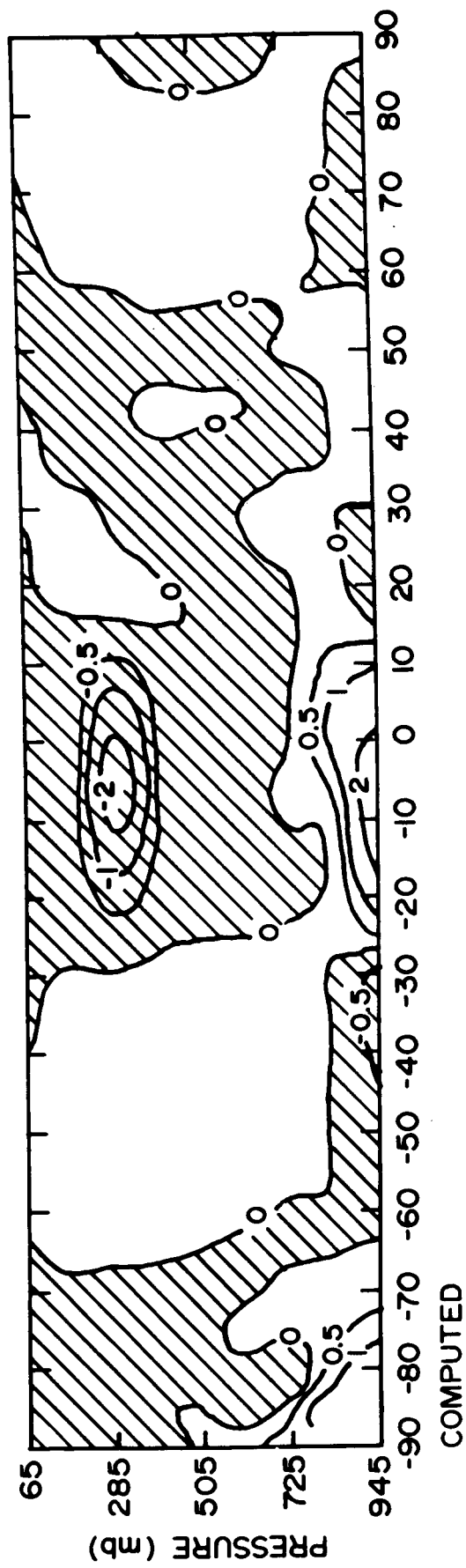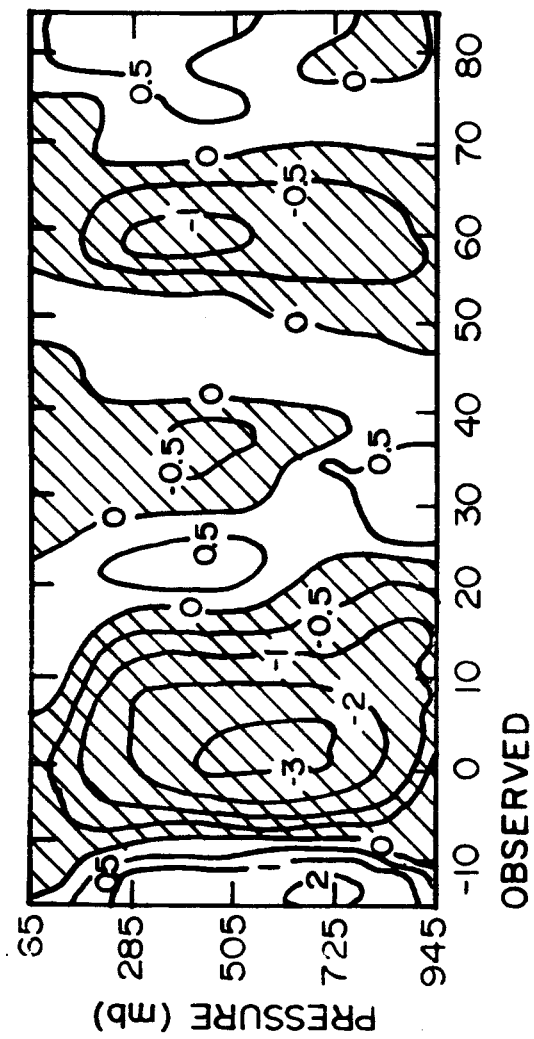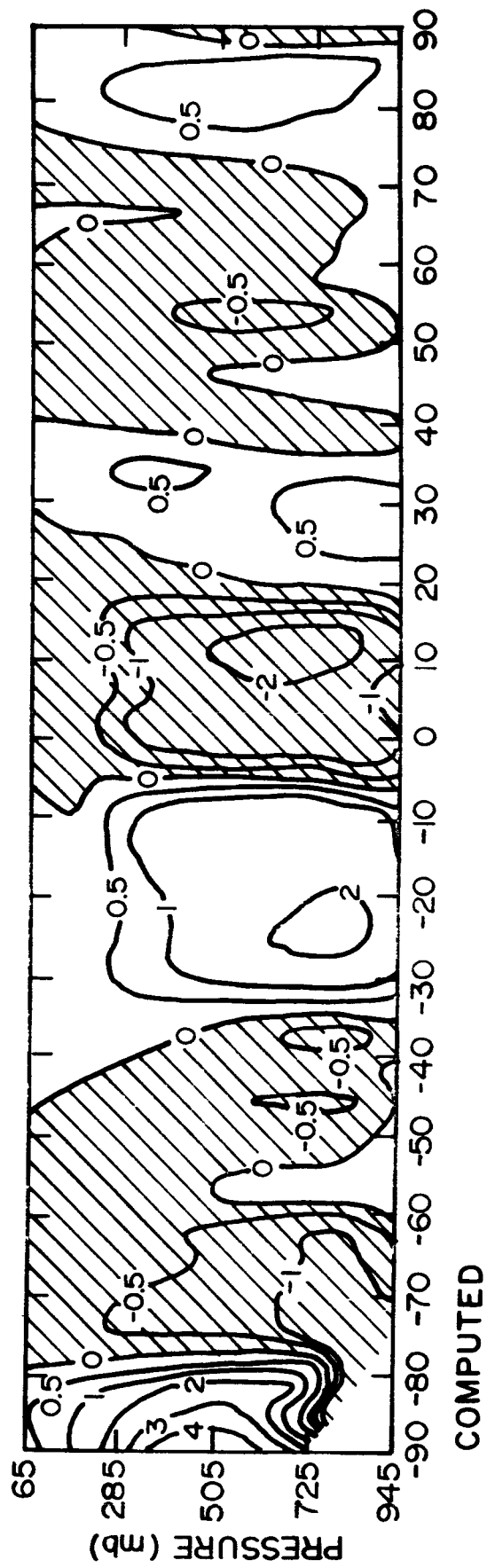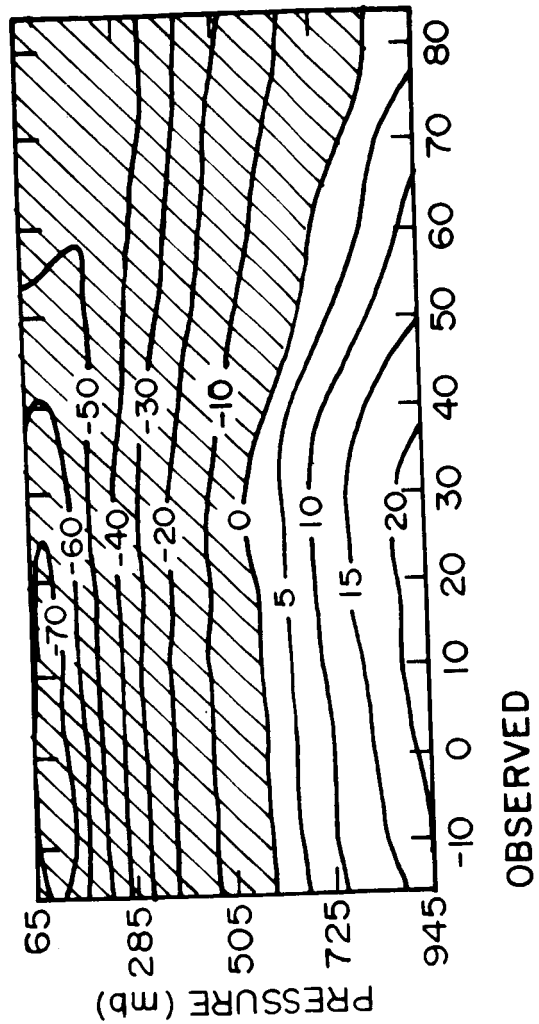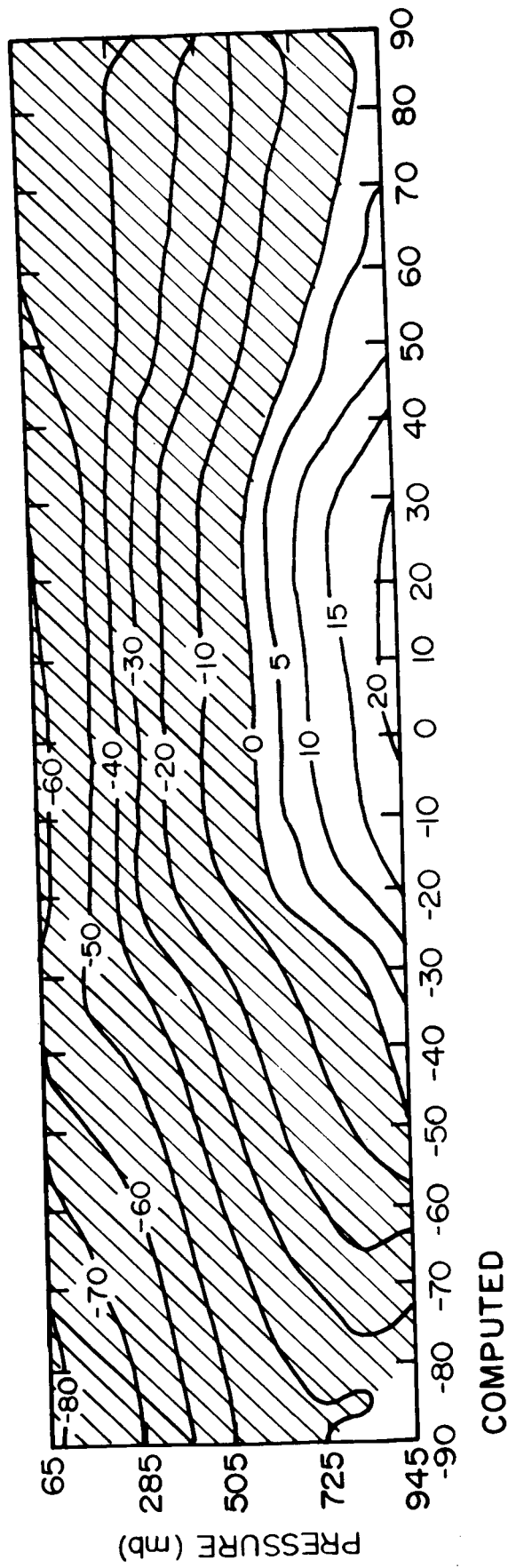
Fig.3.6
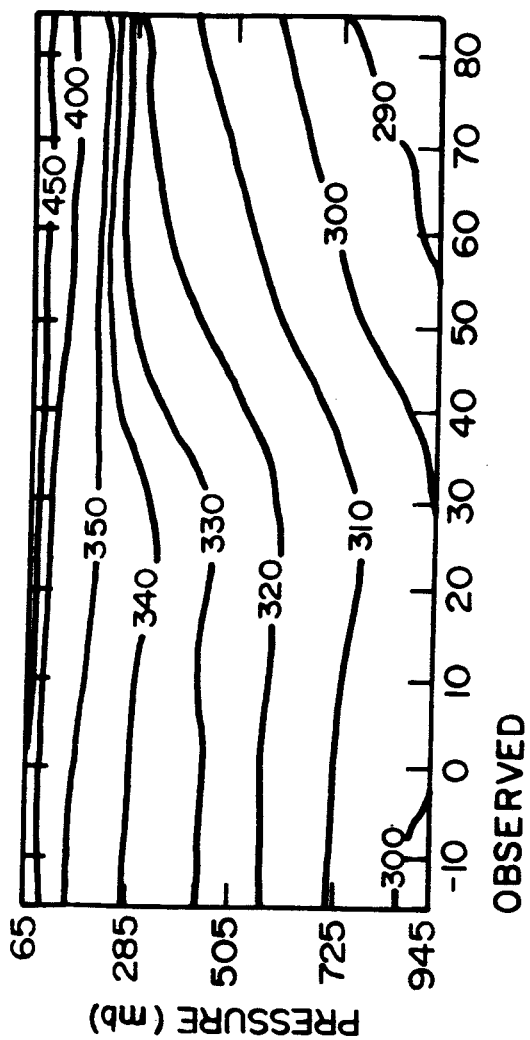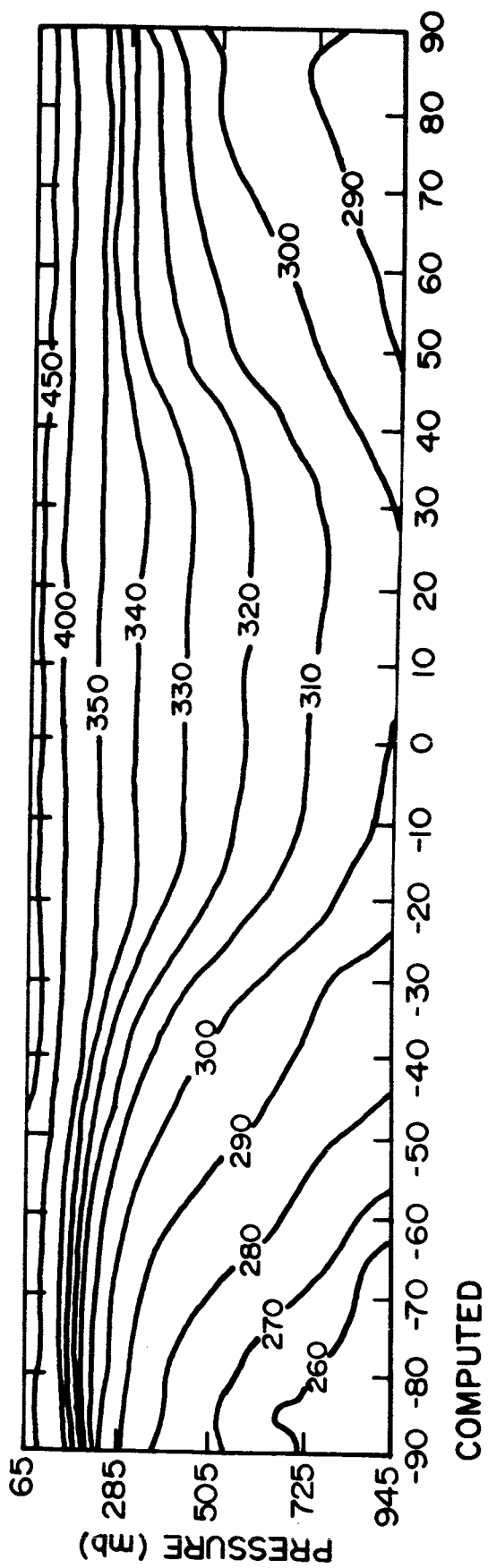
Fig. 3.7
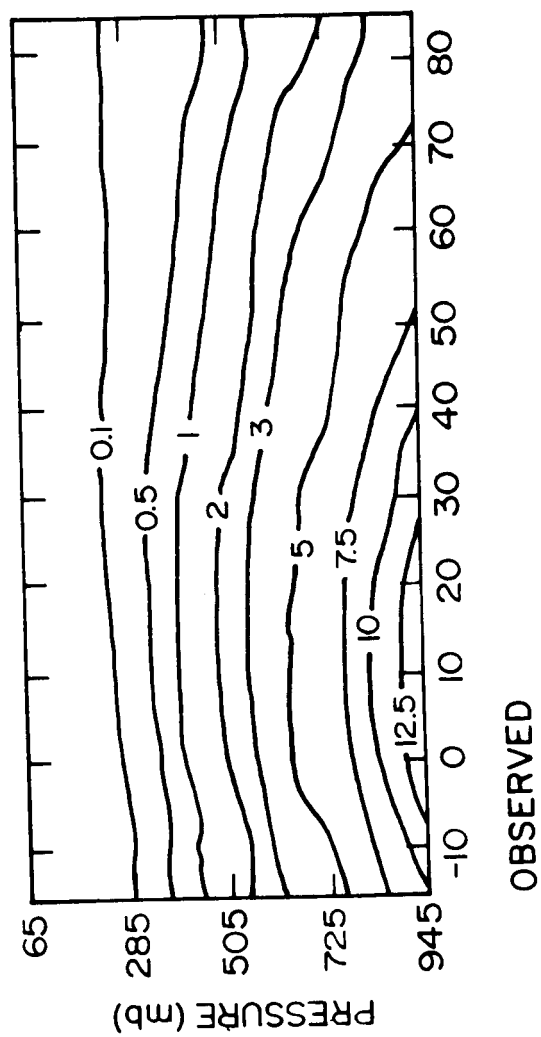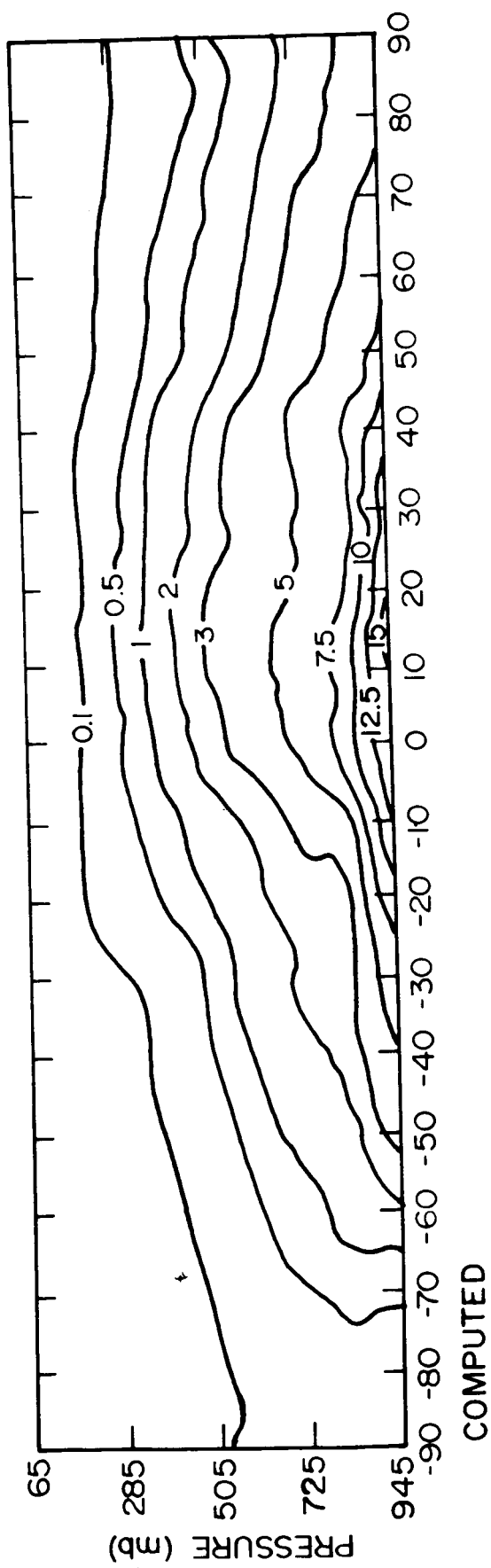
Fig. 3.8
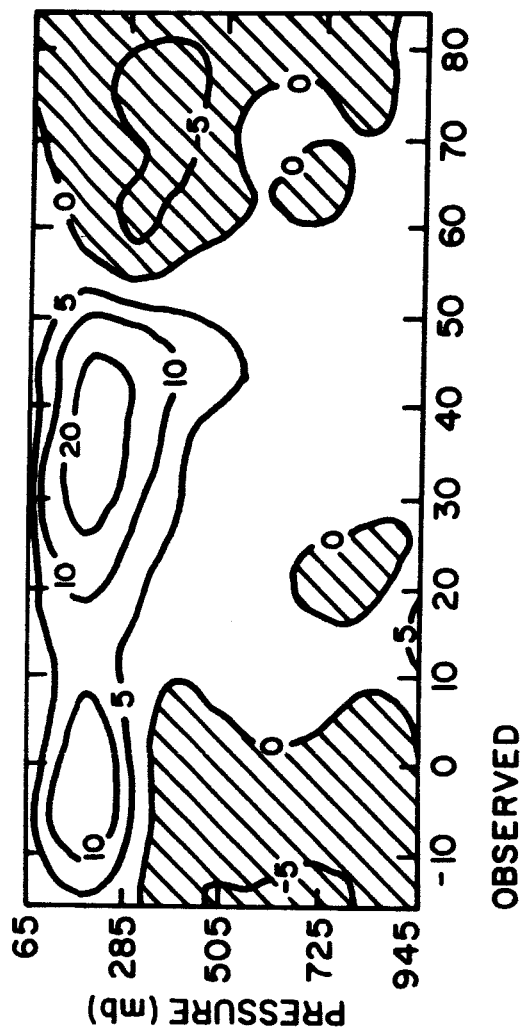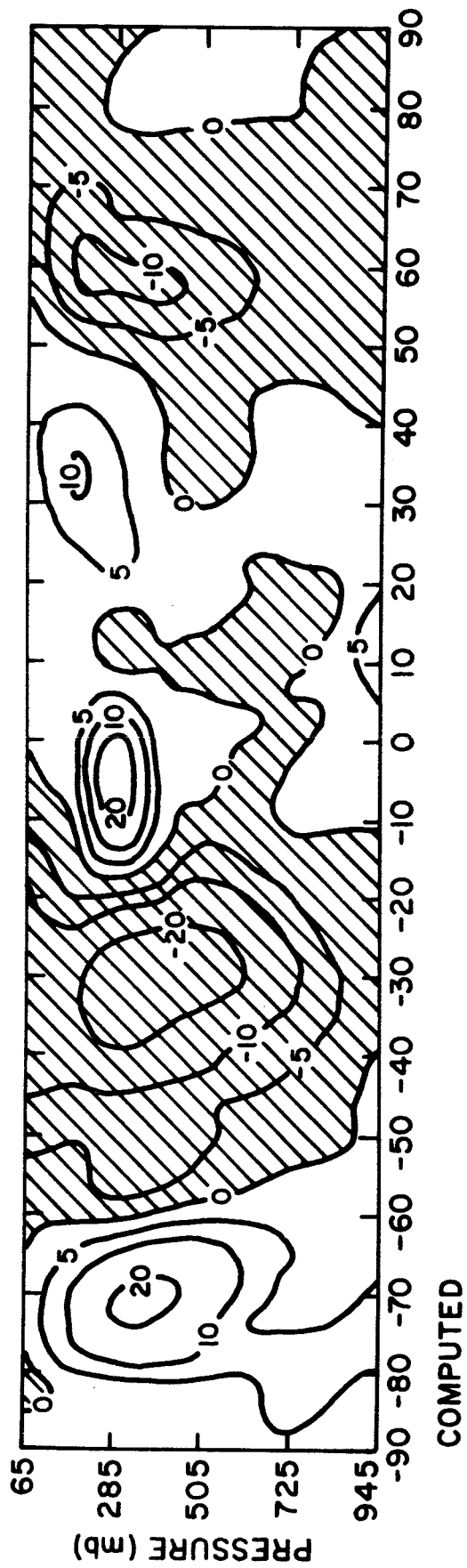
Fig.3.9
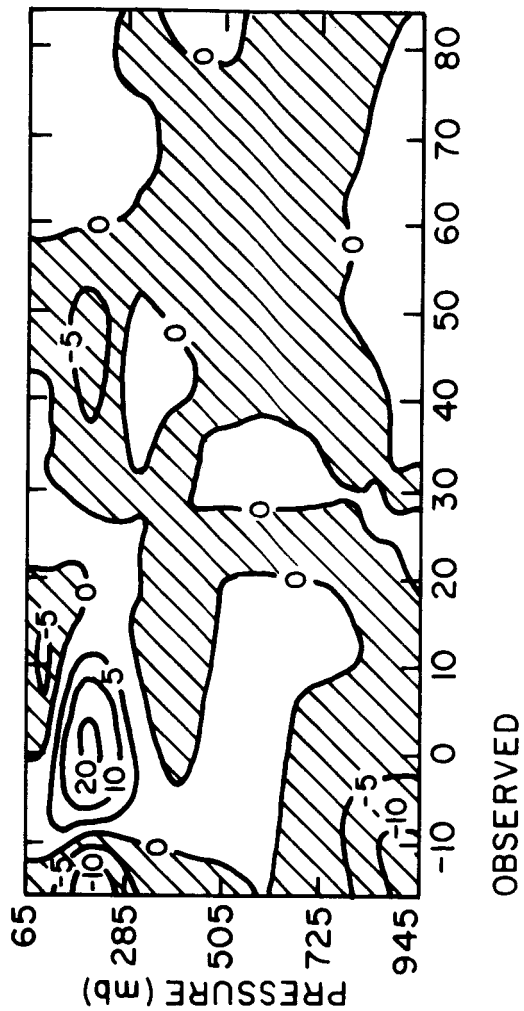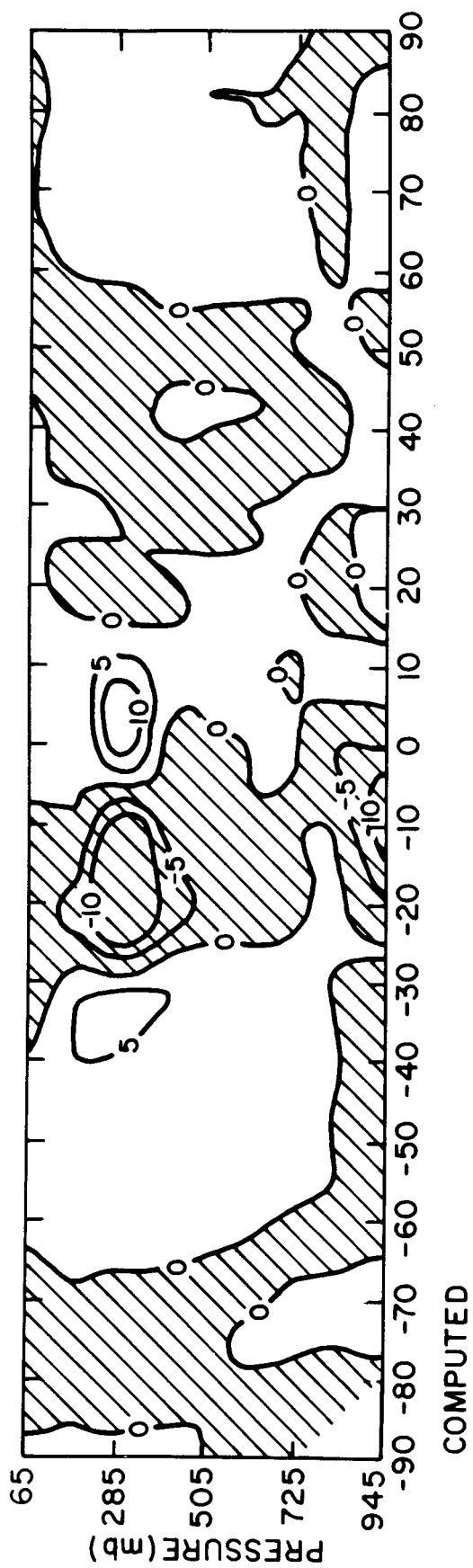
Fig. 3.10
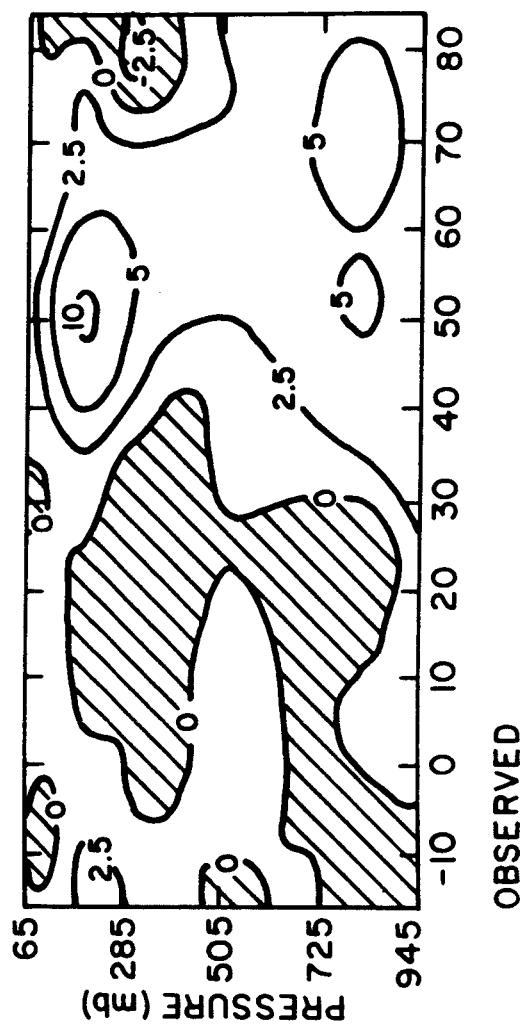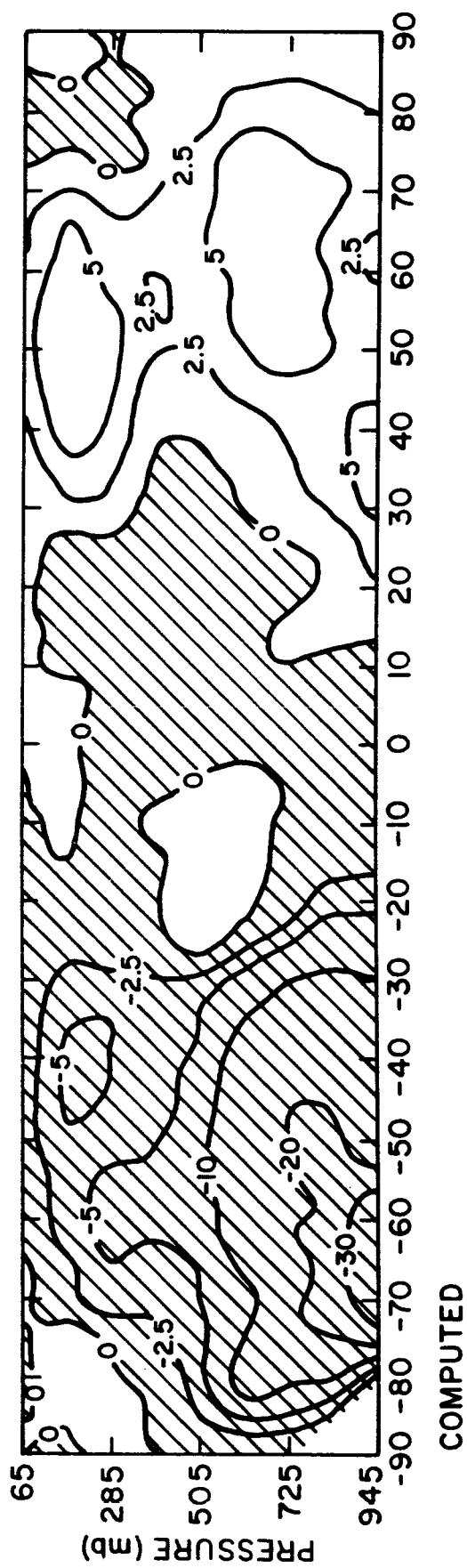
Fig. 3.11

Fig. 3.12

Fig. 3.13

COMPUTED

OBSERVED
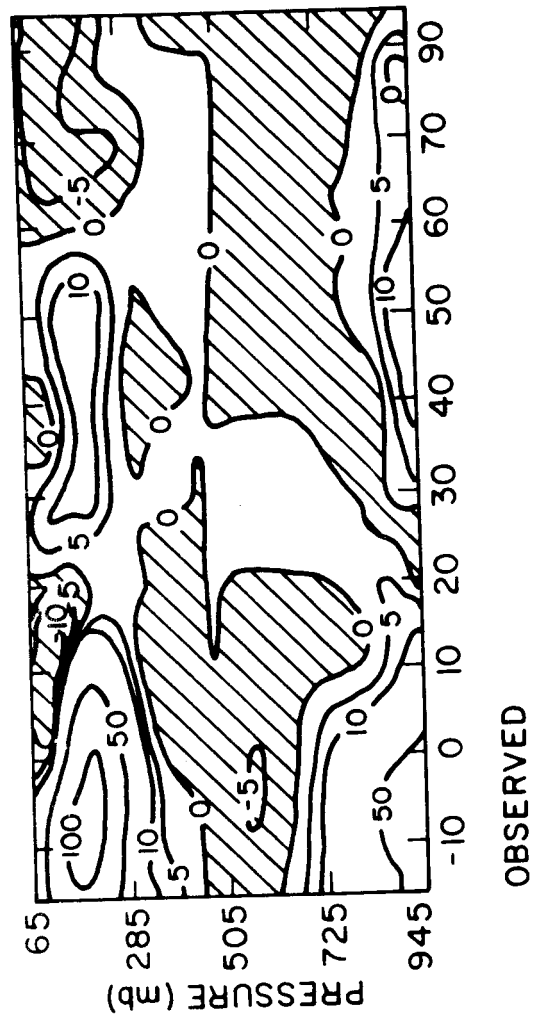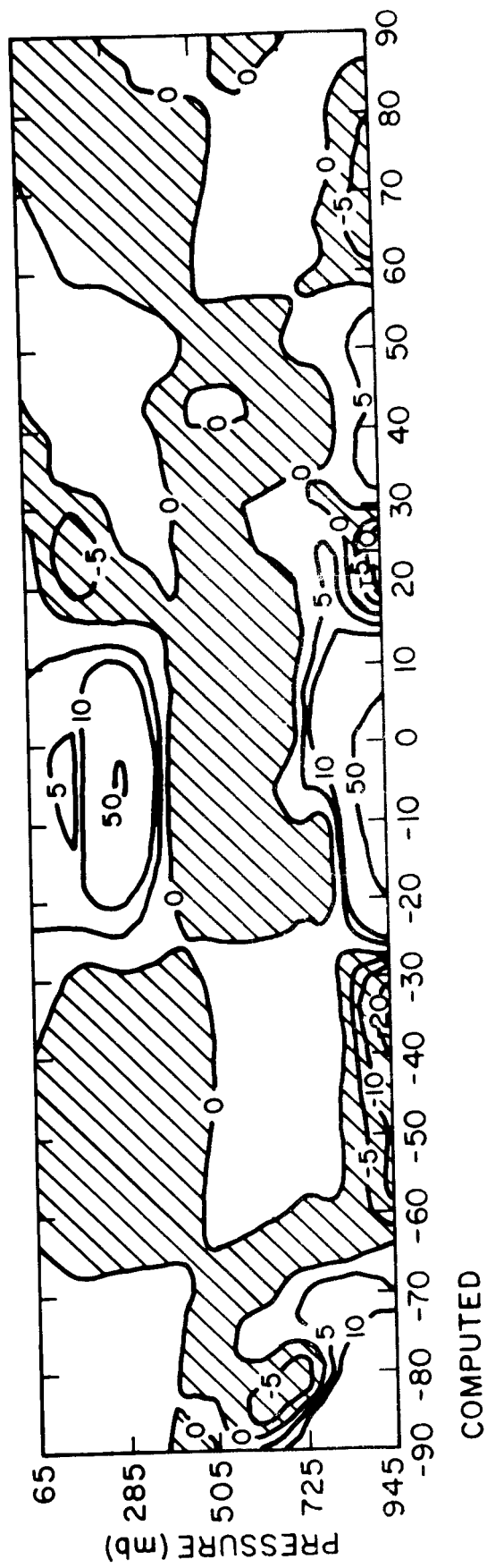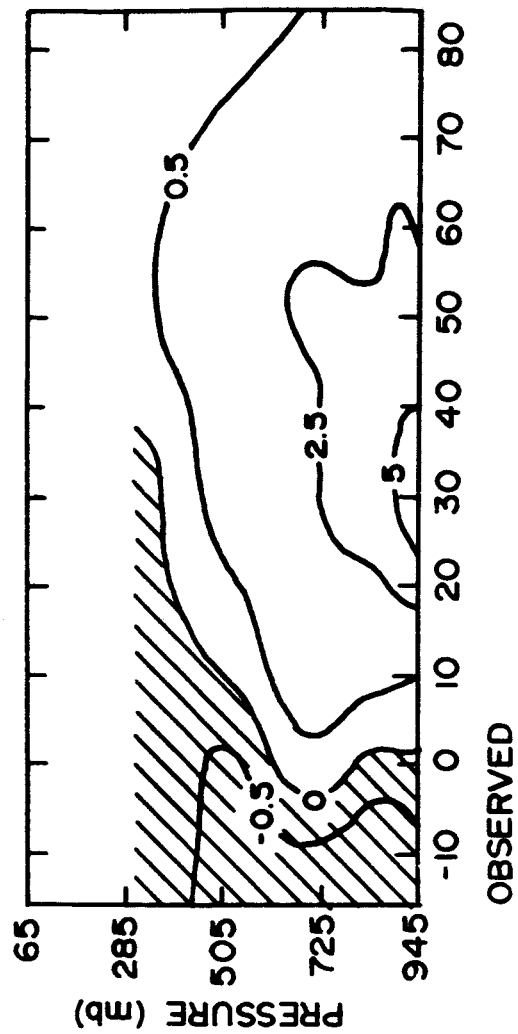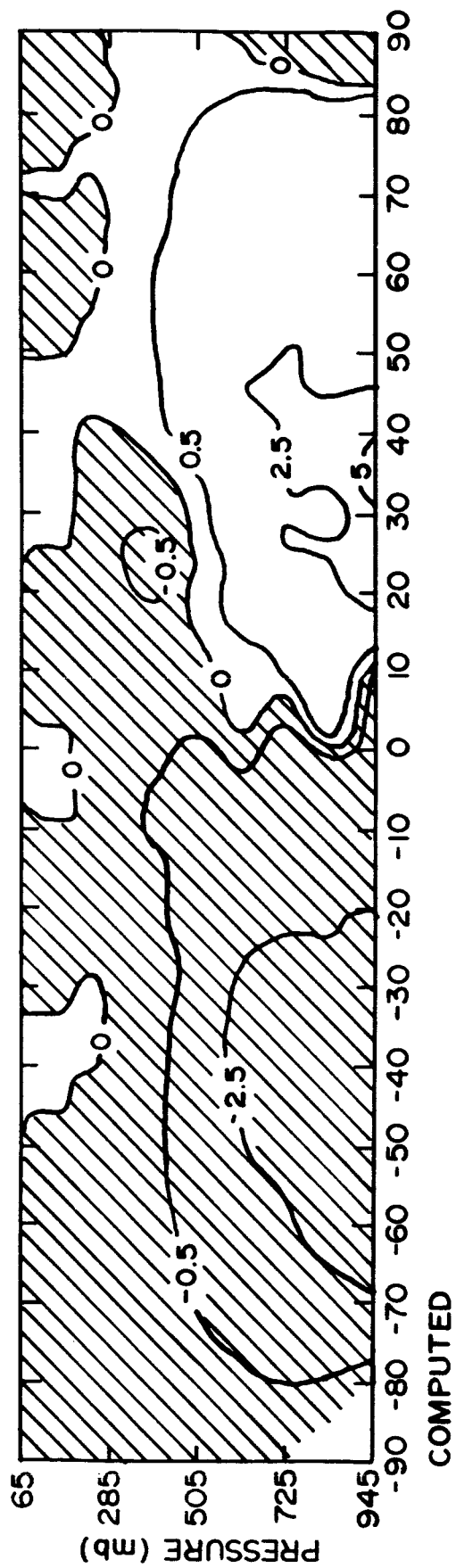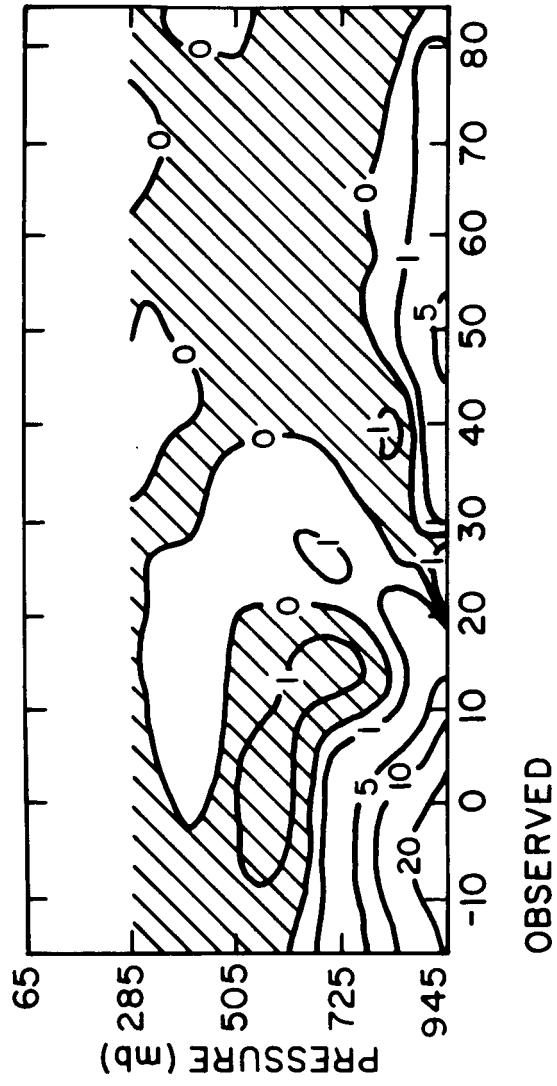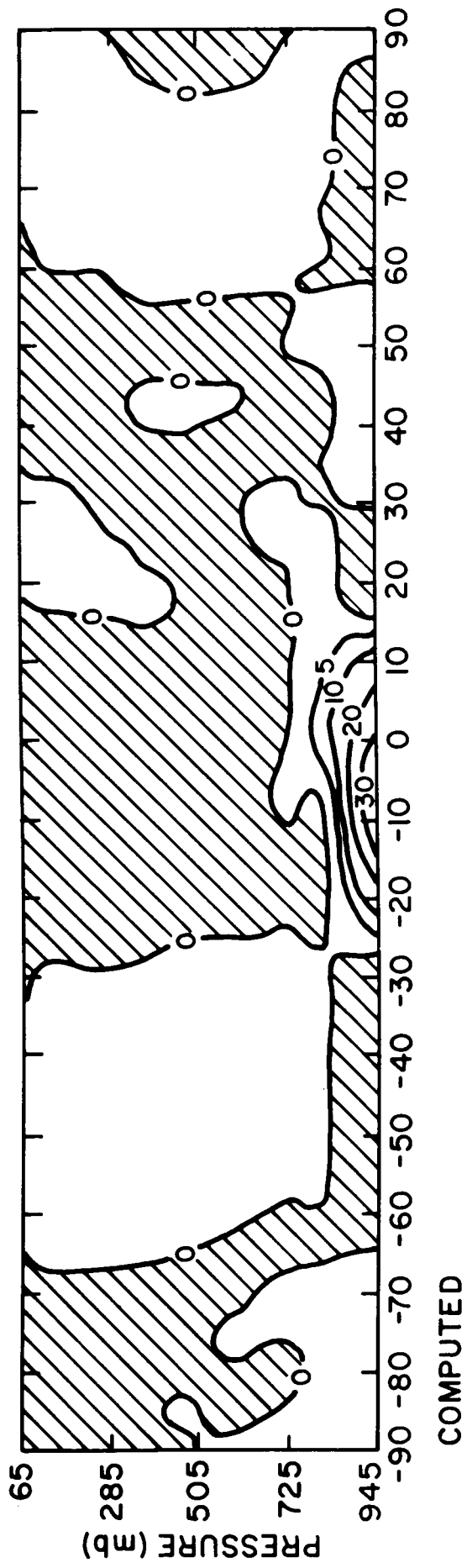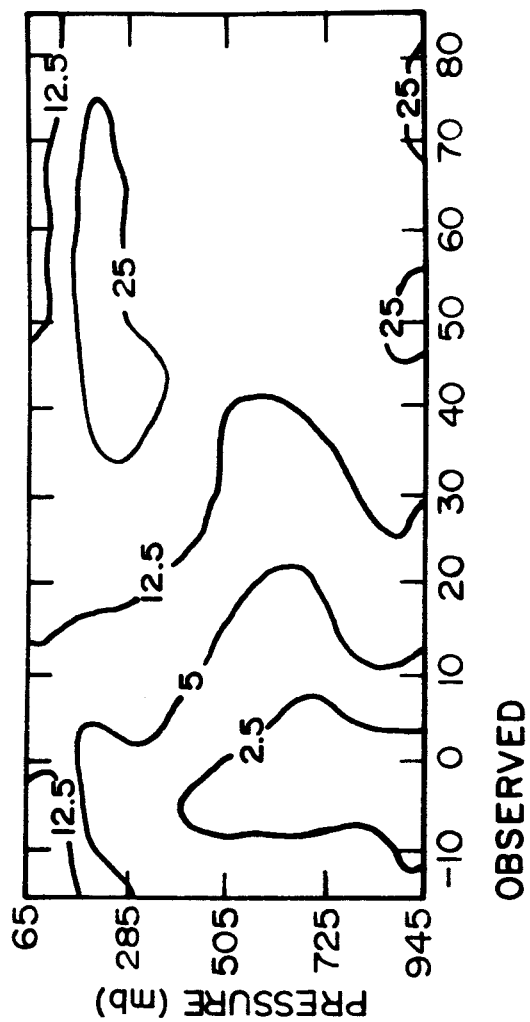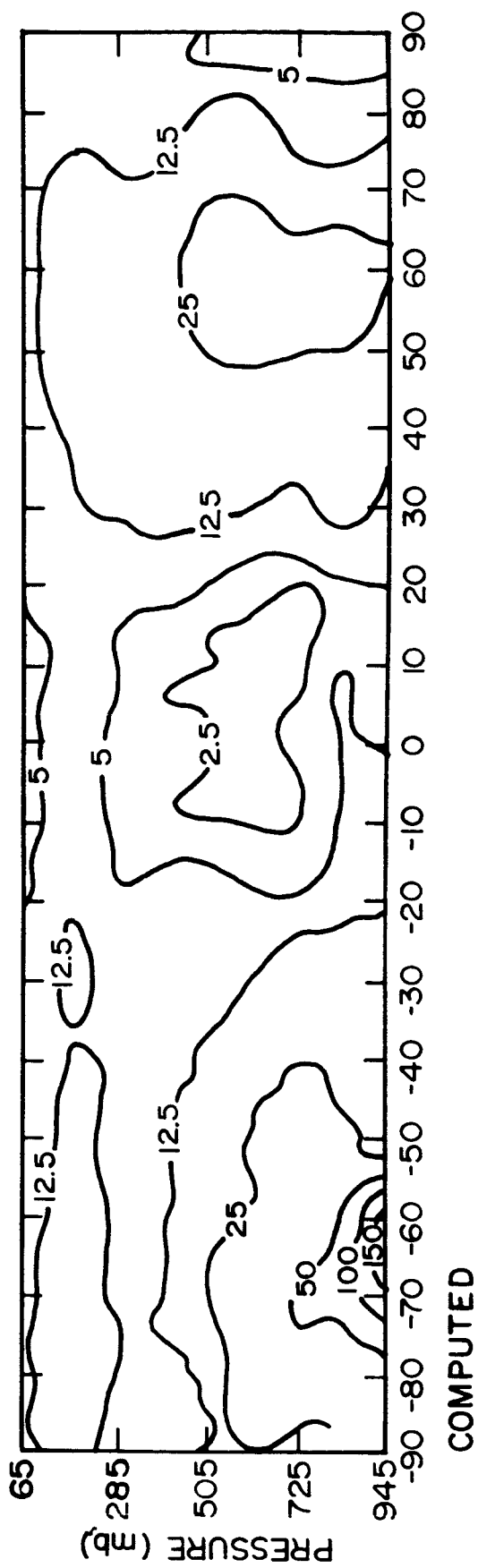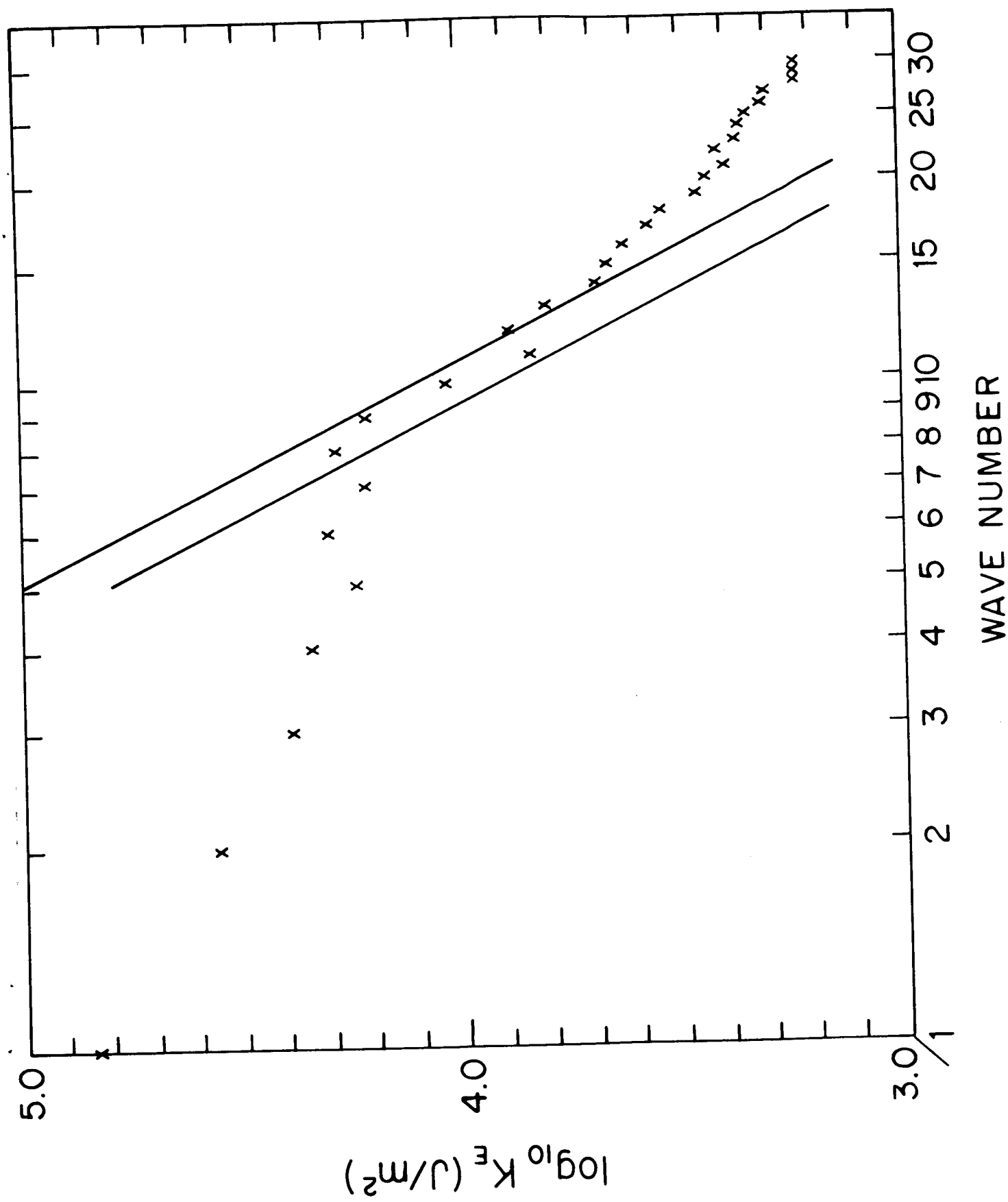
Fig. 3.14

Fig. 3.15

Fig.3.16
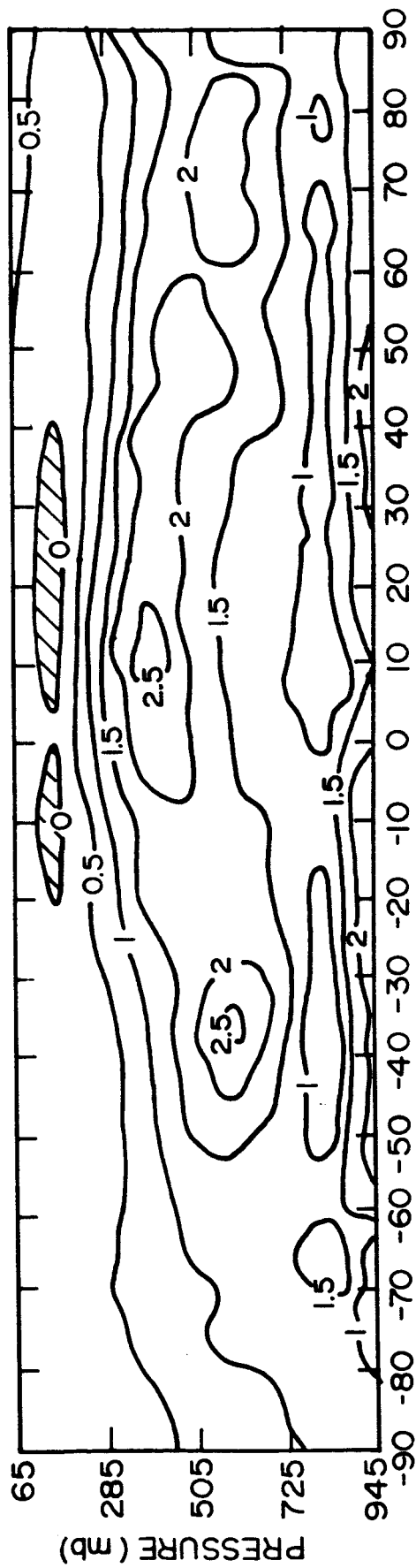
Fig. 3.18
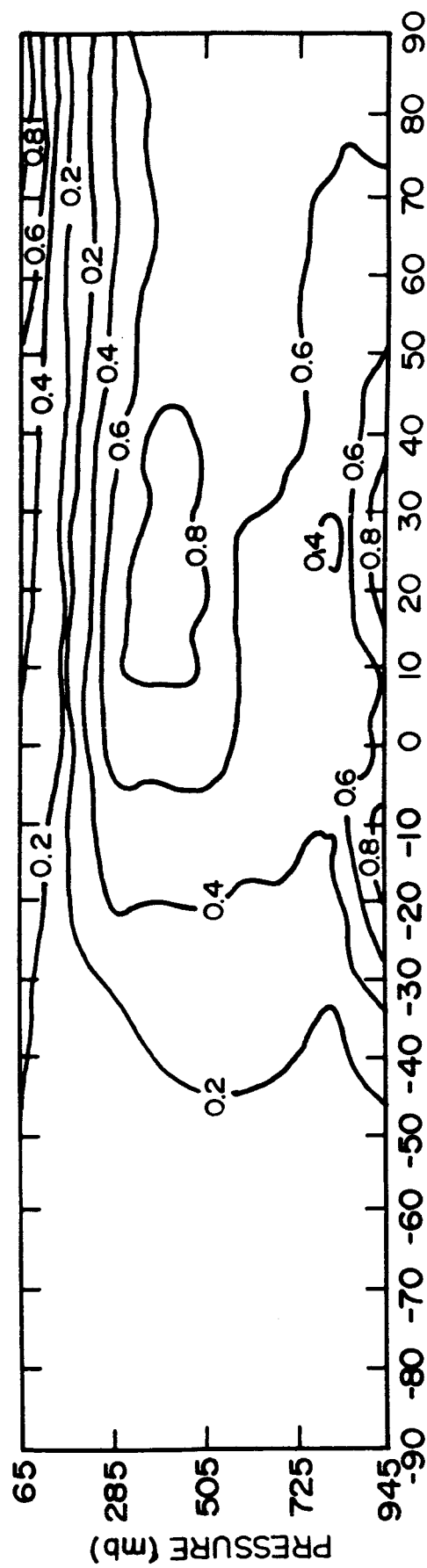
Fig. 3.17

Fig. 3.20

Fig. 3.19

Fig. 4.1a

G(P_M)=1.9

D(K_M)=-0.07

C(P_M,K_M) =0.5

P_M =11.2

K_M =1.8

C(P_M,P_E)=0.4

C(K_E,K_M)=0.06

C(P_E,K_E) =1.9

P_E =4.4

K_E =3.0

G(P_E)=1.6

D(K_E)=-1.3

Fig. 4.1b

Fig. 4.2a

Fig. 4.2 b

$G(P_M) = 2.2$

$D(K_M) = -0.4$

$C(P_M, K_M)$

$P_M = 27.9$

$K_M = 4.8$

$= +0.02$

$C(P_M, P_E) = 1.2$

$C(K_E, K_M) = 0.3$

$C(P_E, K_E)$

$P_E = 3.8$

$K_E = 3.3$

$= 1.9$

$G(P_E) = 1.0$

$D(K_E) = -1.5$
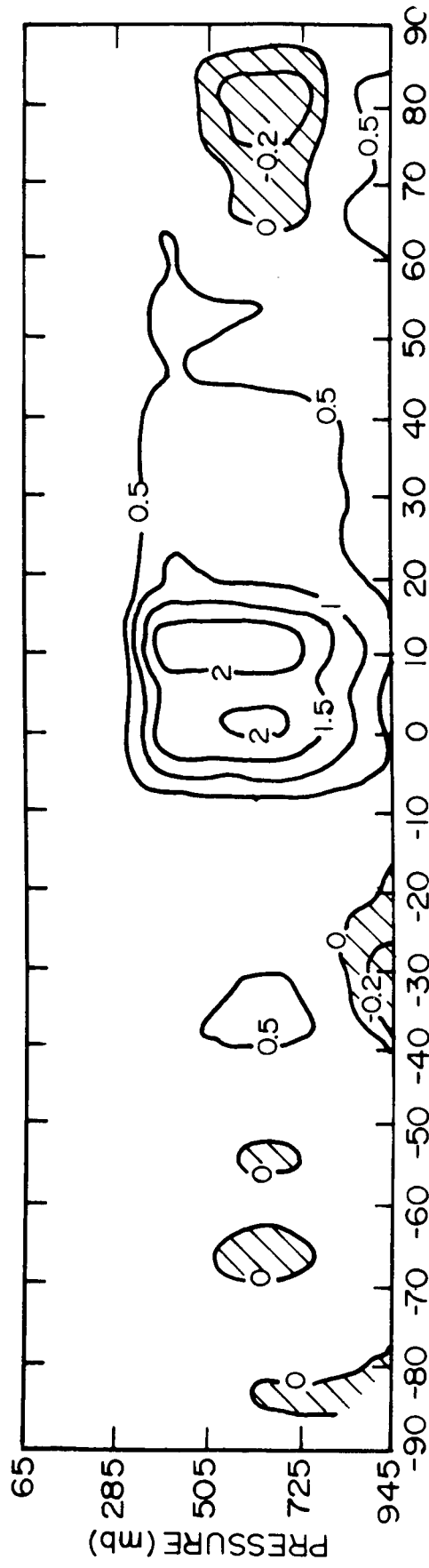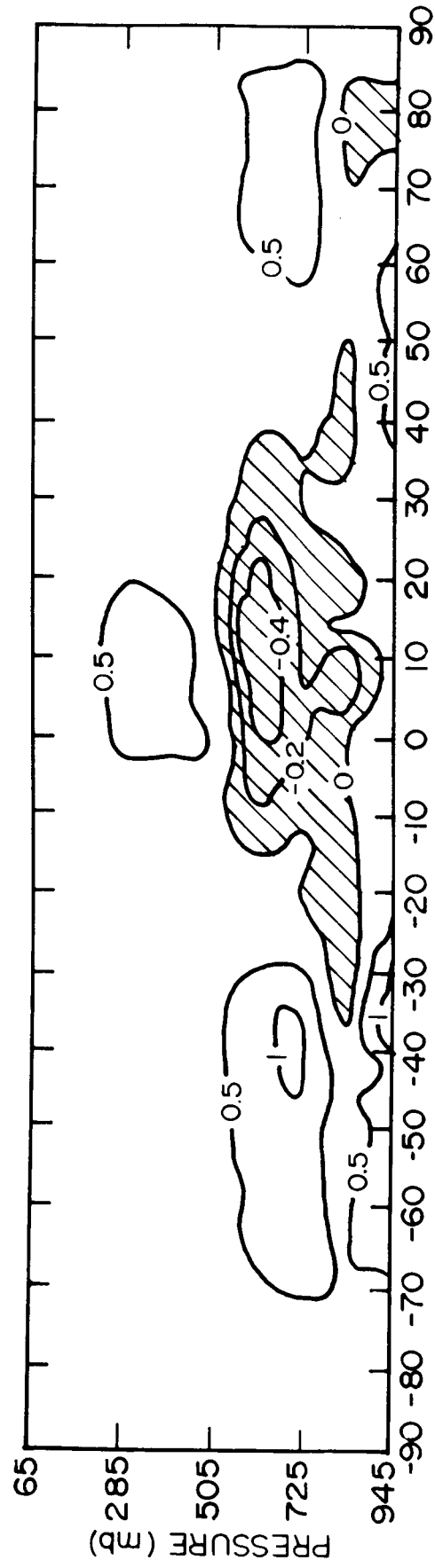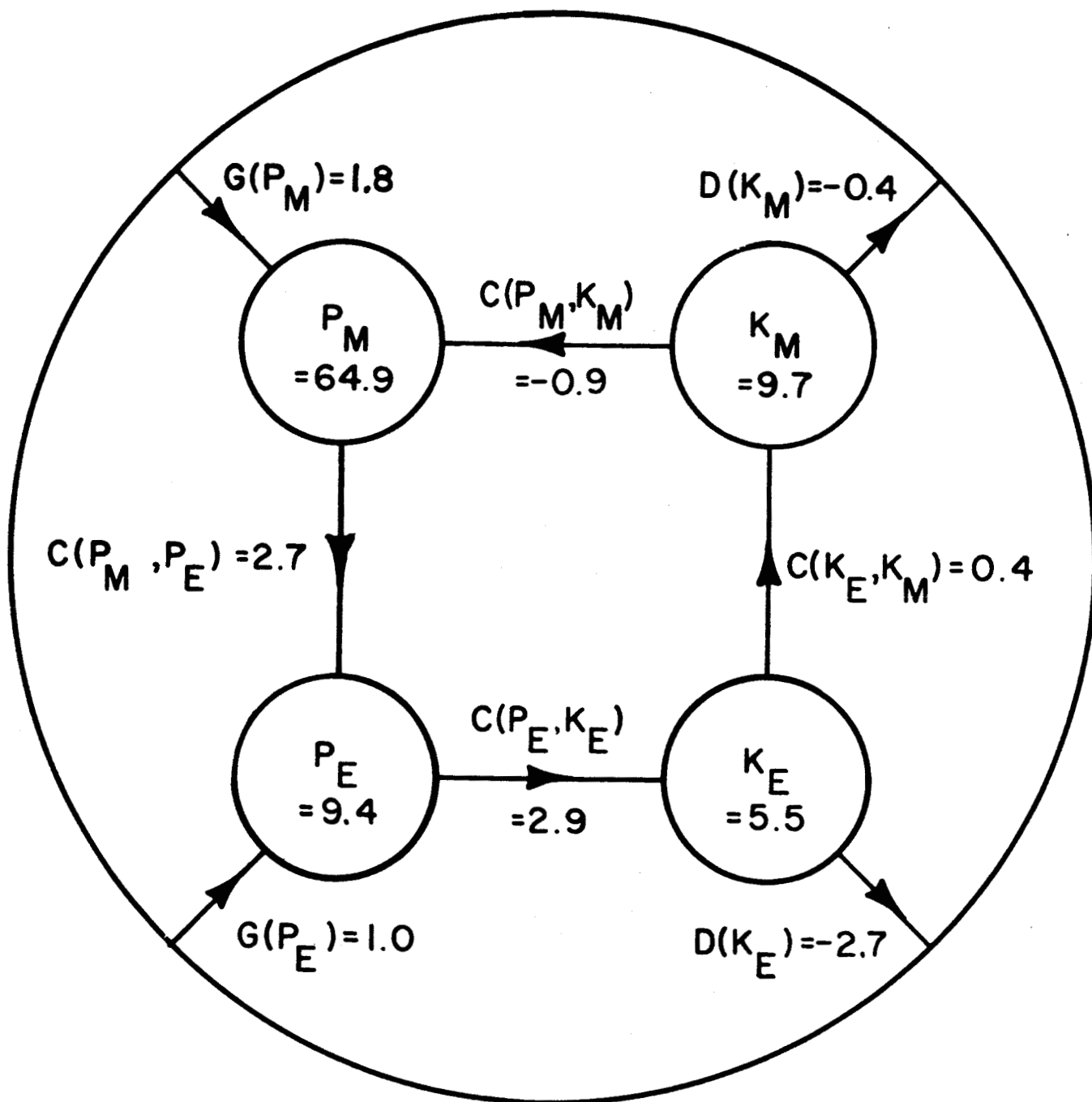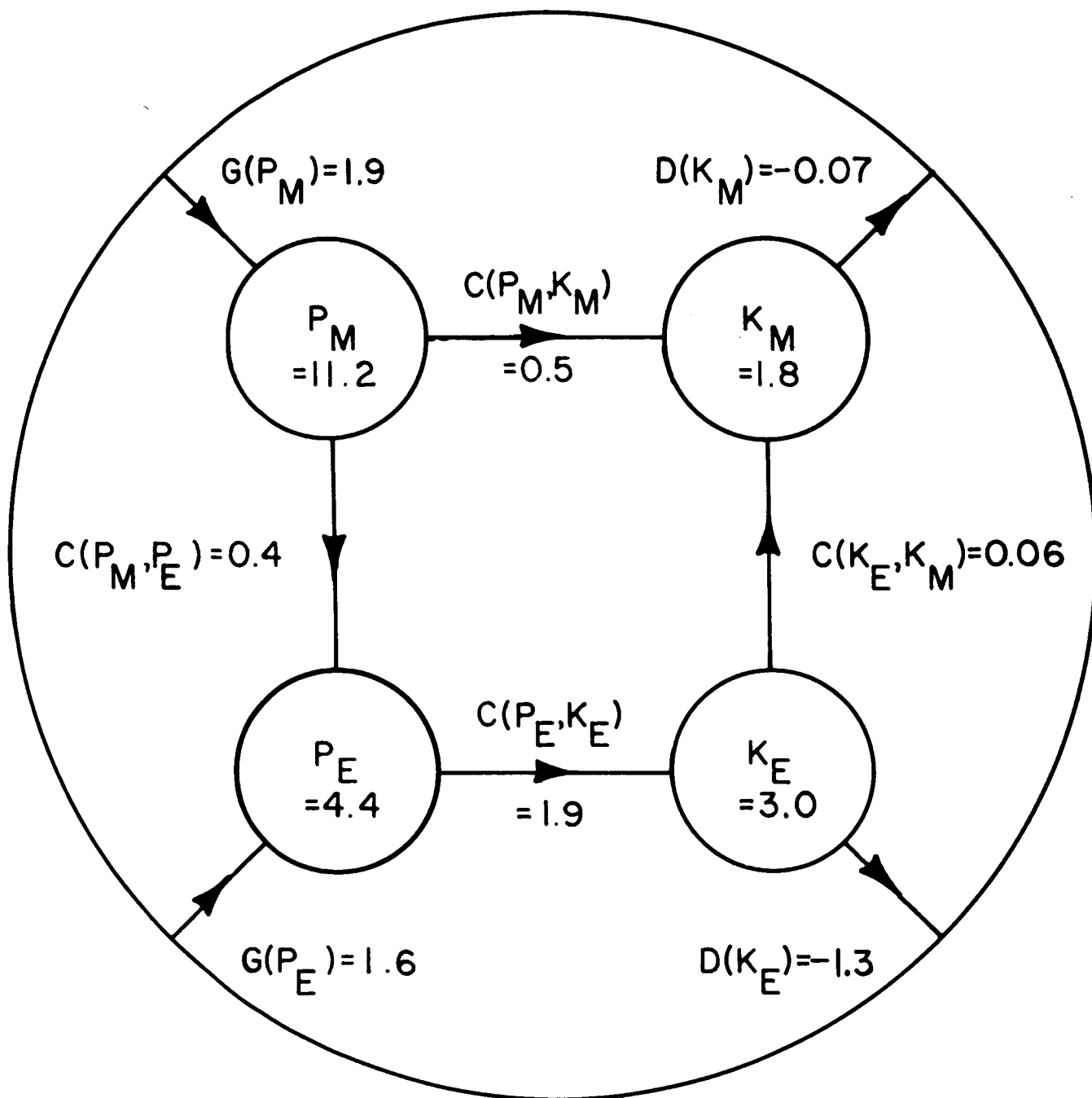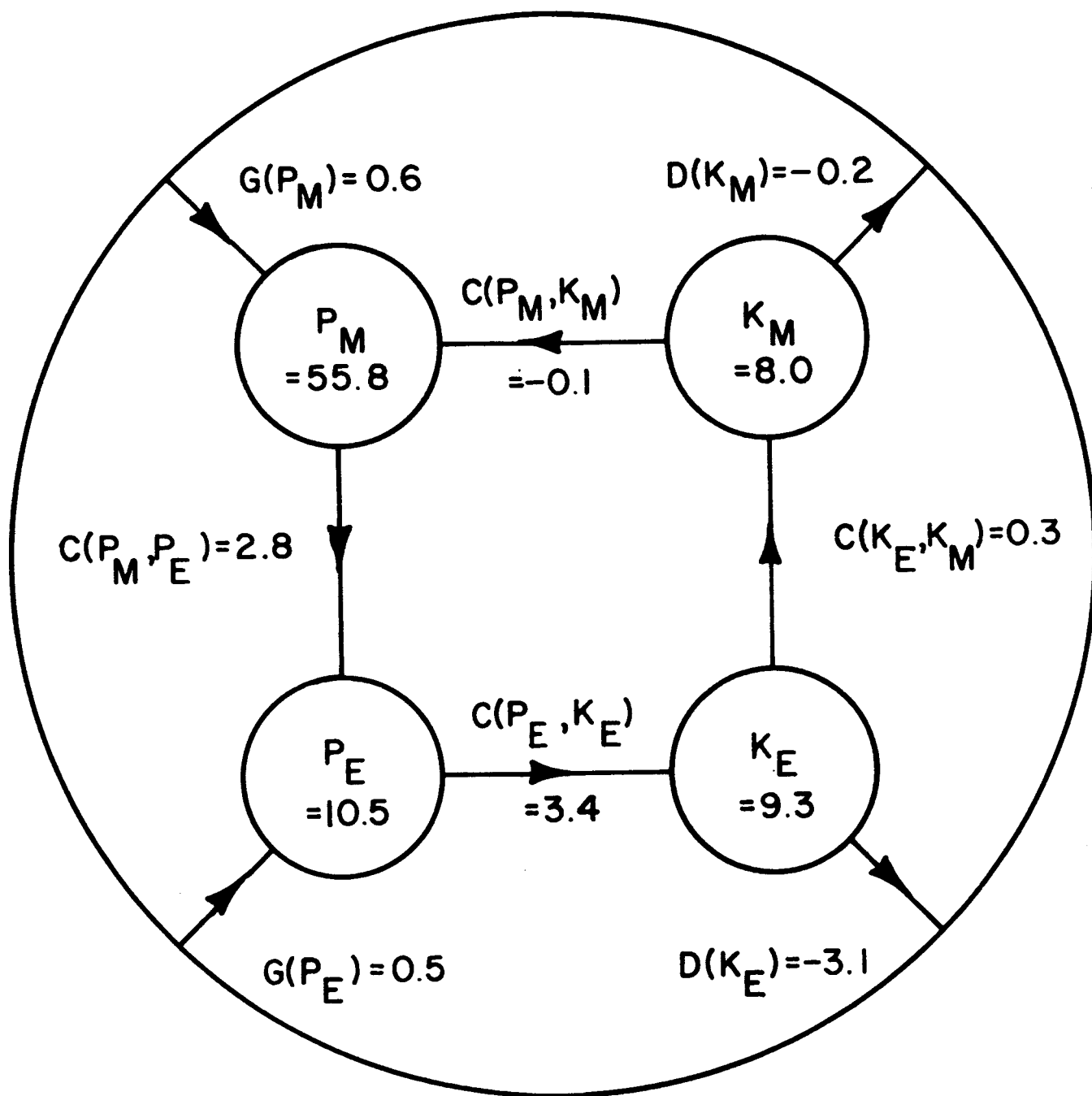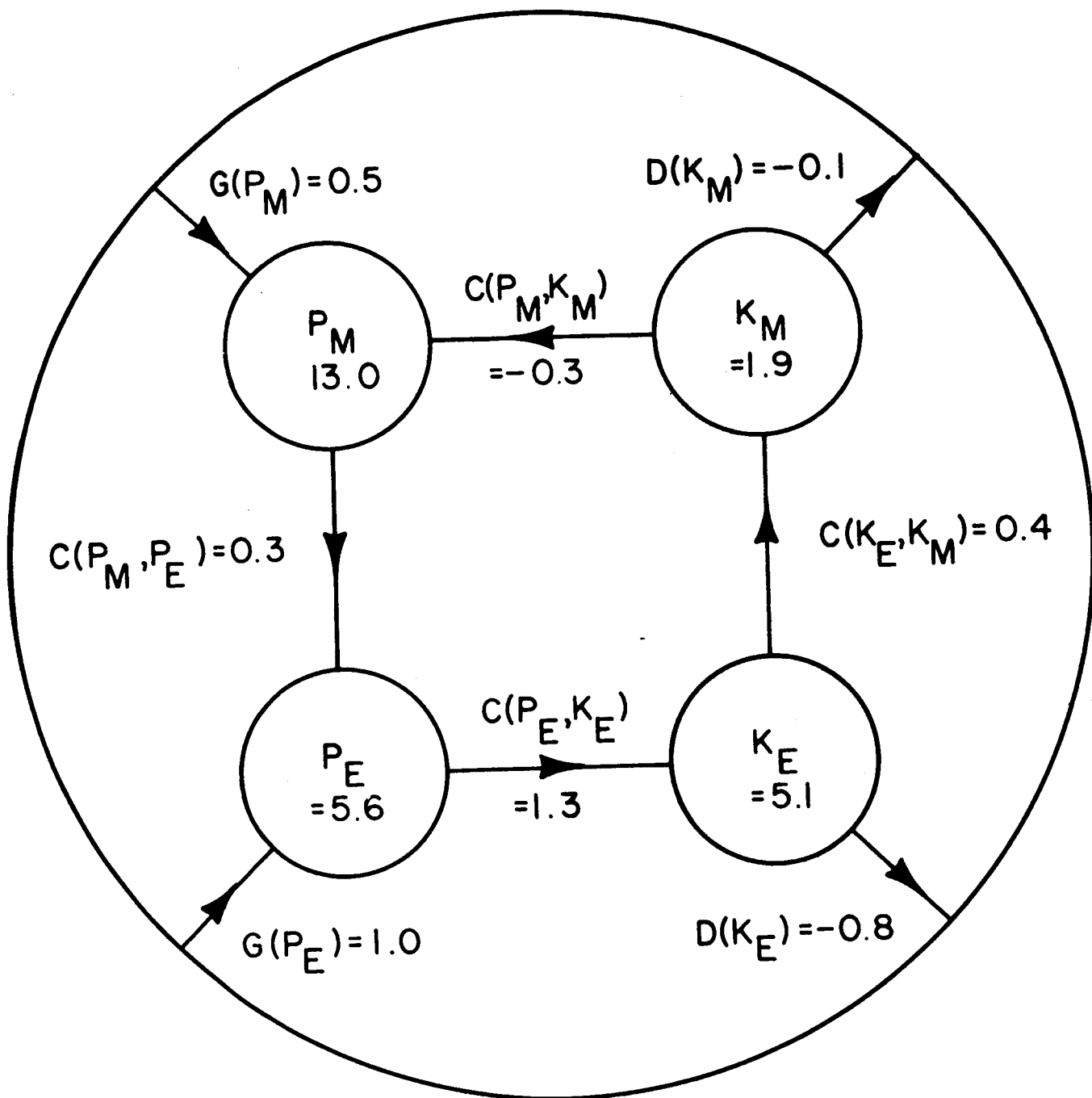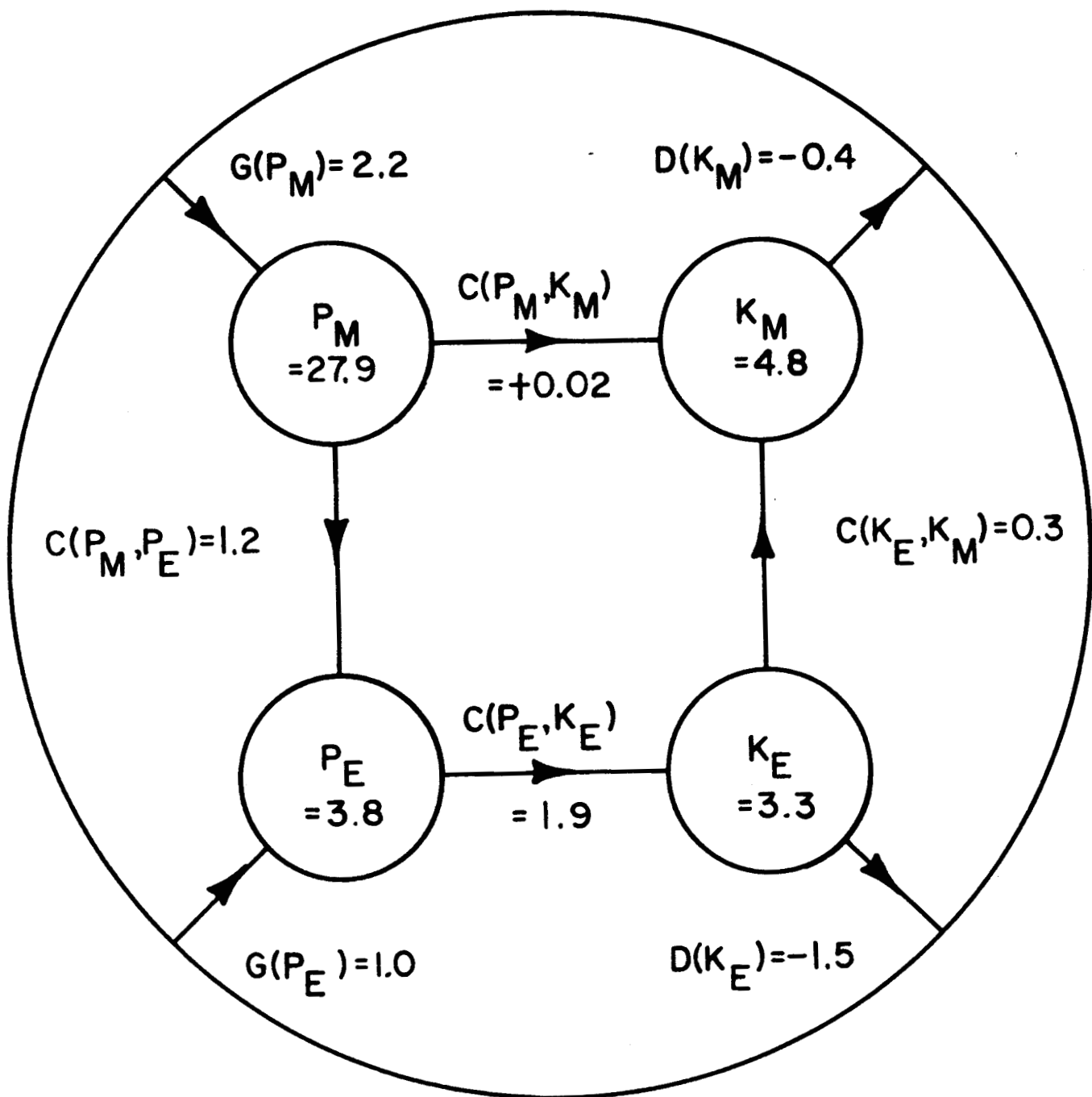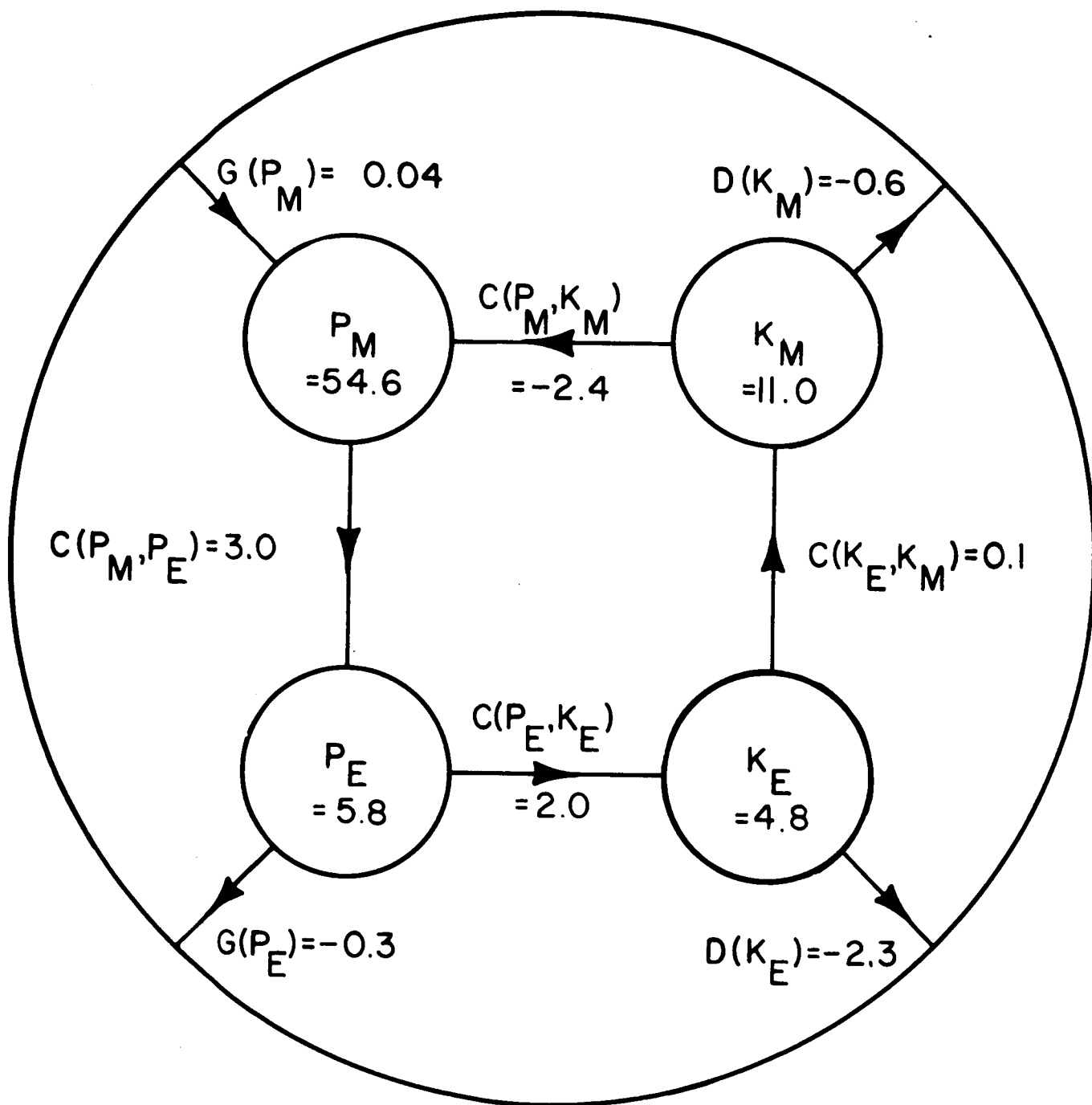
Fig. 4.3a
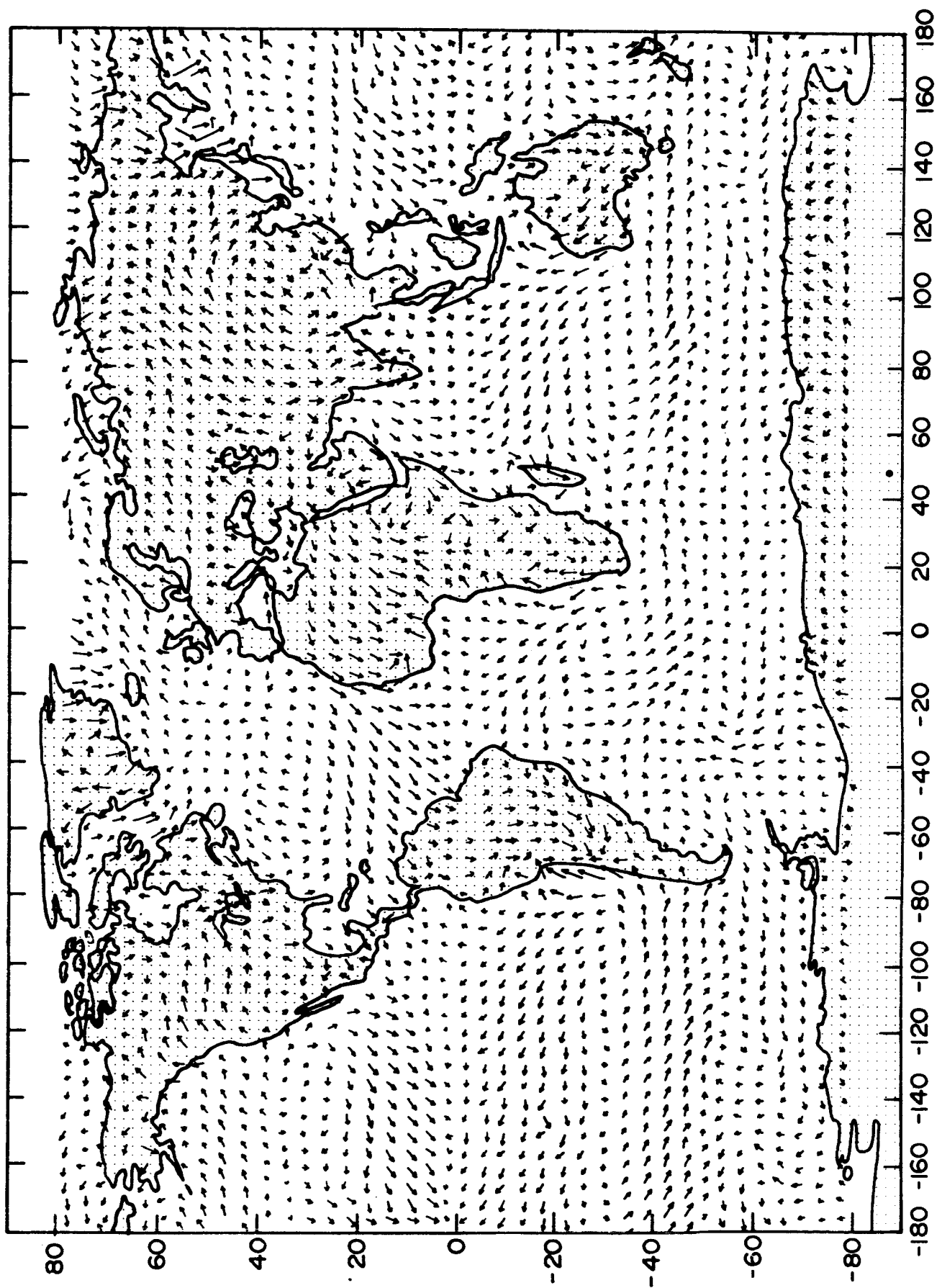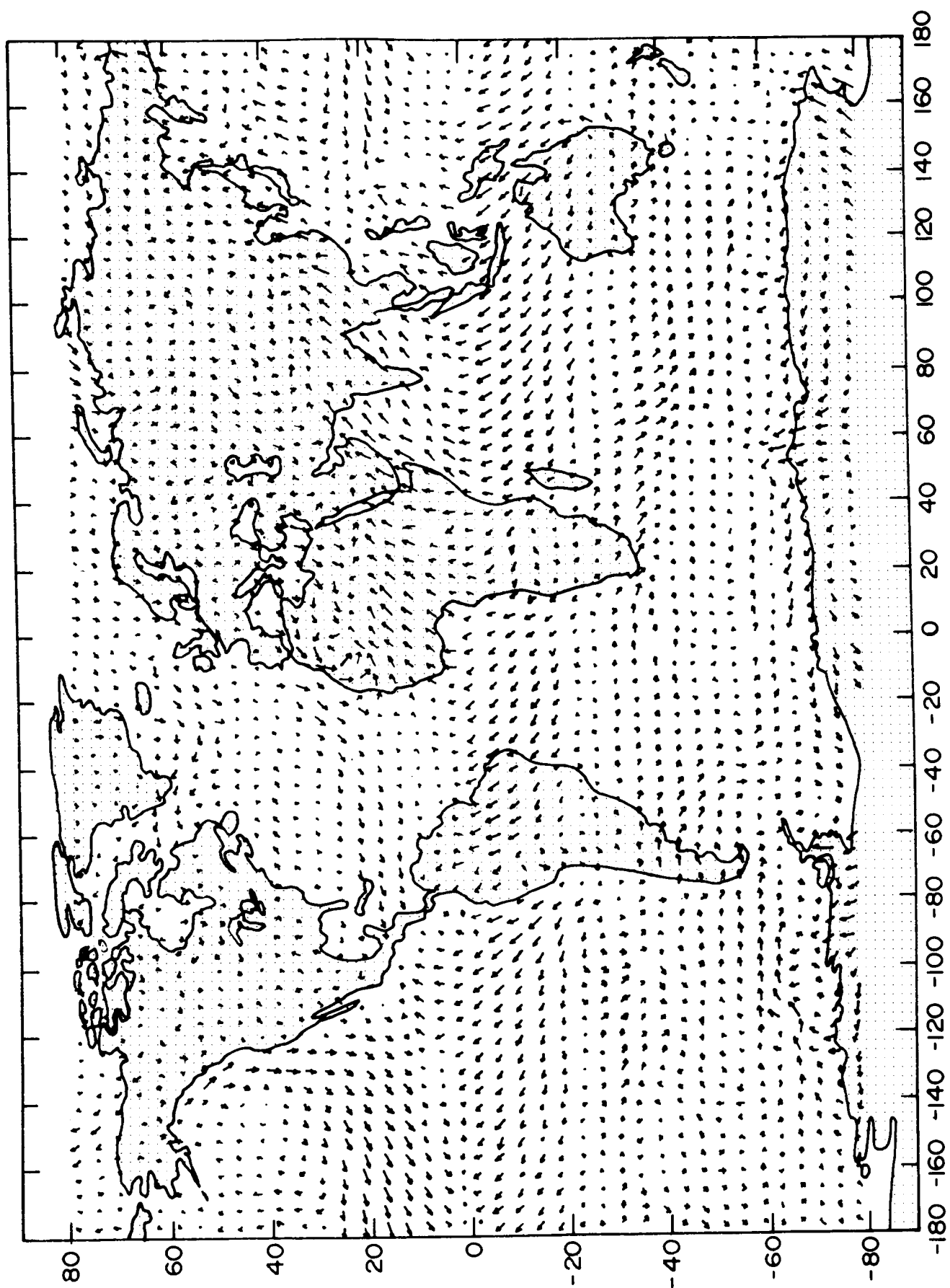
Fig.4.3b
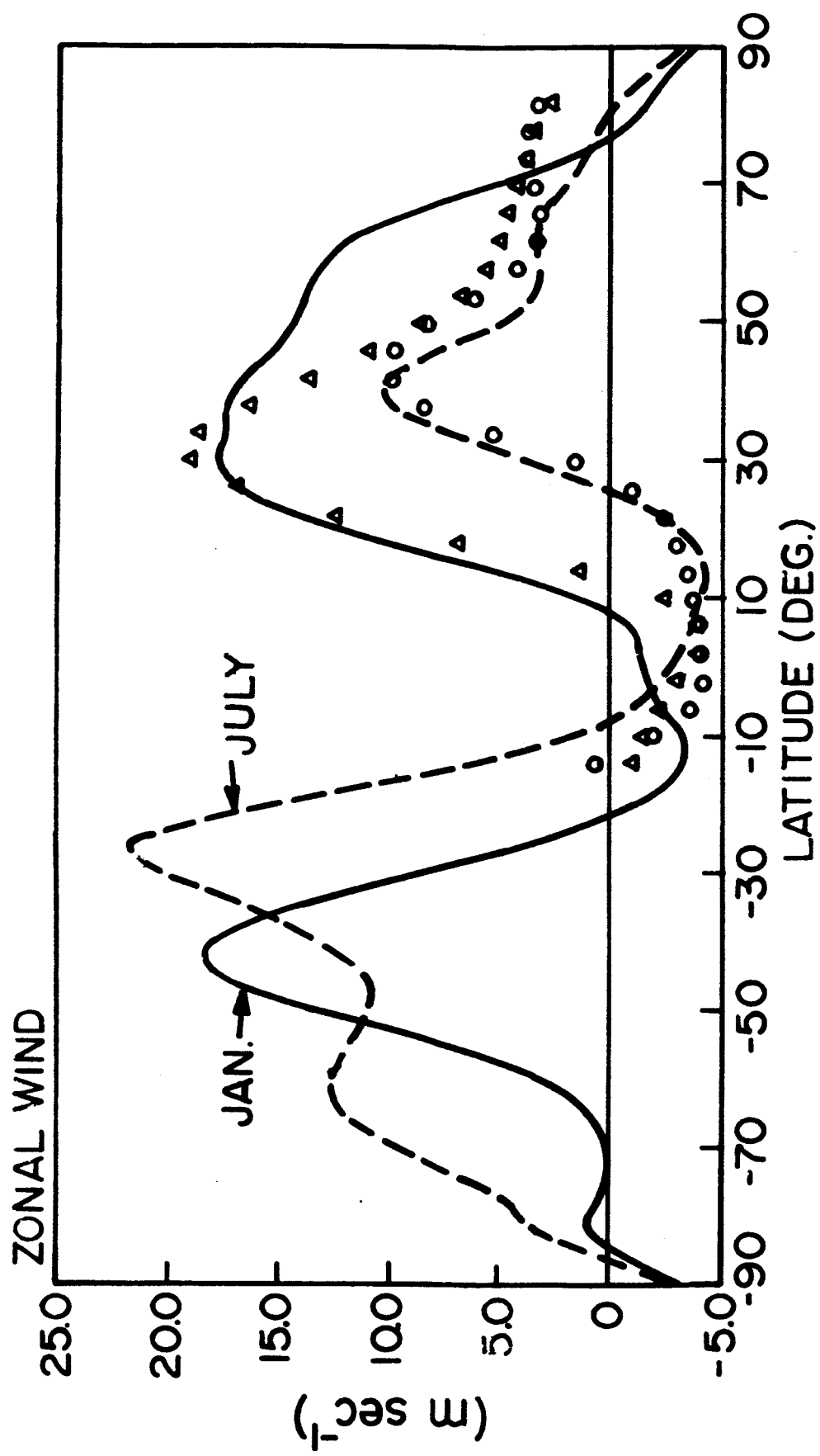
Fig. 4.4
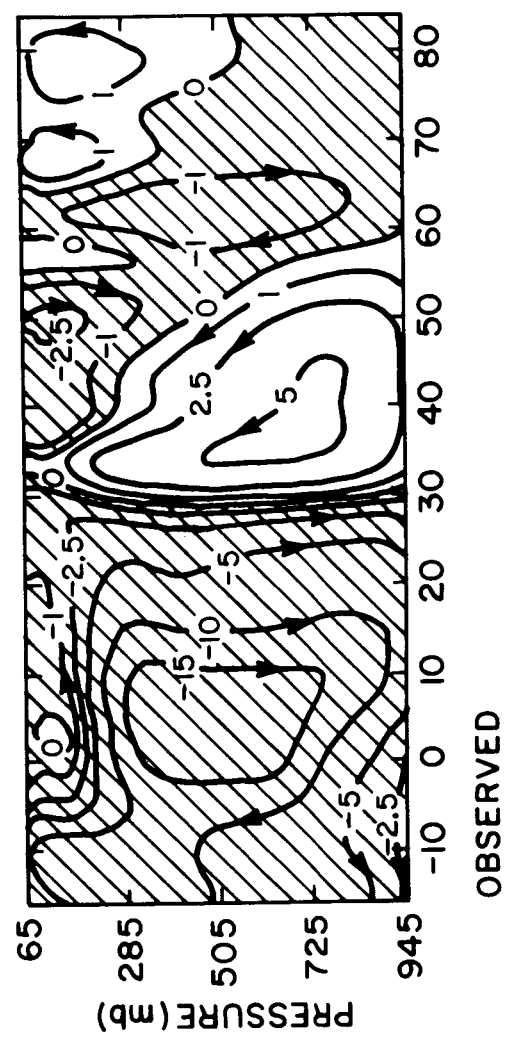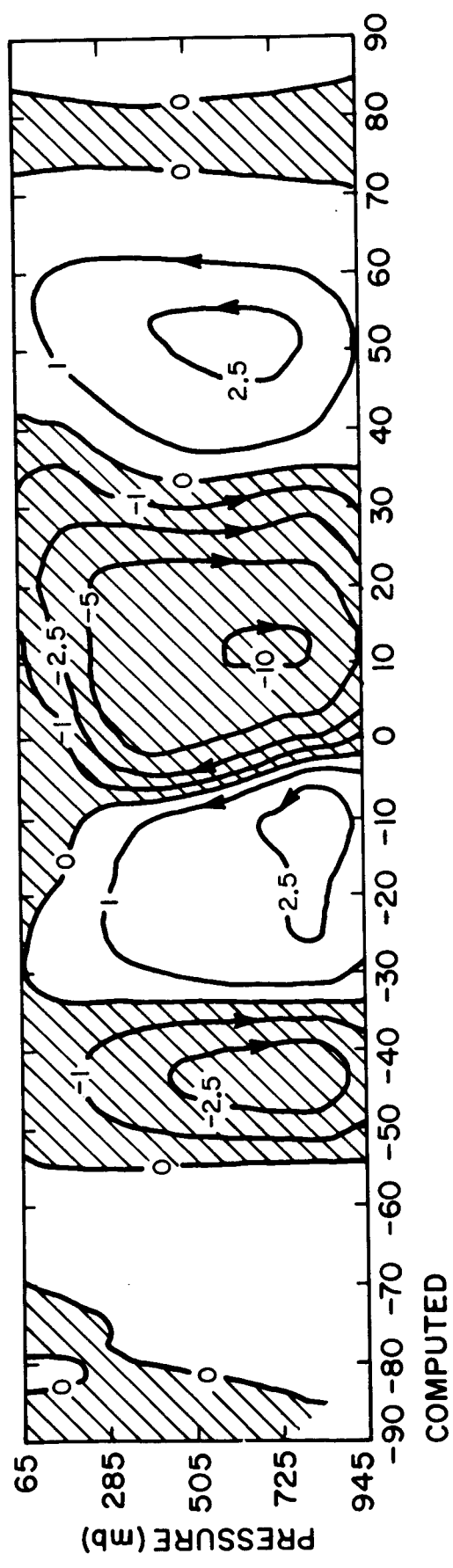
Fig. 4.5

Fig. 4.6

Fig. 4.7

Fig.4.8

PRECIPITATION
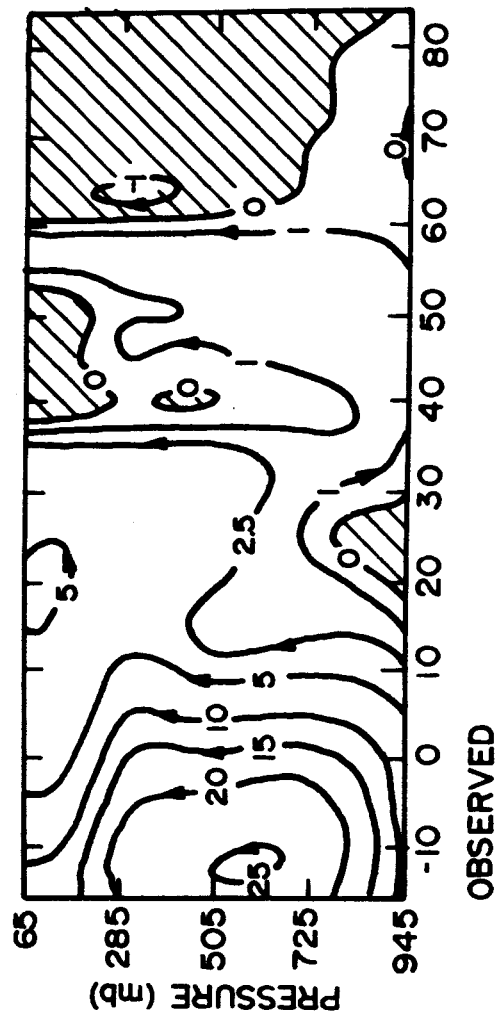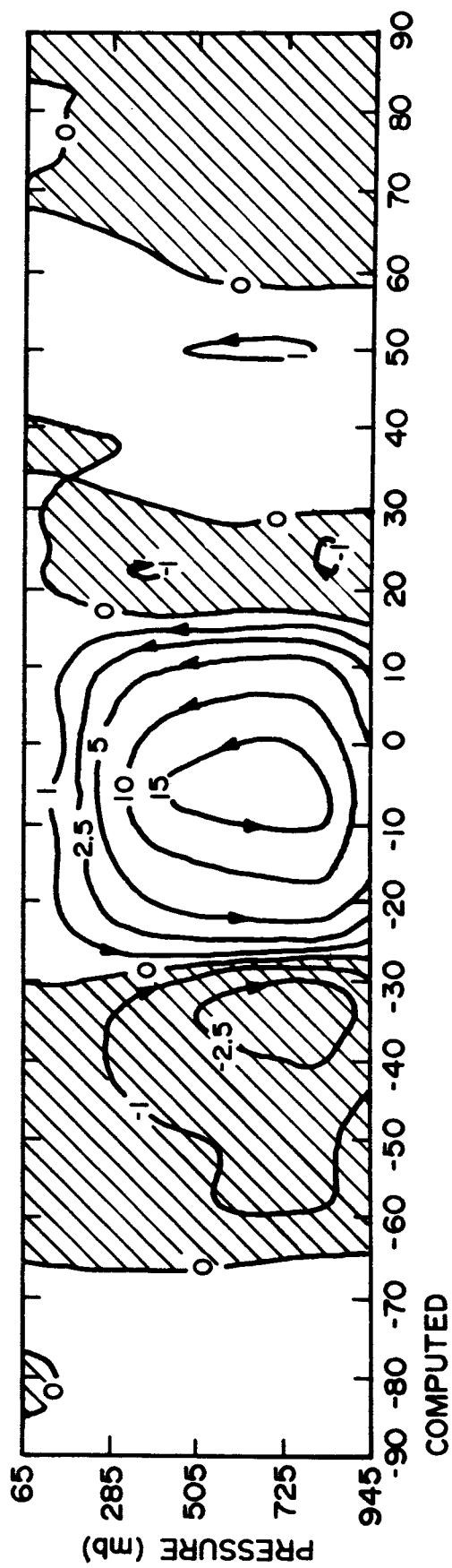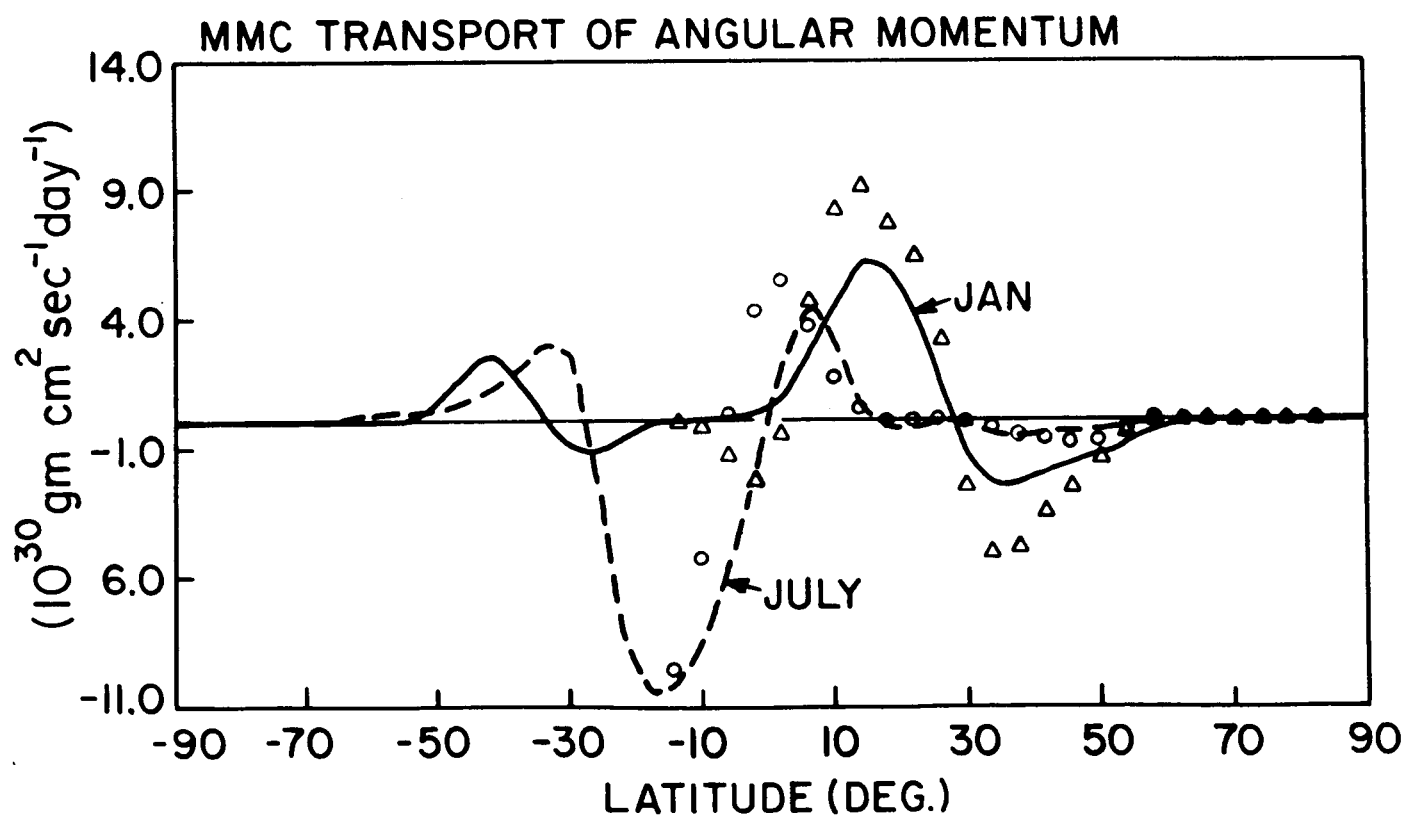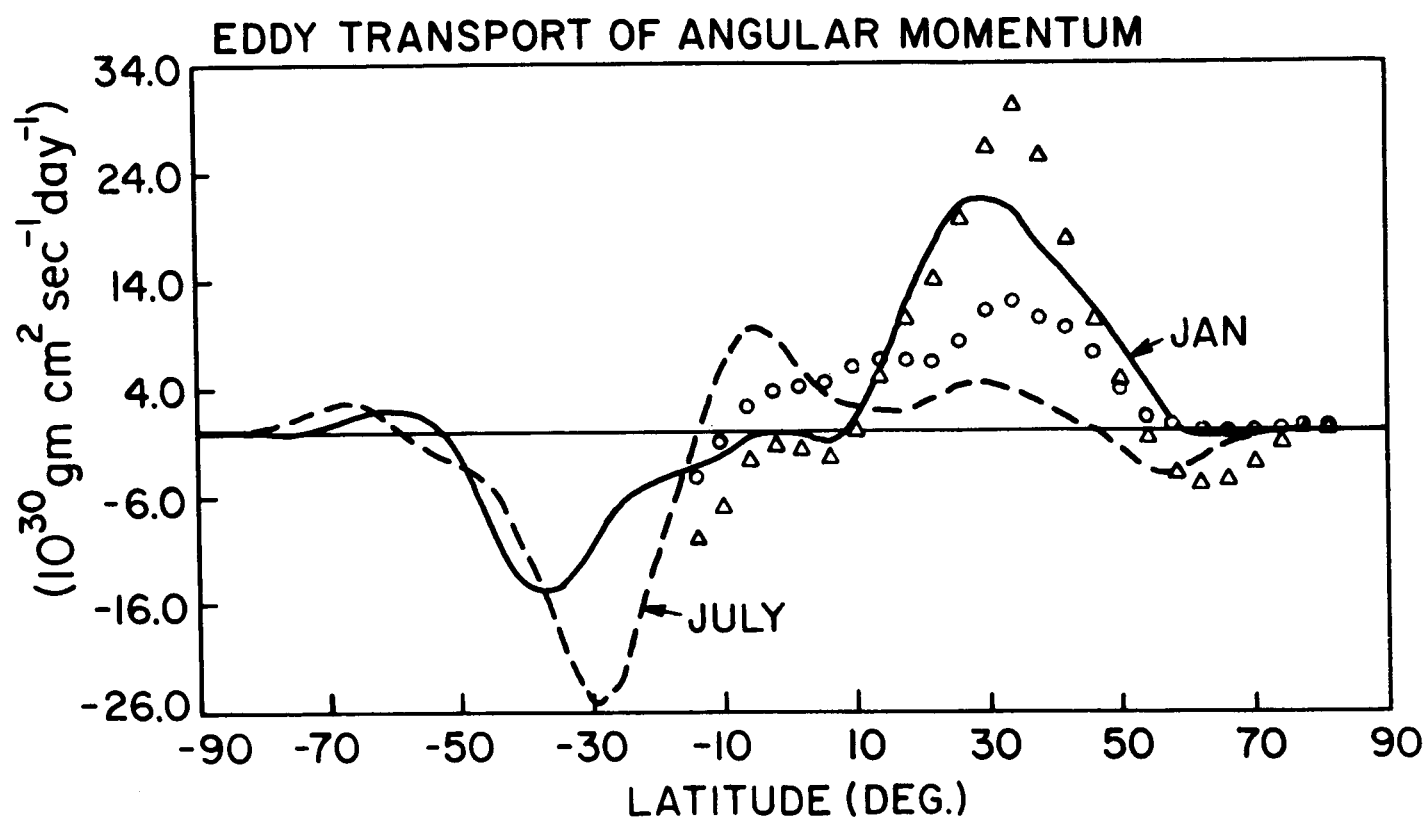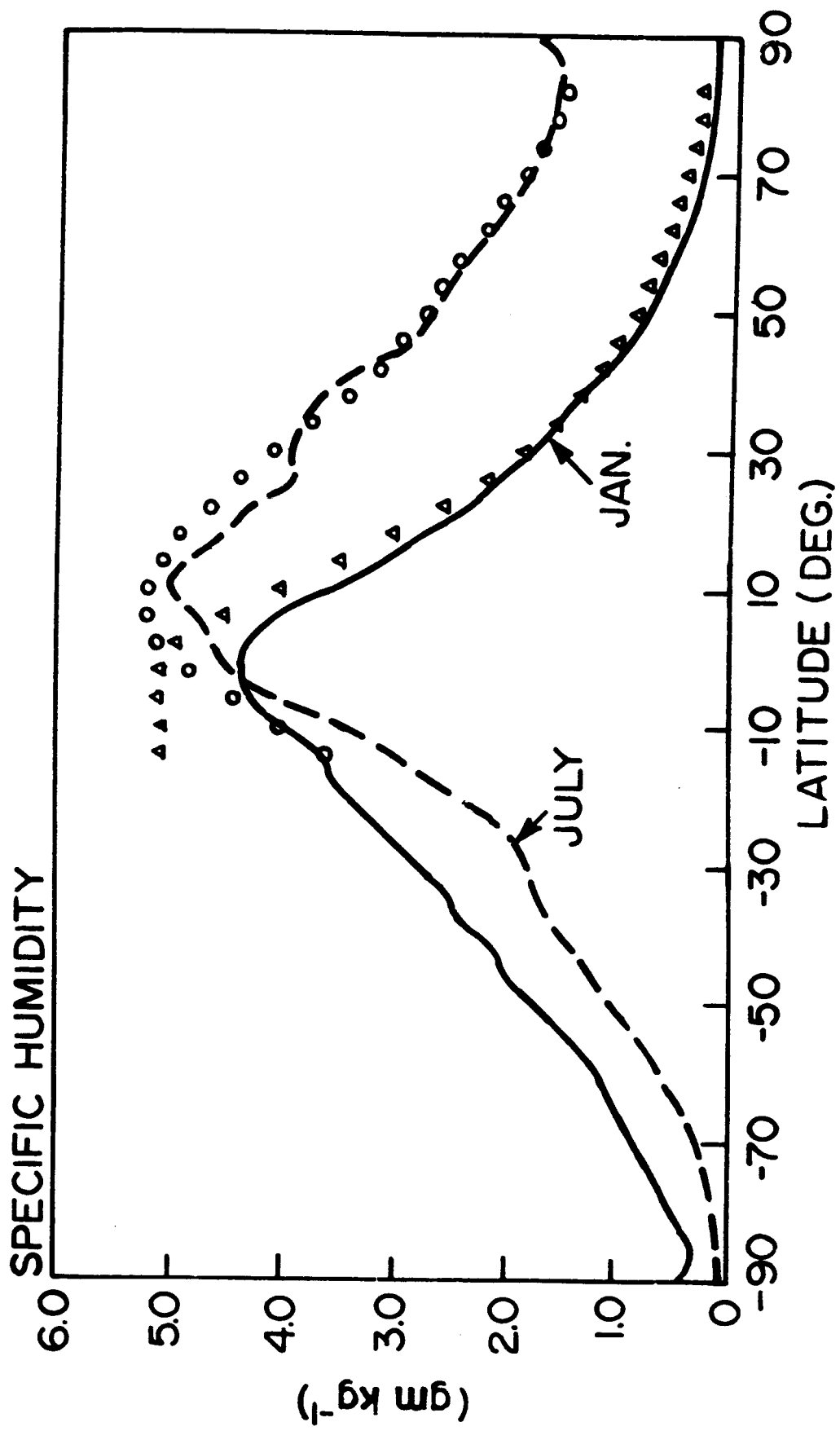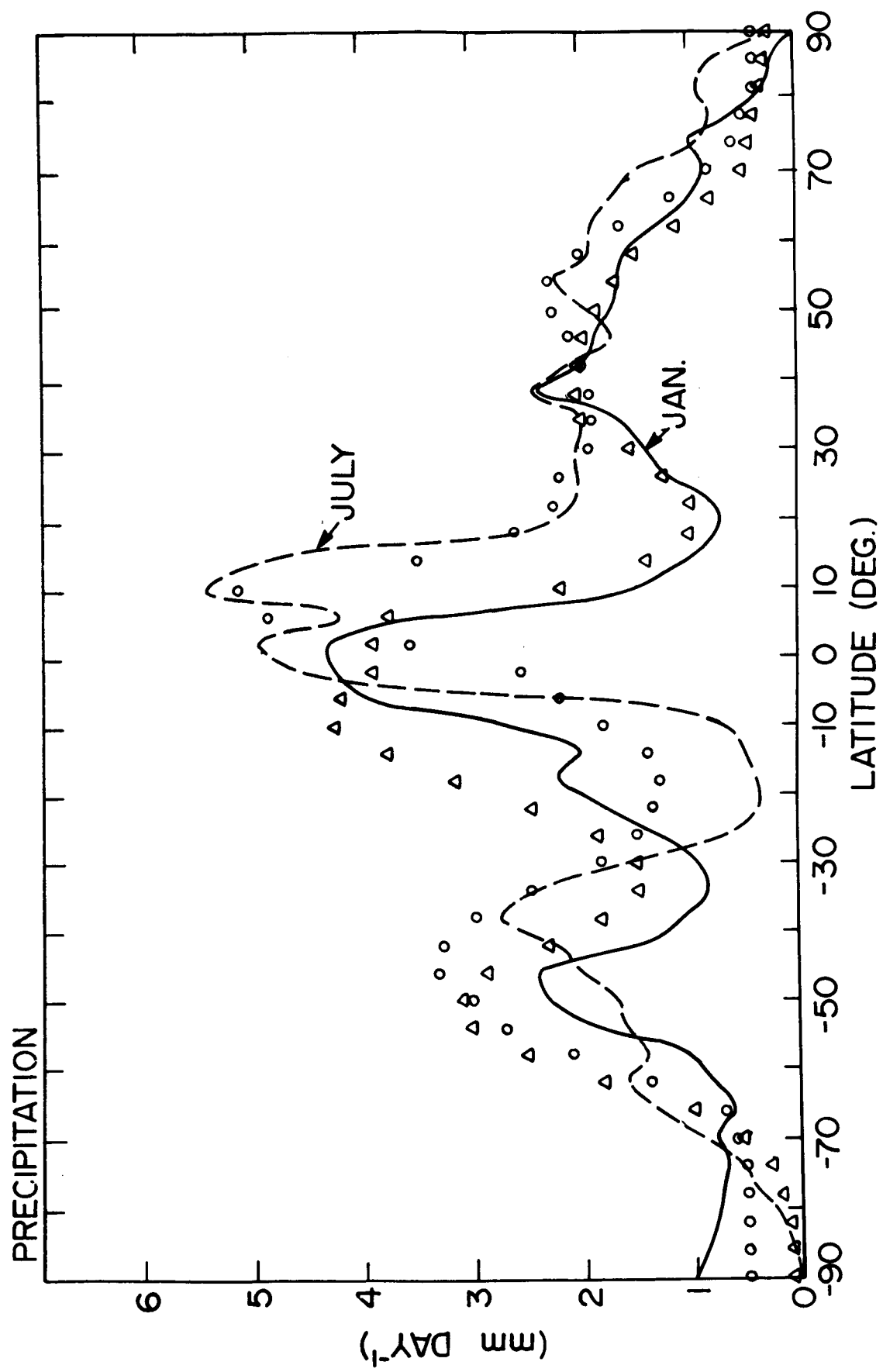
Fig. 4.9
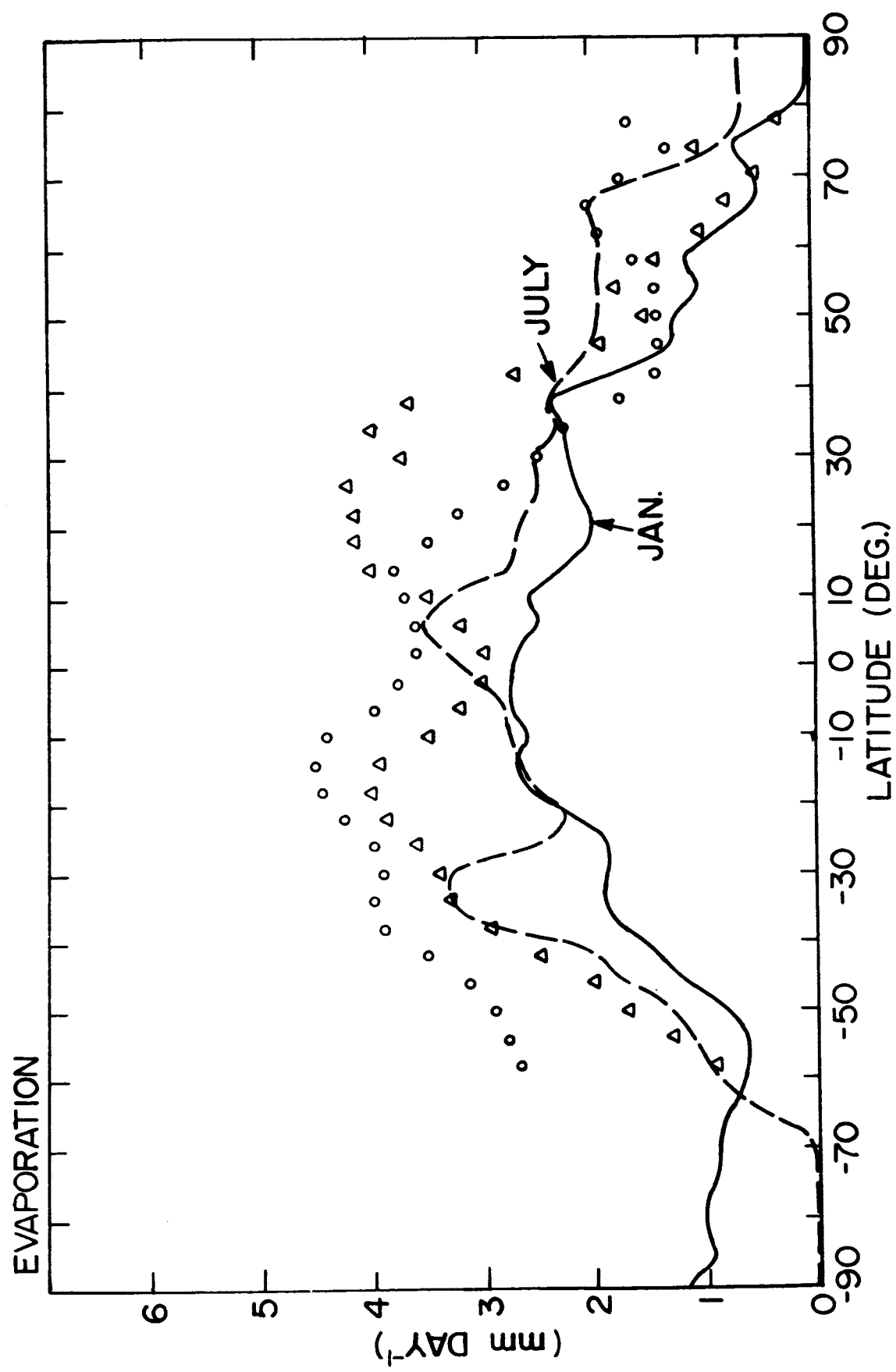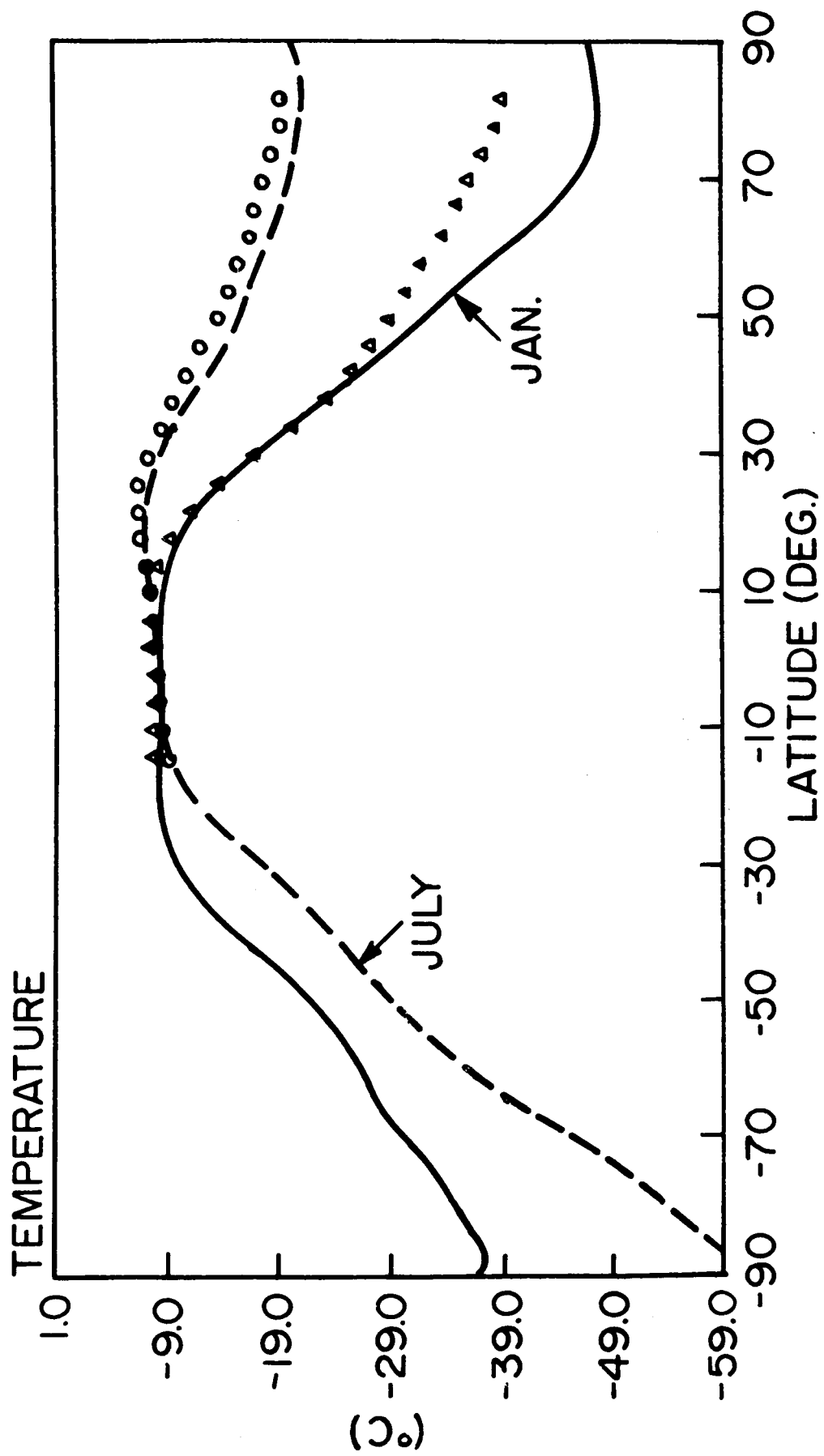
Fig. 4.10

Fig. 4.11
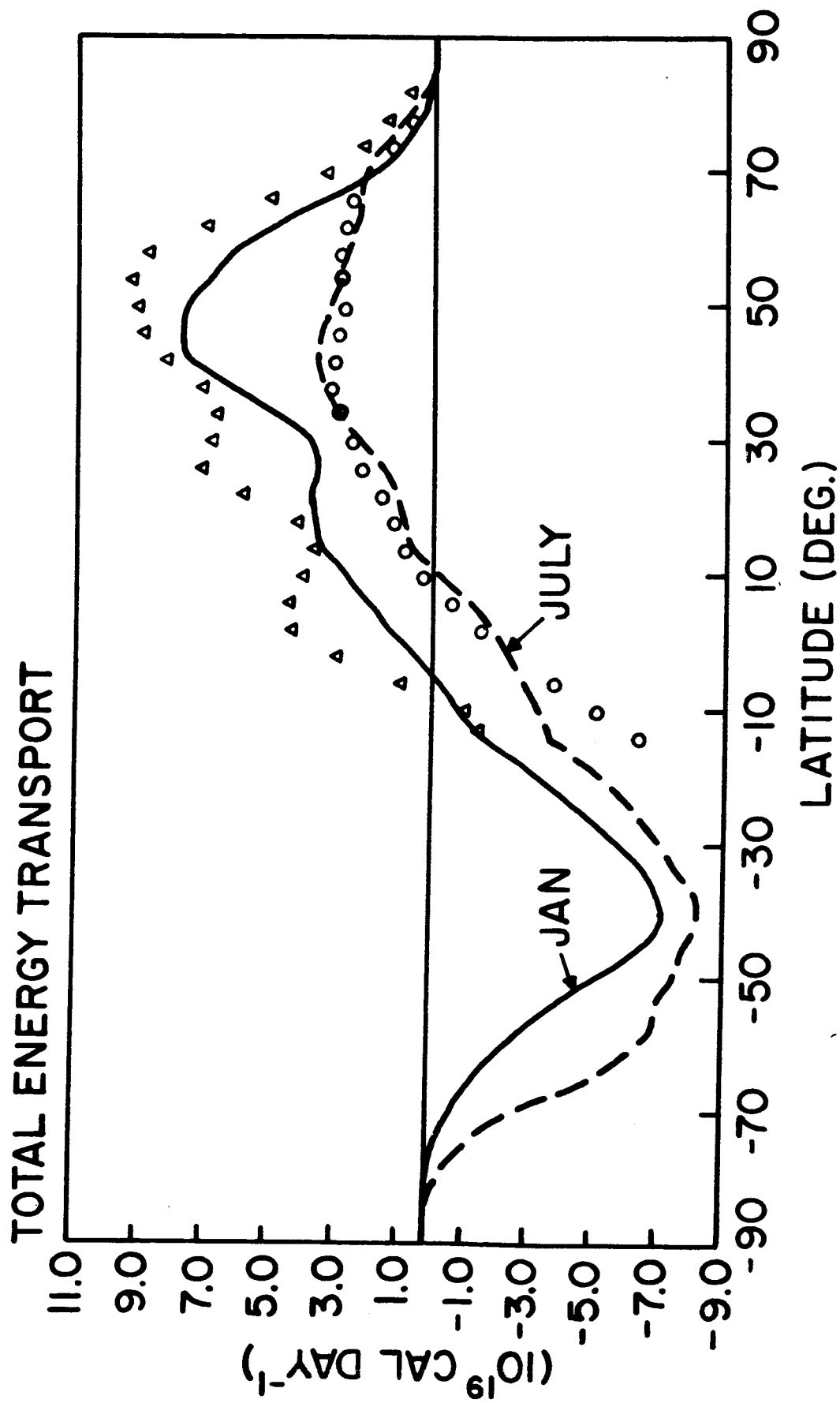
Fig. 4.12
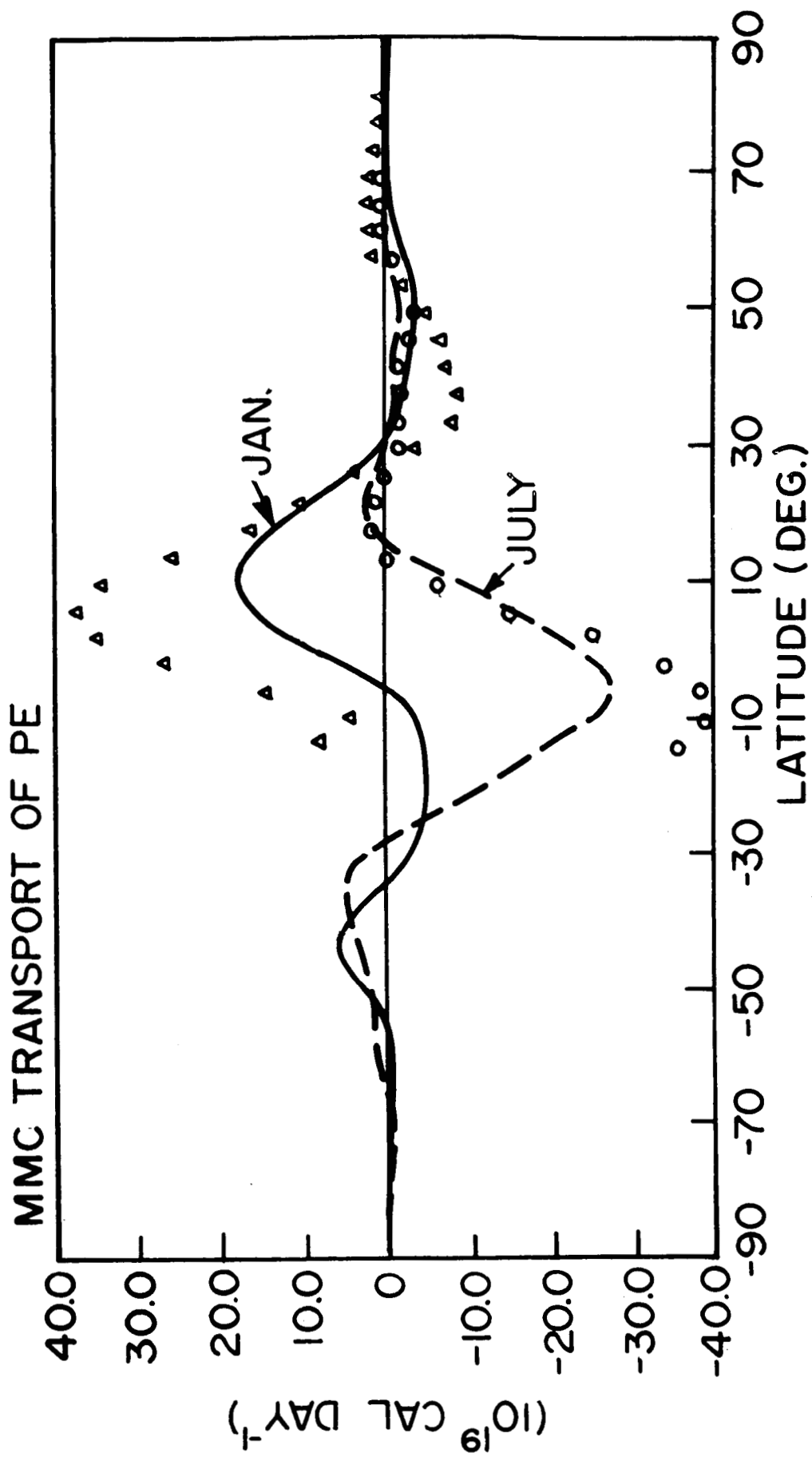
Fig. 4.13
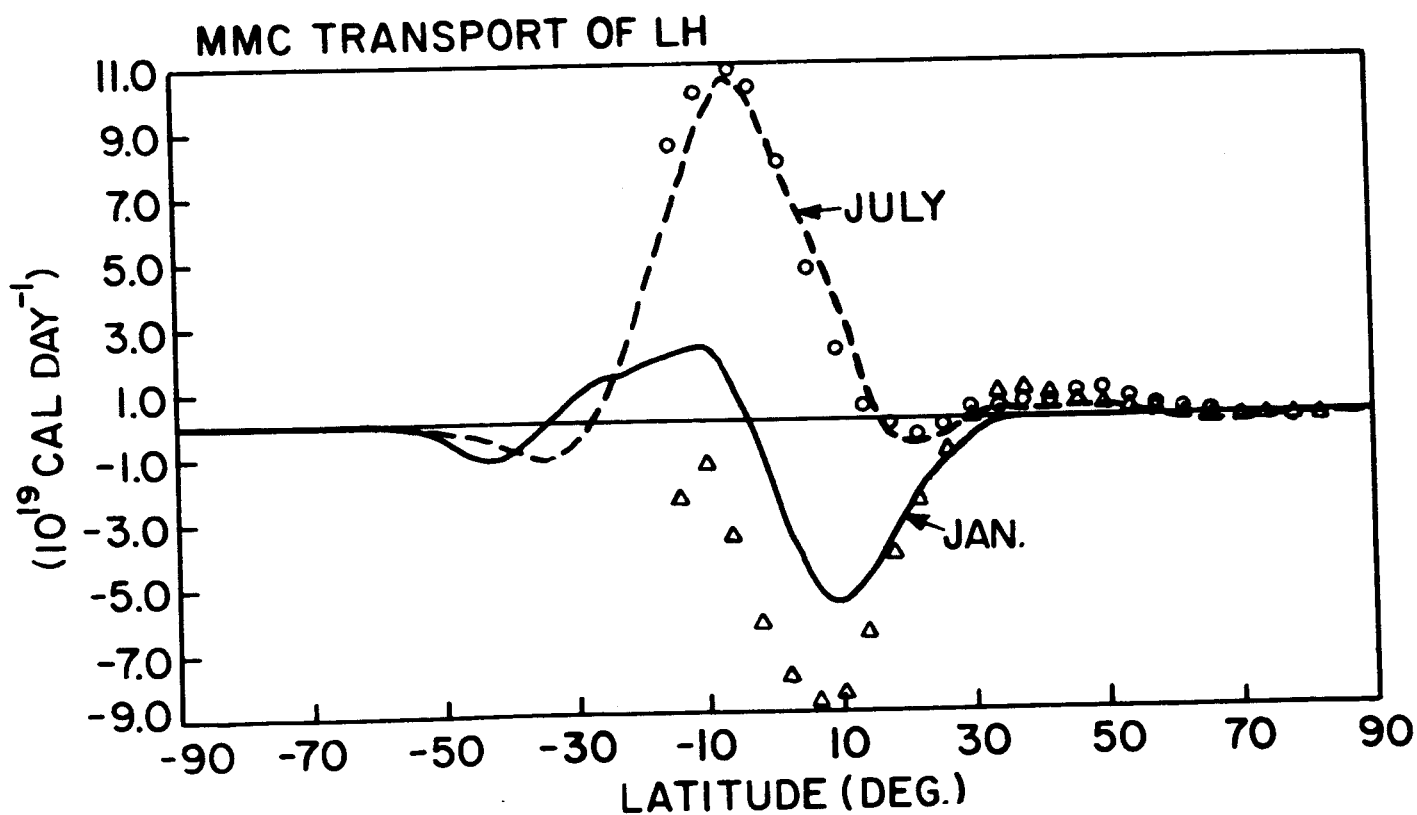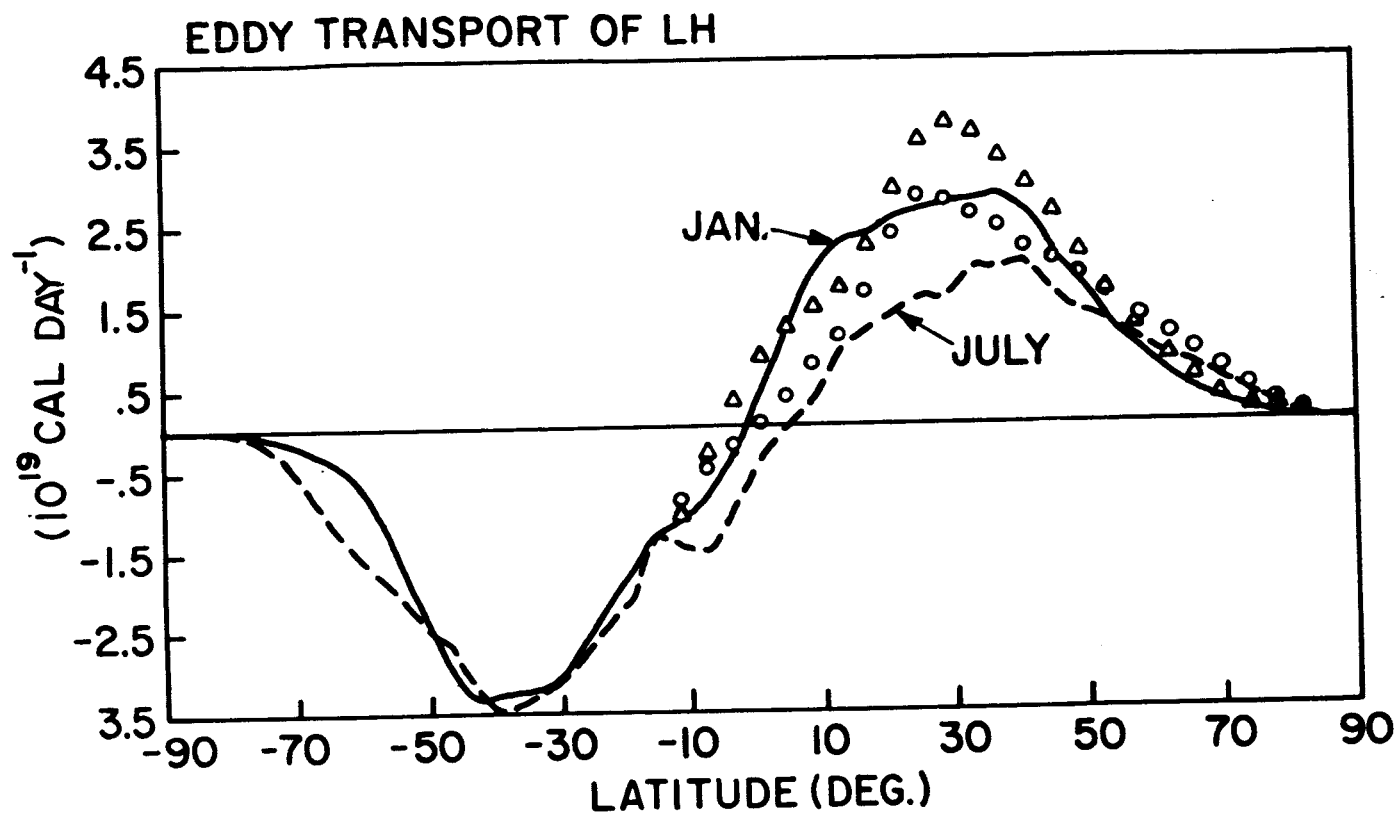
Fig. 4.14
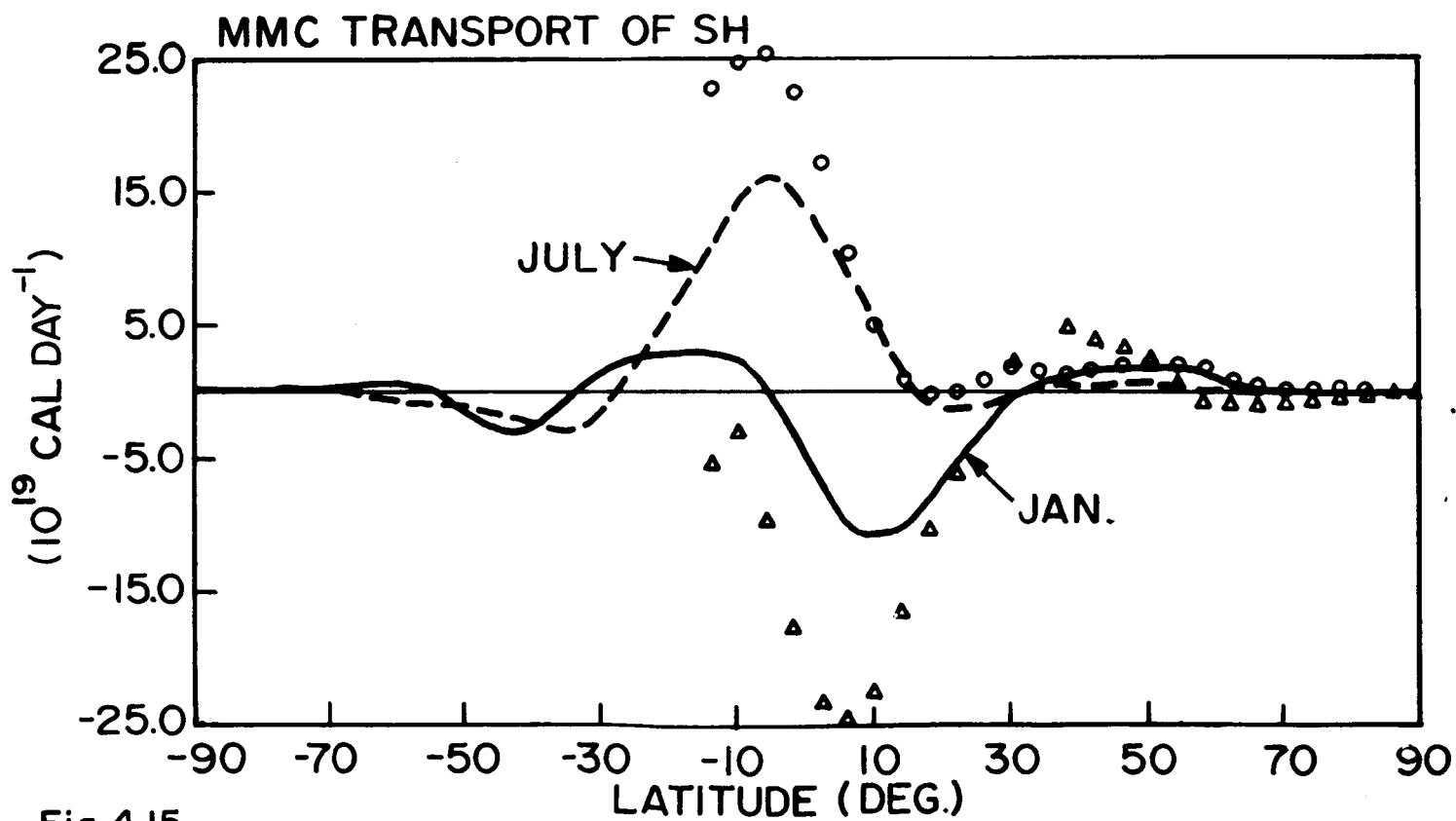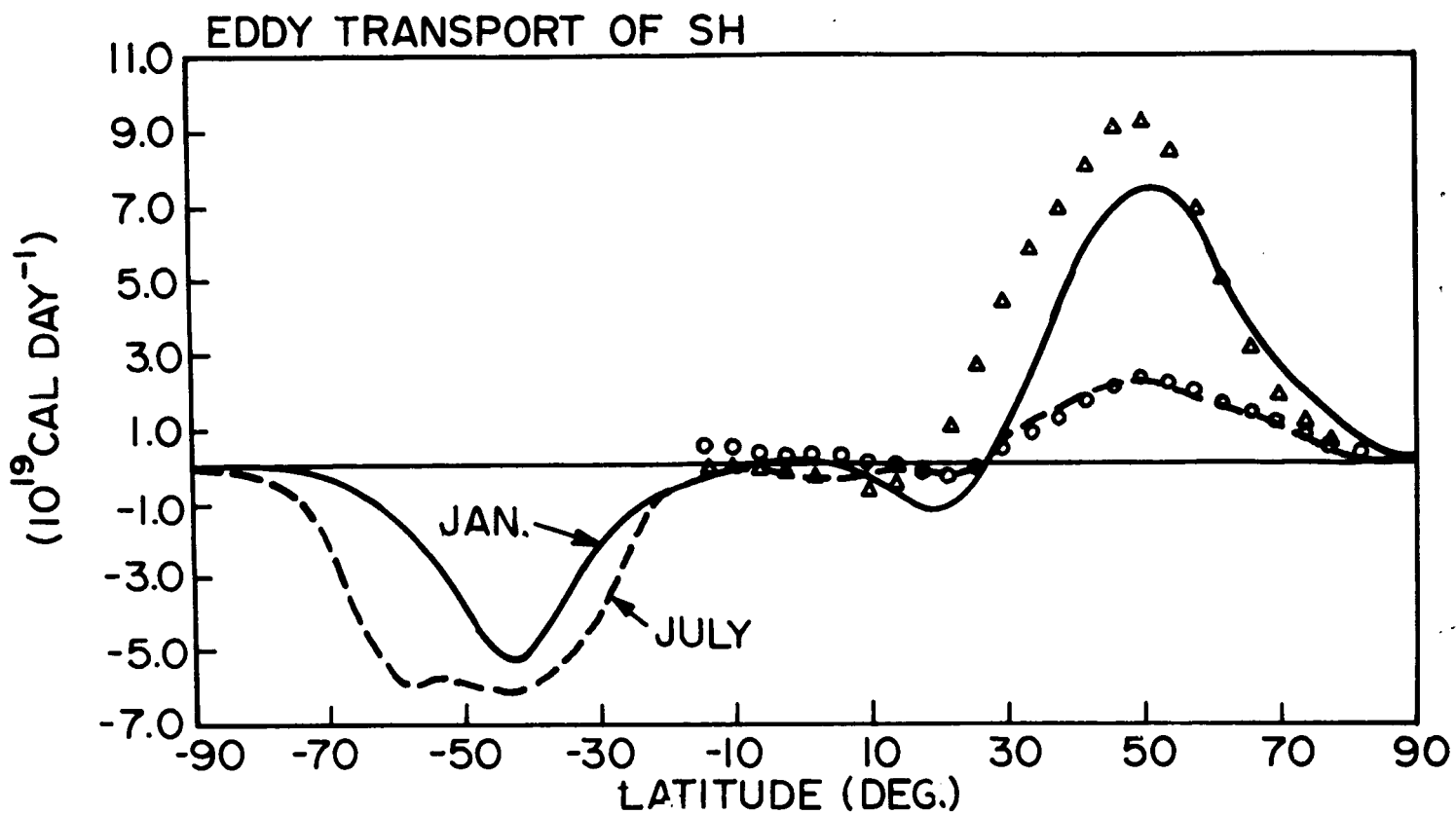
Fig. 4.15
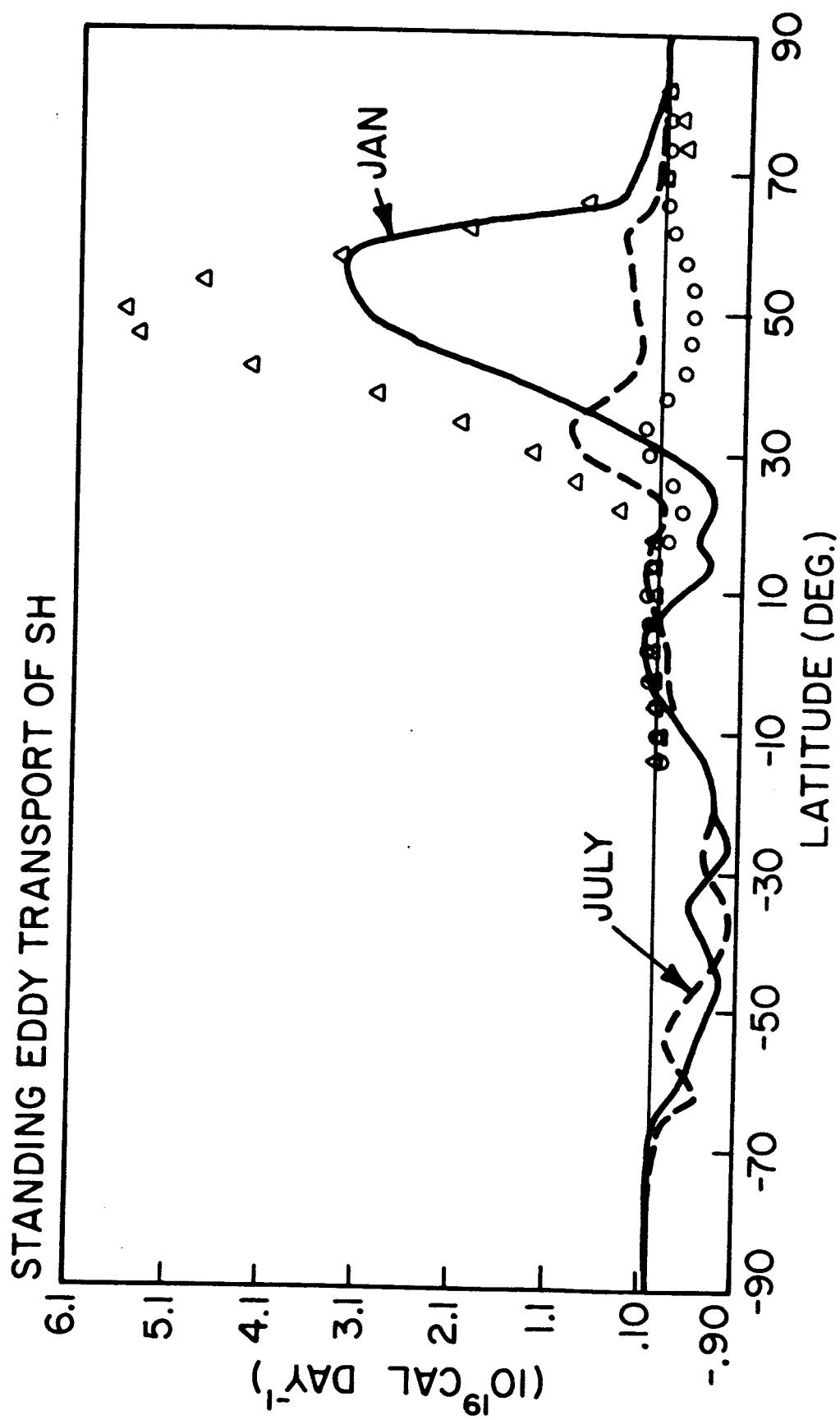
Fig. 4.16

TABLE 4.1

SIMULATED PERCENTAGE CLOUD COVERS

CLOUD TYPE	NORTHERN HEMISPHERE		SOUTHERN HEMISPHERE	
	JANUARY	JULY	JANUARY	JULY
LOW LEVEL CONVECTIVE CLOUDS	7	8	6	9
MIDDLE LEVEL CONVECTIVE CLOUDS	2	3	3	3
PENETRATING CONVECTIVE CLOUDS	5	12	7	4
ALL CONVECTIVE CLOUDS	12	21	14	13
SUPERSATURATION CLOUDS	45	44	40	47
ALL CLOUDS	49	52	45	50
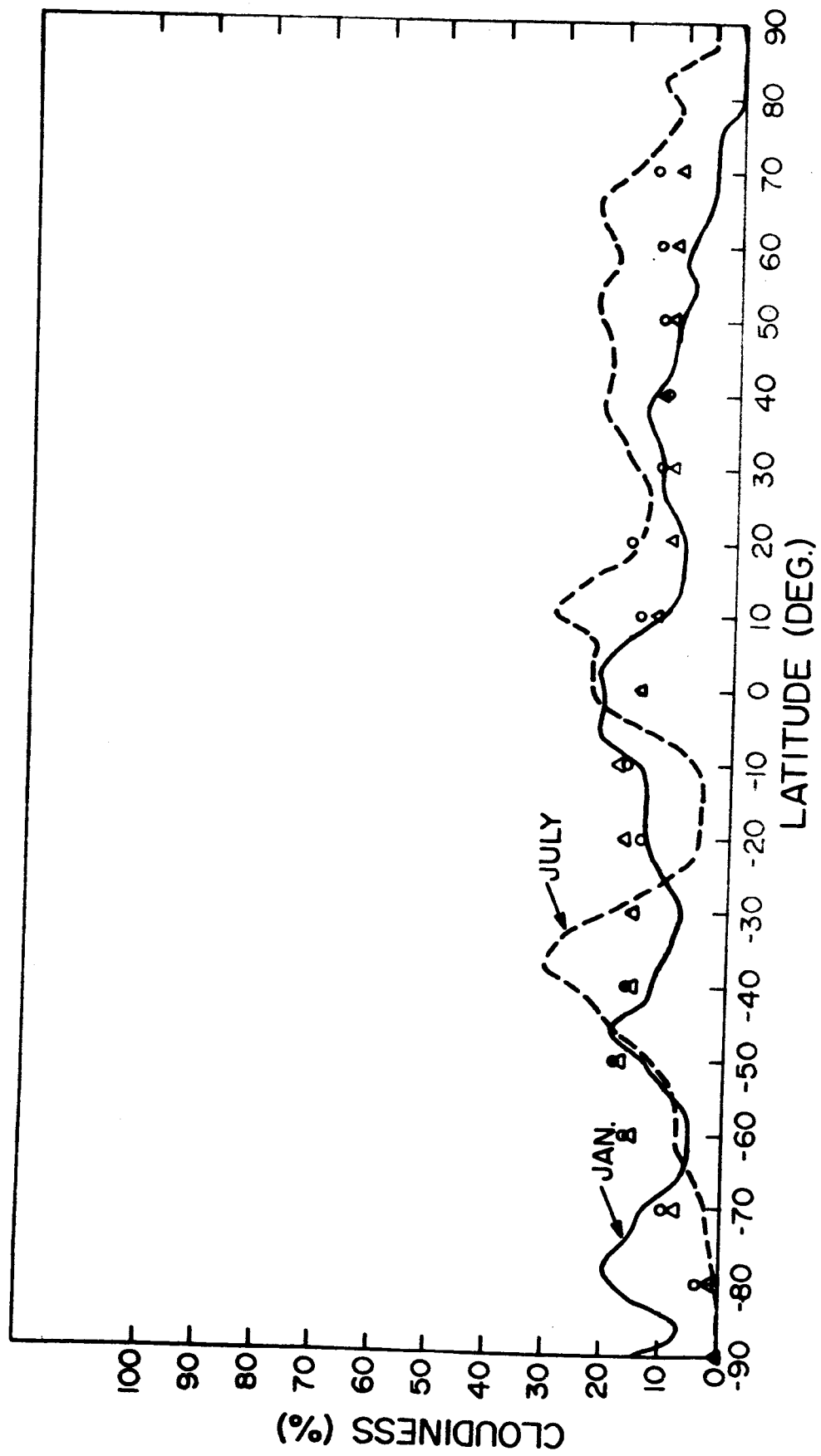
Fig. 4.17
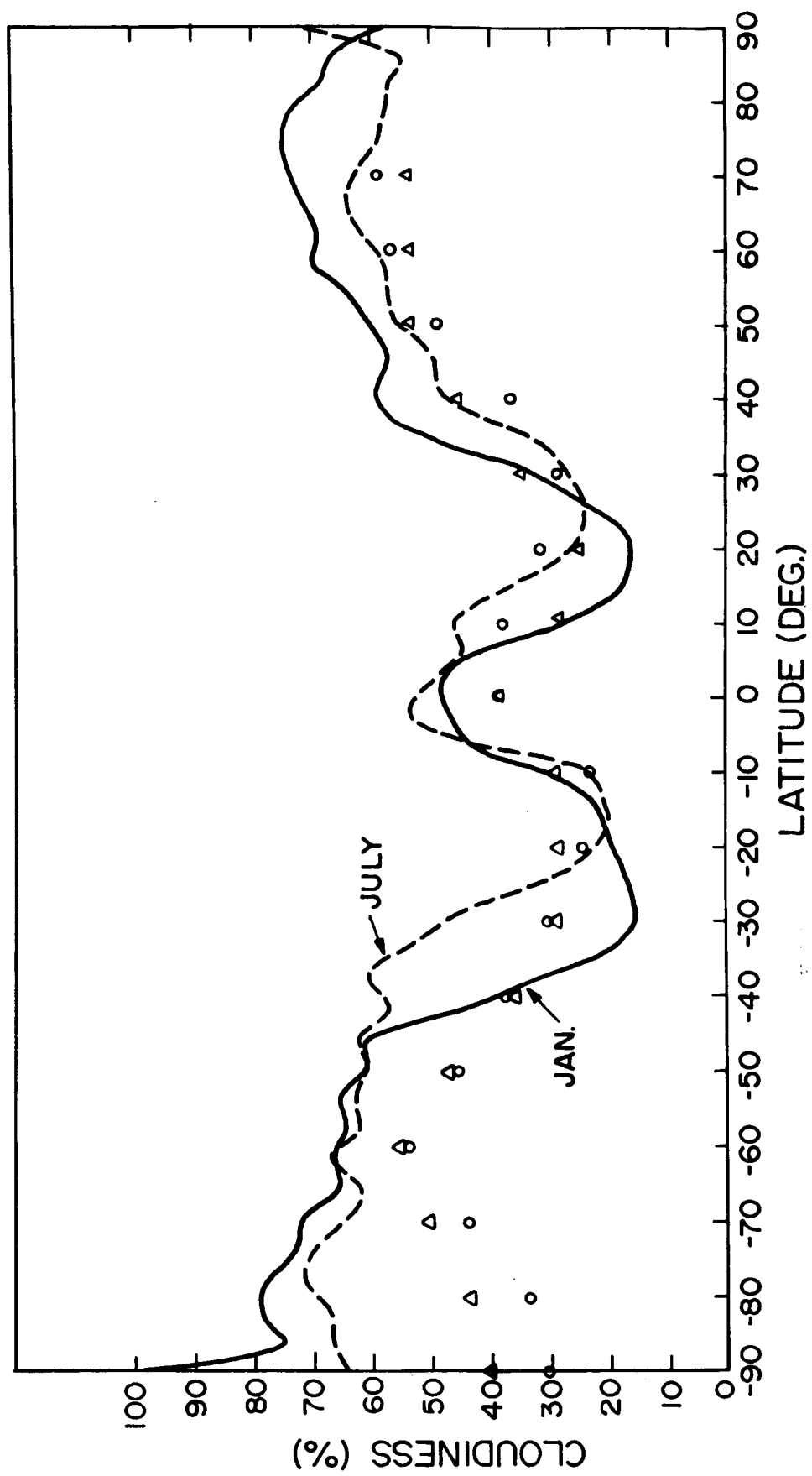
Fig. 4.18
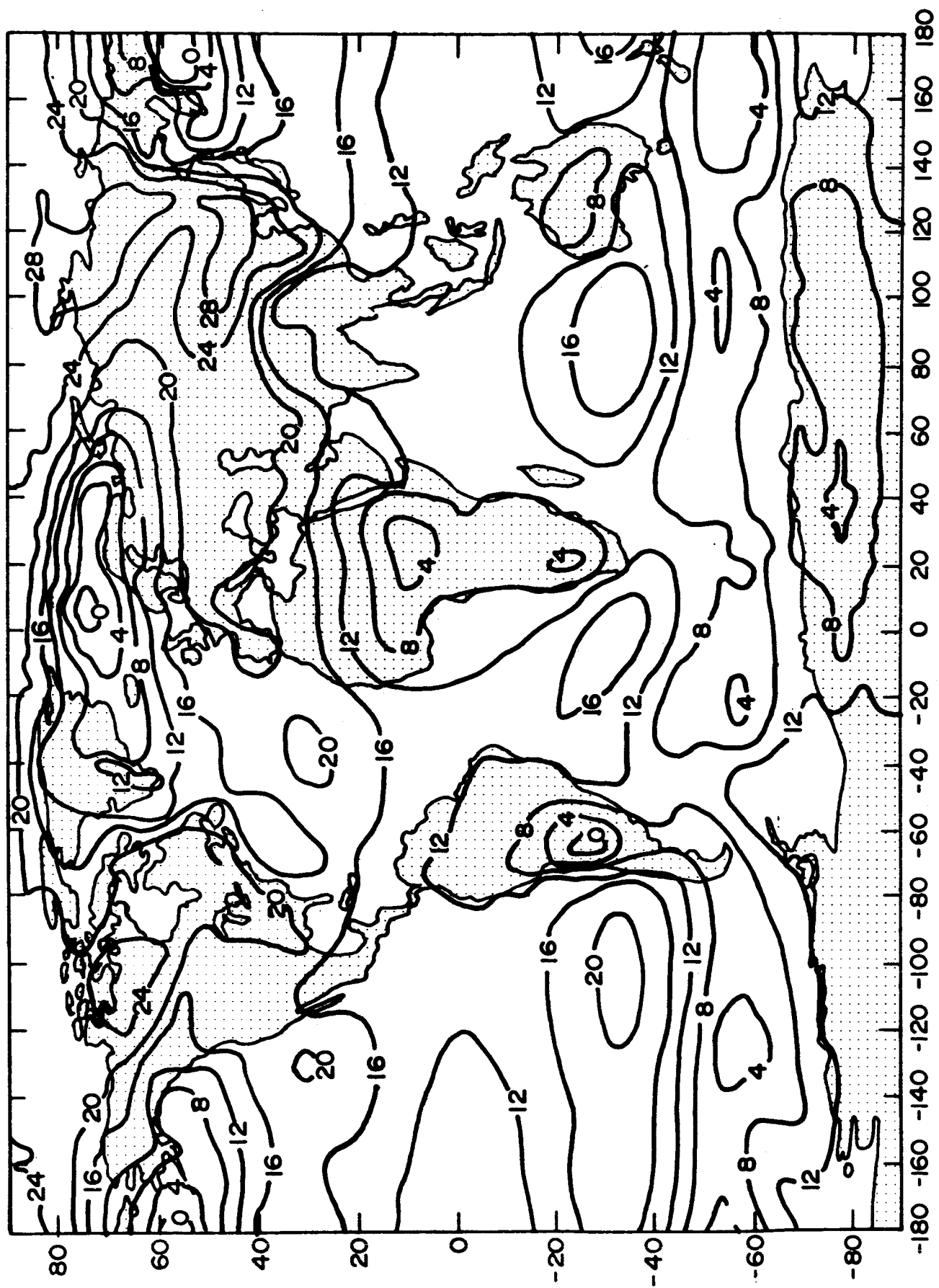
Fig. 4.19
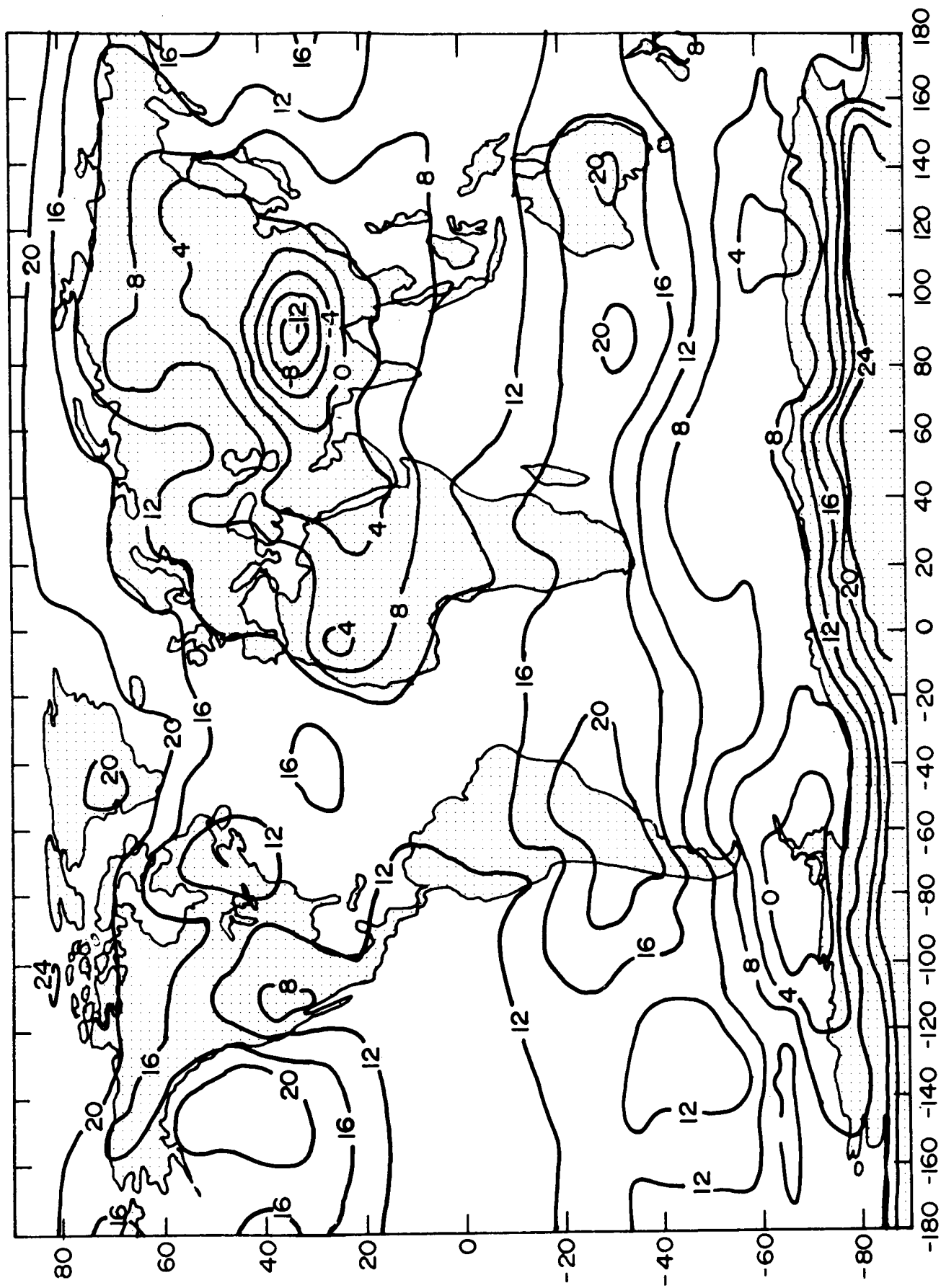
Fig. 4.20
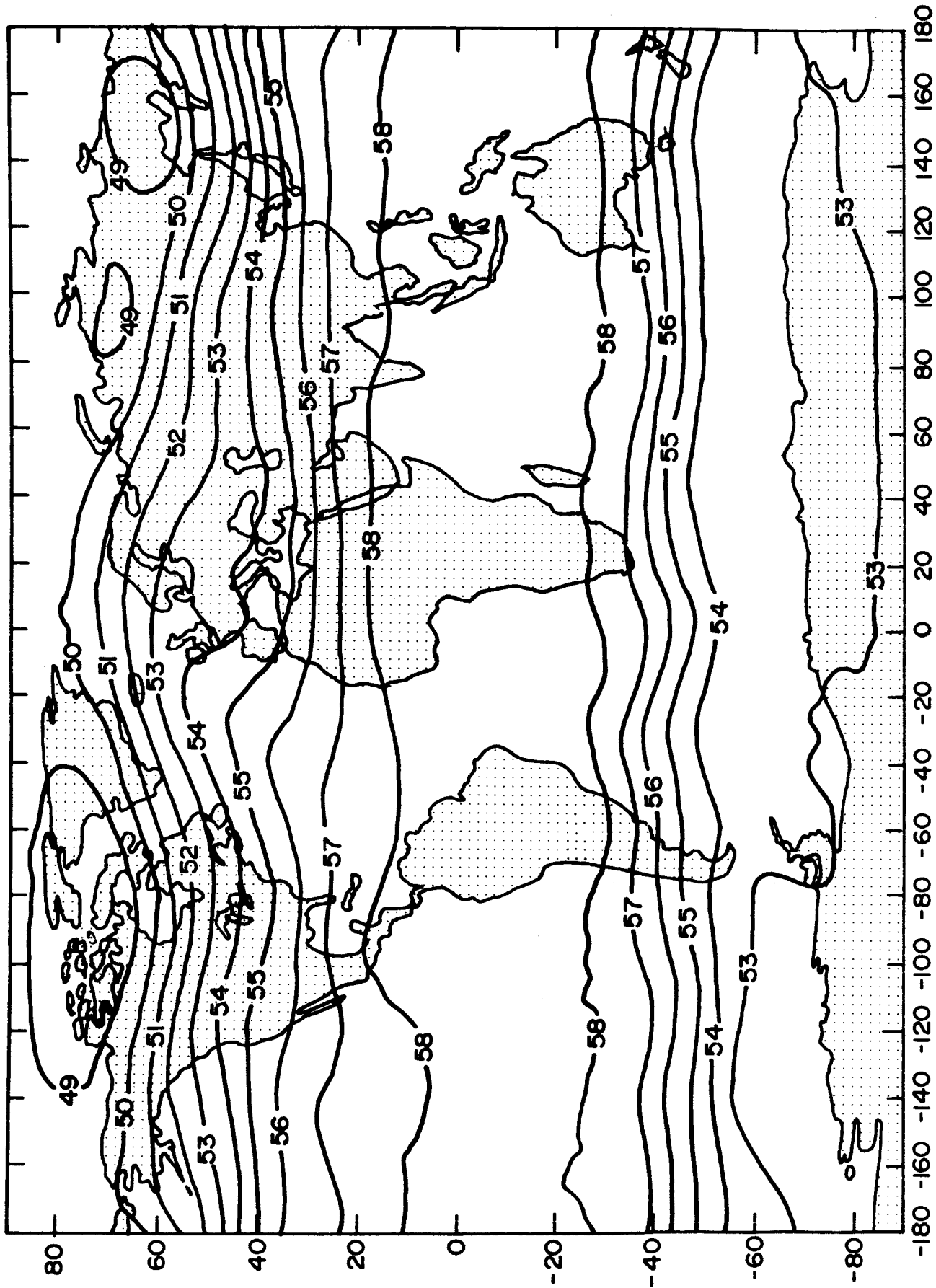
Fig.4.21
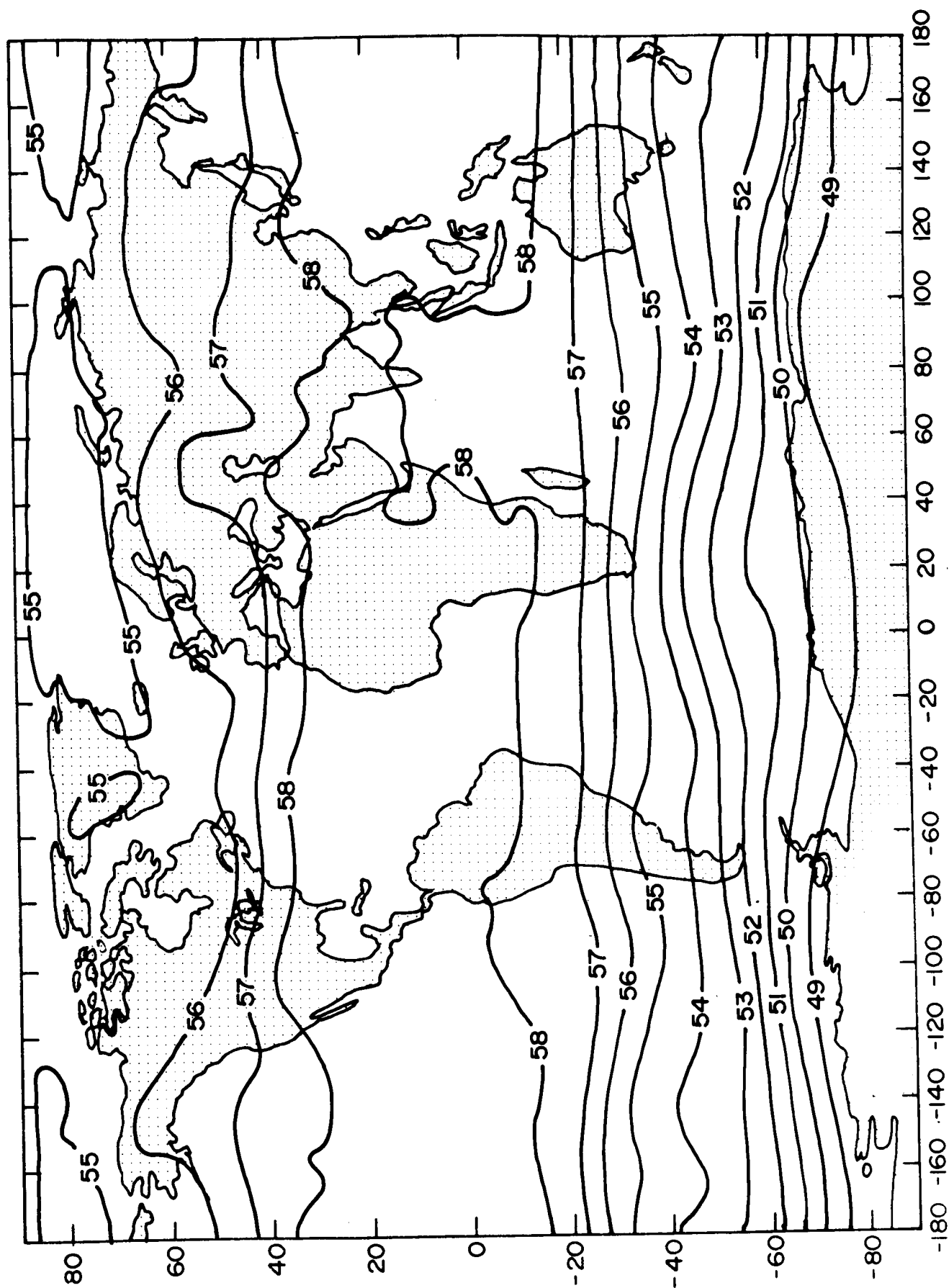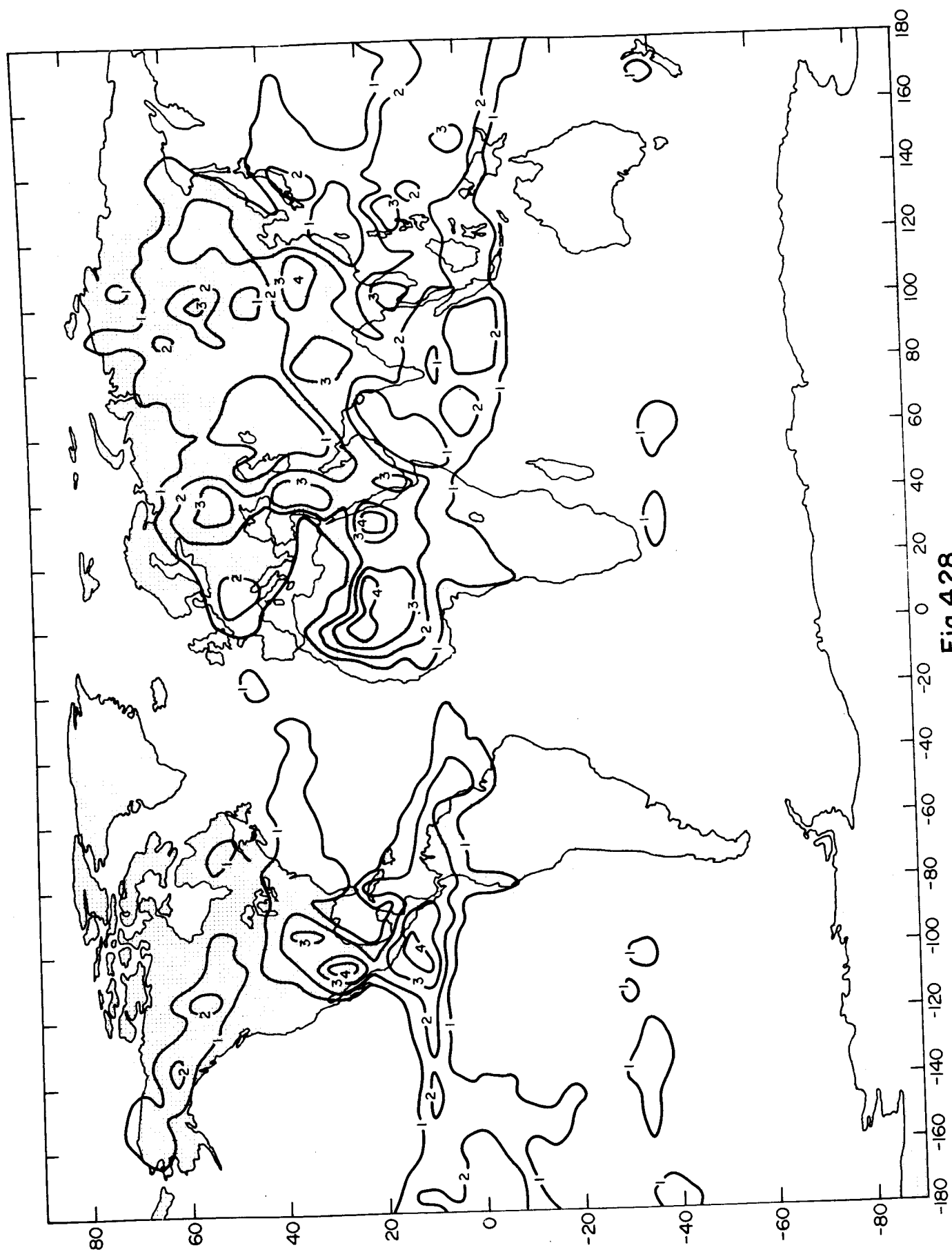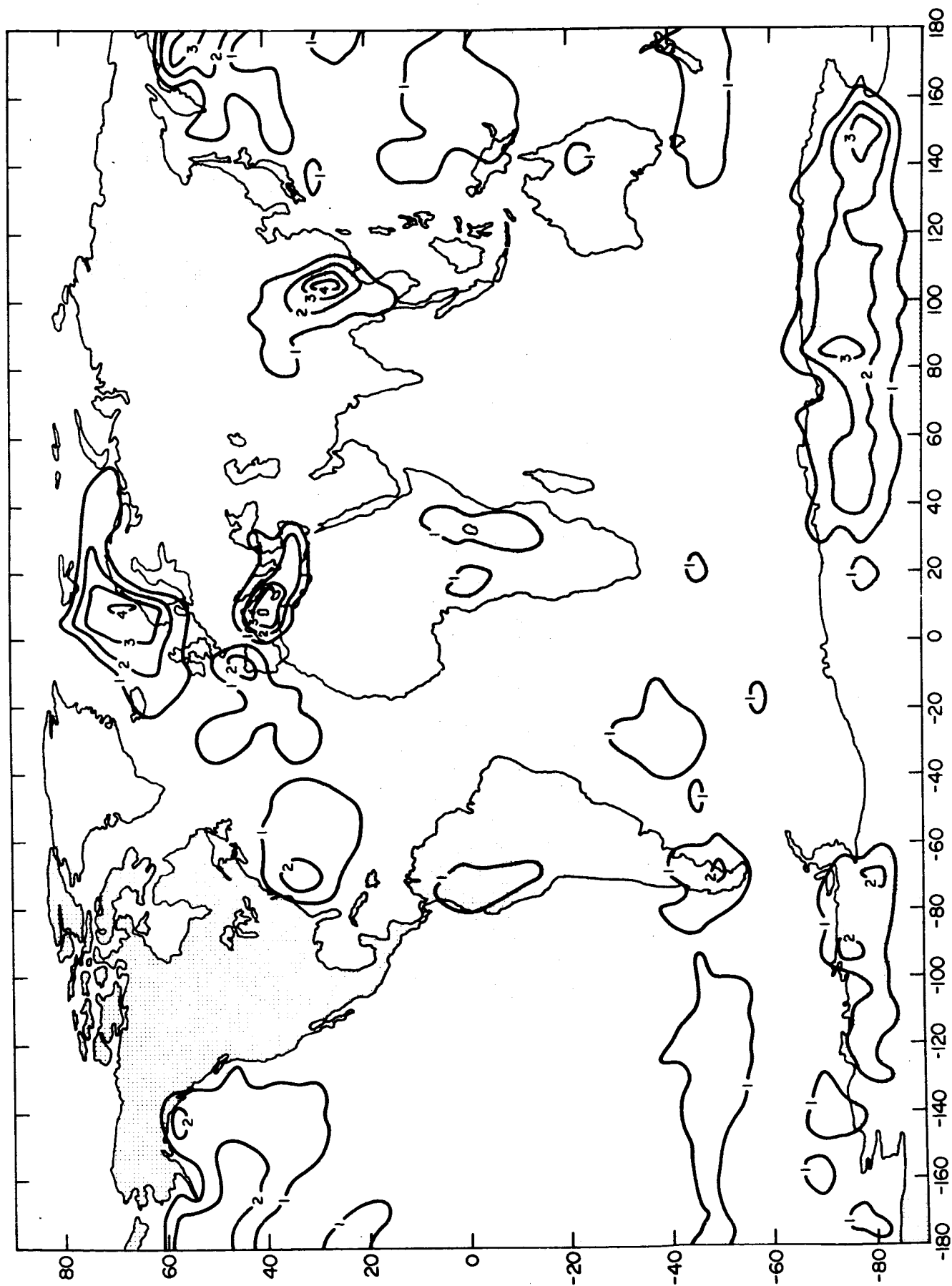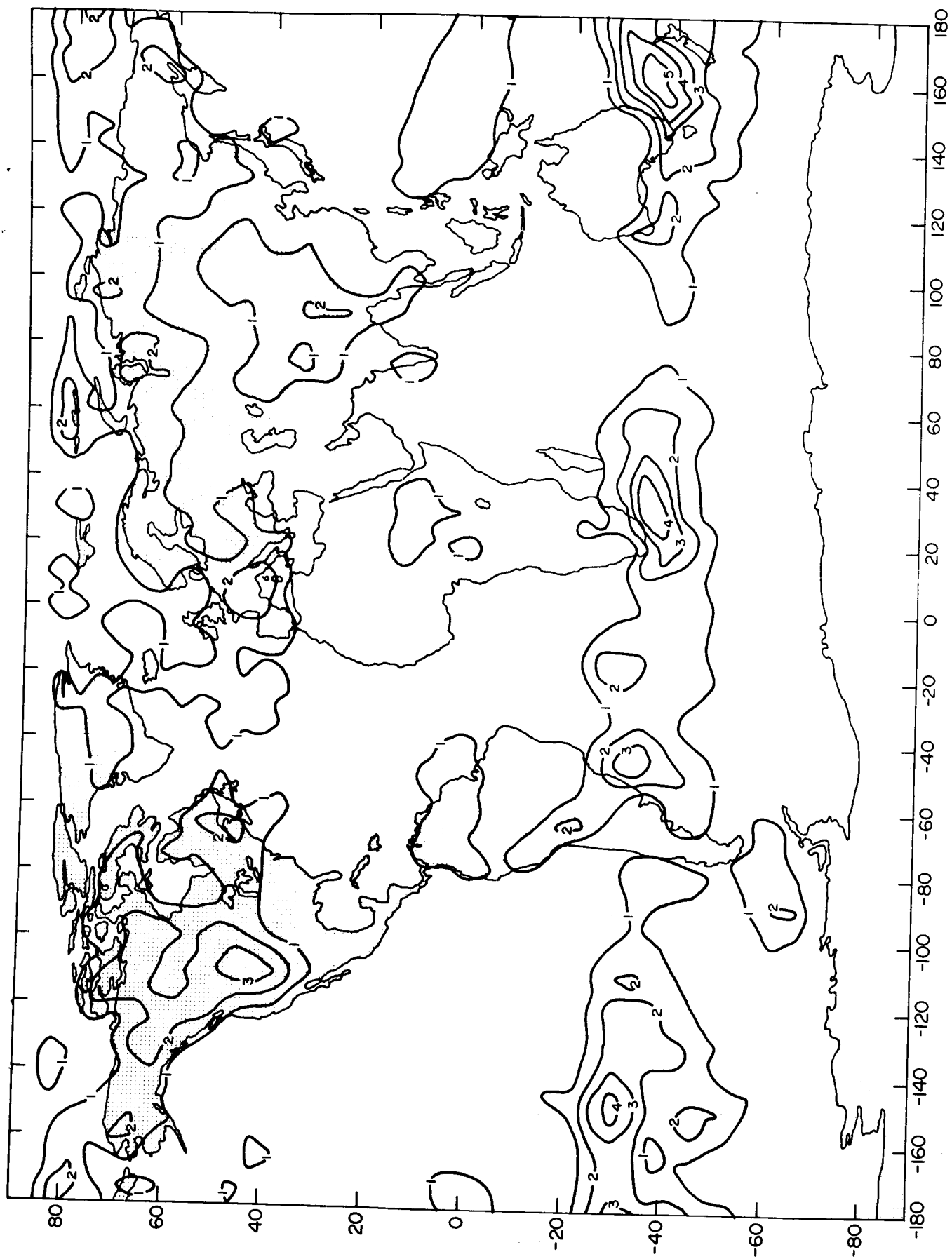
Fig.4.22

Fig. 4.23

Fig. 4.24

Fig. 4.25
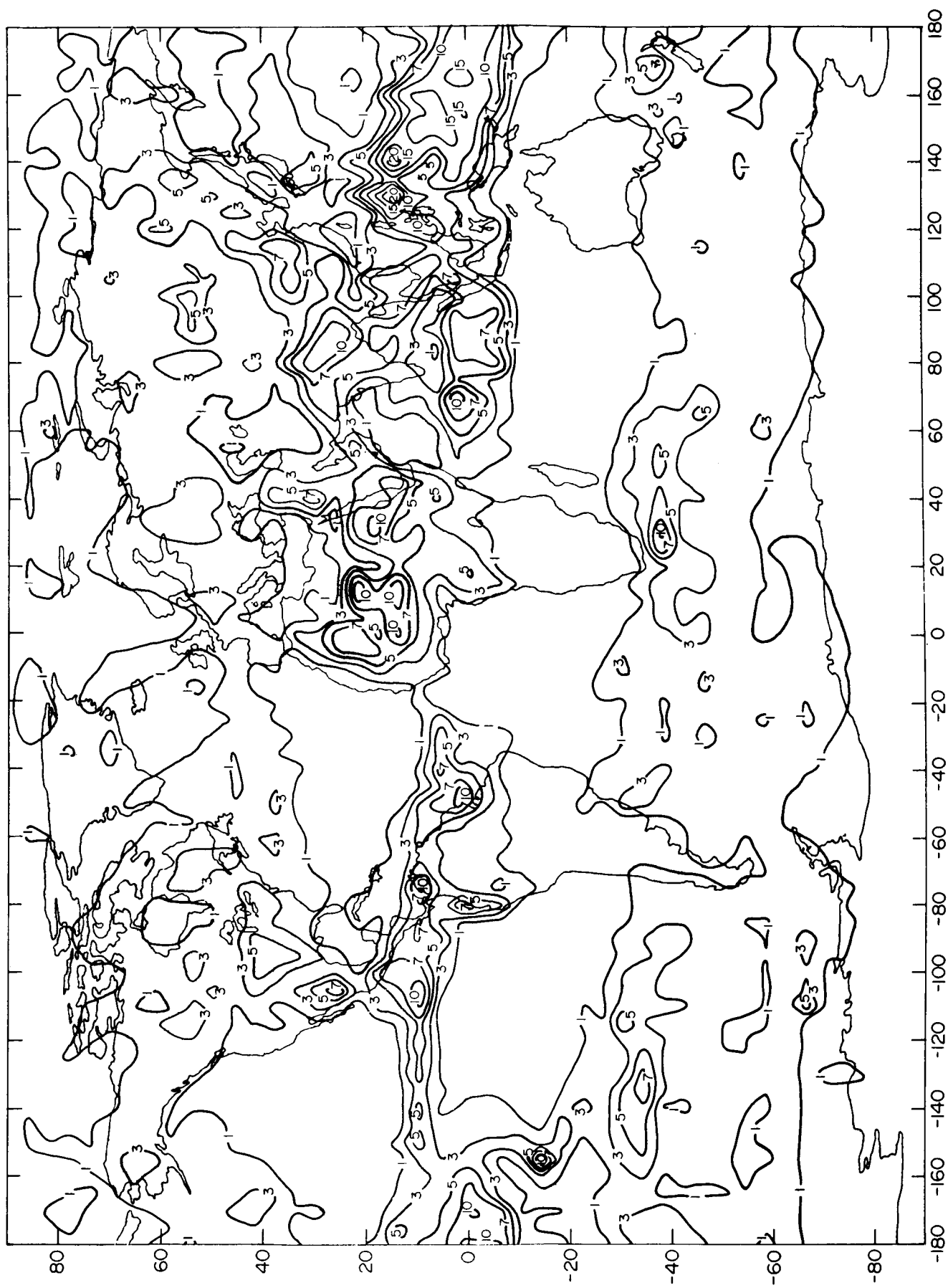
Fig. 4.26
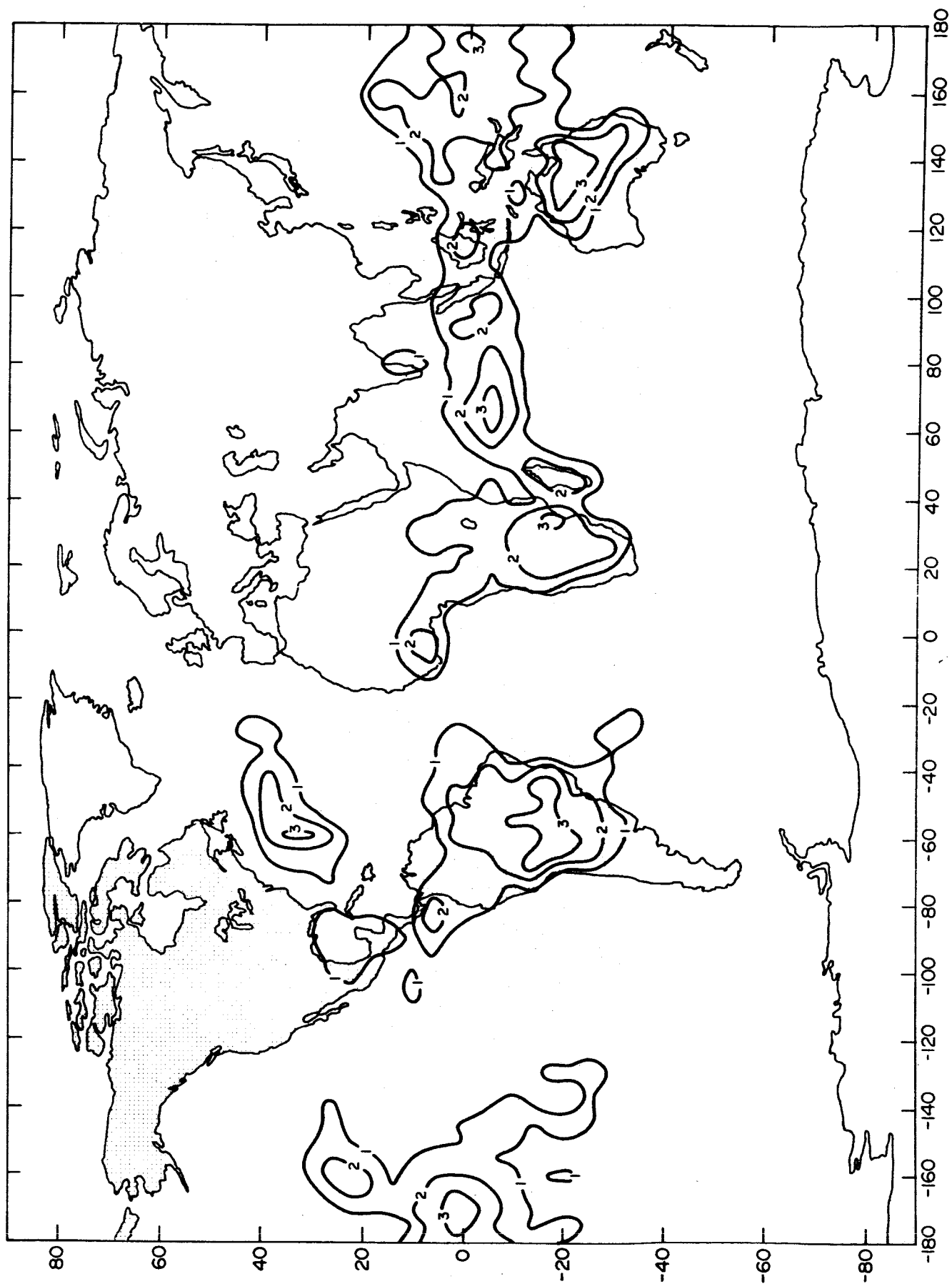
Fig. 4.27

Fig. 4.28

Fig.4.29

Fig. 4.30

Fig. 4.31

Fig.4.32